Title

Design and Application of Functional Hydrophilic Polymers in Engineering and Biomedical Drug Delivery

Author

Lo, Chiao-Yueh

Publication Date

2022

Peer reviewed|Thesis/dissertation

UNIVERSITY OF CALIFORNIA

Los Angeles

Design and Application of Functional Hydrophilic Polymers in Engineering and Biomedical Drug Delivery

A dissertation submitted in partial satisfaction of the

requirements for the degree Doctor of Philosophy

in Materials Science and Engineering

by

Chiao-Yueh Lo

2022

ABSTRACT OF THE DISSERTATION

Design and Application of Functional Hydrophilic Polymers in Engineering and Biomedical Drug Delivery

by

Chiao-Yueh Lo

Doctor of Philosophy in Materials Science and Engineering

University of California, Los Angeles, 2022

Professor Bruce S. Dunn, Co-Chair

Professor Jeffrey I. Zink, Co-Chair

Synthetic hydrophilic polymers are a type of polymers with polar or charged functional groups, and such functional groups render them with favorable interactions with water, leading to solubility or swellability. These polymers have been used in a wide variety of applications because they can be fabricated into novel materials with customized properties through carefully designed synthetic strategy and proper modification.

In the first chapter, a series of polyacrylamide (PAM) based polymers were applied to cohesionless, sandy soil for dust suppression. PAM is a hydrogel, a hydrophilic crosslinked polymer that does not dissolve in water and is a super water absorbent. We copolymerized PAM with hydrophobic units to control the polymer swelling ratio, and thus managed to mitigate the undesirable polymer swelling, soil matrix expansion, and the mechanical strength loss upon wet-dry processes. We further demonstrated that the treatment depth is controllable, which is crucial to minimize environmental impact, by fine-tuning the precursor composition for in-situ curing.

In the second and third chapters, we combined the functions of piezoresistive strain sensing and photothermal actuation into a single material, resembling living organisms' neuromuscular behaviors. This design solved the limitation of conventional physically-integrated sensory actuator systems with interface constraints and predefined functions. The material composed of an interpenetrating double-network of a nanostructured thermo-responsive hydrogel poly(N-isopropylacrylamide) and a light-absorbing, electrically conductive polymer. When connected to a control circuit, these muscle-like materials achieved closed-loop feedback controlled, reversible step motion.

In the fourth chapter, polydopamine (PDA) nanoparticles mixed with large pore MSNs were used to deliver drugs. This research seeks to develop nanotherapeutics to deliver an ultra-short course tuberculosis treatment regimen via inhalation, for both drug-sensitive and drug-resistant tuberculosis (TB). We shall develop in an iterative process nanotherapeutics that safely and effectively deliver each of the four drugs alone and in combination as well as nanotherapeutics that can deliver multiple drugs. We evaluated the optimized nanotherapeutics for safety and efficacy in treating tuberculosis in a murine model of pulmonary TB when administered via inhalation, both alone and in combination with oral therapy with the same drugs.

The dissertation of Chiao-Yueh Lo is approved

Ali Mosleh

Ioanna Kakoulli

Gaurav Sant

Bruce S. Dunn, Committee Co-Chair

Jeffrey I. Zink, Committee Co-Chair

University of California, Los Angeles

2022

Table of Contents

List of Figures

List of Tables

Acknowledgments

First and foremost, I am extremely grateful to my chair advisors, Professor Jeffrey I. Zink and Professor Bruce S. Dunn for their mentorship, patience, invaluable advice, and continuous support during my PhD study. I am not only respectful towards their immense knowledge and plentiful research experience, but also admires their optimism towards life and secrets of worlds. I would also like to thank my prior advisor, Professor Ximin He for her advice and endless enthusiasm towards cutting-edge technology. I would like to express my gratitude to collaborating PIs, Professor Marcus A. Horwitz, Professor Tsu-Chin Tsao, and Professor Edward Kavazanjian for their guidance which helped me through unfamiliar fields. I am also deeply grateful to my committees, Professor Ali Mosleh, Professor Ioanna Kakoulli, and Professor Gaurav Sant, for their critical advice on my proposal and final defense.

I would like to thank Yusen Zhao, who I cooperated with the most during my PhD life. I will never forget the days we stayed up late and worked on experiments in lab and the time we spent together discussing the manuscript and analytical data. I would also like to thank every lab member from collaborating labs, especially Dr. Hamed Khodadaditirkolaei, Dr. Cheolgyu Kim, Dr. Chen-Huan Pi, Dr. Bai-Yu Lee and Dr. Daniel L. Clemens for their kindness, brilliant work, and generosity of sharing their knowledge.

Thanks all of the lab seniors in Professor Zink's lab, especially Dr. Tian Deng and Dr. Fang-Chu Lin, and Professor Kamil Zaruba, for sharing their priceless experience and teaching me technical skills. I also feel very lucky to have Roxanne Castillo and Abir Swaidan as lab mates. We had good chats and enjoyed the life and food together, so I didn't get bored in such a small research group. Finally, I would like to thank my parents and my younger brother, who have

always supported me emotionally across the Pacific Ocean. I feel blessed to have such good family by my side.

Chapter 1 is reprinted with minor edition from [C.Y. Lo, H.K. Tirkolaei, M.T. Hua, I.M. De Rosa, L. Carlson, E. Kavazanjian, X.M. He, Durable and ductile double-network material for dust control, Geoderma, **361**, 114090, (2020), https://doi.org/10.1016/j.geoderma.2019.114090] with permission from Elsevier Science & Technology Journals. Co-author contributions: C.Y. Lo conducted chemistry experiments and drafted the manuscript. H.K. Tirkolaei, M.T. Hua, I.M. De Rosa conducted, analyzed the mechanical characterizations and reviewed the manuscript. L. Carlson, E. Kavazanjian, X.M. He are co-PIs.

Chapter 2 is reprinted with minor edition from [C.Y. Lo, Y.S. Zhao, C. Kim, Y. Alsaid, R. Khodambashi, M. Peet, R. Fisher, H. Marvi, S. Berman, D. Aukes, X.M. He, Highly stretchable self-sensing actuator based on conductive photothermally-responsive hydrogel, Materials Today, **50**, 35-43 (2021), https://doi.org/10.1016/j.mattod.2021.05.008] with permission from Elsevier Science & Technology Journals. Co-author contributions: C.Y. Lo, conducted the experiments and drafted the manuscript. Y.S. Zhao conducted the experiments and reviewed the manuscript. C. Kim conducted the simulations and drafted the paragraphs related to simulation. Y. Alsaid, R. Khodambashi, M. Peet, R. Fisher, H. Marvi, S. Berman, D. Aukes, assisted with experiments and reviewed the manuscript. X.M. He is the PI.

Chapter 3 is reprinted with minor edition from [Y.S. Zhao, C.Y. Lo, L.C. Ruan, C.H. Pi, C. Kim, Y. Alsaid, I. Frenkel, R. Rico, T.C. Tsao, X.M. He, Somatosensory actuator based on

stretchable conductive photothermally responsive hydrogel, Science Robotics, **6**(53), eabd5483, (2021), DOI: 10.1126/scirobotics.abd5483] with permission from American Association for the Advancement of Science. simulation was conducted. Co-author contributions: Y.S. Zhao, C.Y. Lo conducted the experiments and drafted the manuscript. L.C. Ruan, C.H. Pi provided the automation and control system and drafted the paragraphs related to closed-loop control. C. Kim conducted the simulations and drafted the paragraphs related to simulation. Y. Alsaid, I. Frenkel, R. Rico reviewed the literatures and manuscript. T.C. Tsao, X.M. He are co-PIs.

Chapter 4 contains contents from a collaboration project funded by National Institutes of Health and U.S. Army Medical Research Acquisition Activity. Chiao-Yueh Lo conducted the synthesis, fundamental characterizations and drafted the chemistry-related paragraphs. Bai-Yu Lee and Daniel L. Clemens conducted the experiments and drafted the paragraphs related to bioassay. Marcus A. Horwitz, and Jeffrey I. Zink are co-PIs.

Vita/Biographical Sketch

Education

M.S. in Material Science and Engineering (Polymer materials) **2010-2012**

National Taiwan University

B.S. in Material Science and Engineering **2006-2010**

National Taiwan University

B.S. in Chemistry **2006-2010**

National Taiwan University

Publications

First Author Research Articles

1. "Highly stretchable self-sensing actuator based on conductive photothermally-responsive hydrogel", Materials Today, ISSN: 1369-7021, **2021**.
2. "Somatosensory actuator based on stretchable conductive photothermally responsive hydrogel", Science Robotics 6 (53), eabd5483, **2021**.
3. "Durable and ductile double-network material for dust control", Geoderma, Volume 361, 114090, **2020.**

Co-author Research Articles

1. "Poly (Vinyl Alcohol) Hydrogels with Broad-Range Tunable Mechanical Properties via the Hofmeister Effect", Advanced Materials 33 (11), 2007829, **2021**.
2. "Interactively full-color changeable electronic fiber sensor with high stretchability and rapid response", Advanced Functional Materials 30 (19), 2000356, **2020**.
3. "Hydrocipher: Bioinspired dynamic structural color-based cryptographic surface", Advanced Optical Materials 8 (1), 1901259, **2020**.

Book Chapter

1. "Bioinspired sensors and actuators based on stimuli-responsive hydrogels for underwater soft robotics", Bioinspired Sensing, Actuation, and Control in Underwater Soft Robotic Systems, 99-115, **2021**.

Chapter 1. Durable and Ductile Double-network Material for Dust Control

Chapter 1 is reprinted with minor edition with permission from Elsevier Science & Technology Journals.

Authors: Chiao-Yueh Lo,[a] Hamed Khodadadi Tirkolaei,[b] Mutian Hua,[a] Igor M. De Rosa,[a,c] Larry Carlson,[c] Edward Jr. Kavazanjian,[b] Ximin He[a]

Affiliations:

[a] Department of Materials Science and Engineering, Henry Samueli School of Engineering and Applied Science, University of California, Los Angeles, 410 Westwood Plaza, Los Angeles, CA 90095

[b] Center for Bio-mediated and Bio-inspired Geotechnics, Arizona State University, 650 E. Tyler Mall Tempe, Arizona 85281

[c] Institute for Technology Advancement, Henry Samueli School of Engineering and Applied Science, University of California, Los Angeles, Engineering VI, Suite 510 Los Angeles, CA 90095

Corresponding Author: Ximin He (ximinhe@ucla.edu)

ABSTRACT

Dust generation is a world-wide issue due to its serious deleterious effects on the environment, human health and safety, and the economy. Although various dust suppression methods have been used for decades, some critical drawbacks in state-of-the-art technology still remain unsolved, such as short-lasting, ground water impact, and prone to water. This work reports a soil stabilizer based on non-toxic material (Andersen, 2005; Berndt et al., 1991; Horak et al., 1997) and forms a **d**uctile and **d**urable **d**ouble-network in soil, namely "**D^3** soil stabilizer", which not only improves soil mechanical toughness of surface soil but also suppresses dust generation. A copolymer comprising hydrophilic and hydrophobic components combined with enzyme-induced carbonate precipitation is utilized as an in-situ gelation binder to soil particle. The tunable hydrophobic-to-hydrophilic component ratio minimizes undesirable soil matrix expansion and mechanical strength loss upon experiencing wet-dry processes, while still retains good water affinity. We further demonstrated controllable treatment depth by fine-tuning precursor composition, which is essential to minimize environmental impact. The double-network morphology with carbonate precipitate embedded uniformly in polymer matrix is observed via microscopic imaging. The nature of outstanding ductility, high durability against water, and good long-term stability were supported by systematic unconfined compressive strength (UCS) measurements on treated soil, which show strong inter-particles binding, good retention of peak strength, increased strain at peak strength, and increased toughness after soil samples have experienced wet-dry processes.

1. INTRODUCTION

Dust generation is a world-wide issue due to its serious deleterious effects on the environment, human health and safety, and the economy. Dust refers to the wind-blown particles eroded by air. The soil particles with the size of around 0.18 mm (i.e. fine sand) was reported to have the highest susceptibility to air erosion (Garrels, 1951). Very fine soil particles are more resistant to detachment by wind due to inter-particle cohesion (Wilson, 2001). Dust particles can contaminate water and food and, when inhaled, can lead to serious respiratory ailments, while dust clouds are traffic hazards as they can reduce visibility during road and aircraft transportation. The concentration of airborne fugitive dust particles is used as an air quality indicator by the United State Environmental Protection Agency (EPA). Sources of airborne fugitive dust include construction activities, travel on unpaved roads, wind storms, wildfires, and agricultural activities.

The conventional method for mitigating dust is to spray water on the source area, while the main issue with applying water is that the dust is suppressed only as long as the source area remains wet, and it is often complicated by the scarcity of water in hot, arid areas, making procurement of sufficient water difficult and costly. Incorporation of hygroscopic salts such as magnesium or calcium chloride in water applied for dust control is often done in an attempt to retain moisture on the surface. However, application of salt has many disadvantages, including to the need for relatively high concentration of salt and associated equipment corrosion and surface and ground water impacts (due to the high solubility of the salts in water). Various types of chemical dust suppressants including surfactants, polymers, bituminous products, and resins (Foley et al., 1996), are also commercially available.

Notwithstanding that there is a wide variety of soil stabilizing materials that facilitates soil strengthening and dust suppression, there is a need for alternatives with enhanced effectiveness and less environmental impact. Within last two decades, extensive attention has been paid to use of biocompatible and bio-based products for dust suppression, including synthetic hydrogels, bio-polymers, and biologically mediated mineral precipitation (Bang et al., 2009; Chen et al., 2015; Hamdan and Kavazanjian, 2016; Kavazanjian Jr et al., 2009; Liu et al., 2018; Meyer et al., 2011). Synthetic hydrogels and bio-polymers are attractive because of their water retaining ability and because their application typically does not require compaction (Chang et al., 2015c), which make them compatible with establishment of vegetation on the treated surface. Biopolymers such as gellan gum, guar gum (Chang et al., 2015b) and xanthan gum (Chang et al., 2015a; Chang et al., 2015c) can provide not only a surficial soil strength level comparable to cement-treated soil but also high ductility via reversible hydrogen bonding (Chang et al., 2015b). However, water-soluble biopolymers lose strength and can be flushed from the soil when they are exposed to water. By contrast, synthetic hydrogels are cross-linked hydrophilic polymers and thus water insoluble. In fact, synthetic polymers have been used as a soil conditioner in agriculture for decades due to their good water retention and anti-erosion functions (Barvenik, 1994; Mirzababaei et al., 2017; Orts et al., 2007; Paganyas, 1975).

Moreover, cohesionless soils are also lower in load-bearing capacity, shear strength, and plasticity which make them prone to damage during earthquake (e.g., liquefaction) and in heavy rainy season. Some traditional soil strengthening methods such as geosynthetics matting and cementation, which produces poly(carbonate-silicones) to bind soil particles and significantly improve soil strength (Firoozi et al., 2017), suffer from bio-incompatible issues, as the formed dense water-blocking layer suppresses plant root system development and causes severe surface

water runoff (Eith and Koerner, 1992; Federation and Engineers, 1998; Koerner, 2012). These new challenges in environmental protection and infrastructure sustainability bring up growing demands for new soil strengthening techniques that are non-toxic, long lasting, and effective in enhancing ground loading capacity and resiliency.

Recently, innovative biologically mediated mineral precipitation techniques, such as microbially induced carbonate precipitation (MICP) and enzyme induced carbonate precipitation (EICP) have been proposed for dust control (Bang et al., 2009; Hamdan and Kavazanjian, 2016; Meyer et al., 2011). These techniques bind soil particles together via precipitation of carbonates as cementitious agent, forming an erosion resistant crust on the treated surface to mitigate dust generation. MICP and EICP combined with hydrogels have been shown to facilitate the retention of the treatment solution at the surface, enhancing erosion-resistant crust formation (Hamdan et al., 2016; Wang).

We have previously reported synthesis of a hybrid soil stabilizing material based on a combination of EICP and a biopolymer, xanthan gum (Hamdan et al., 2016), or a synthetic hydrogel, poly(acrylic acid) (PAAc) (Zhao et al., 2016). This method can significantly enhance the strength of treated soil after dehydrated (Hamdan et al., 2016; Zhao et al., 2016). However, this approach suffers from a water durability problem arose from drastic polymer swelling.

In this research, we managed to mitigate the water durability problems using a series of hydrophilic-hydrophobic copolymers instead of hydrogels. Additionally, we used a polyacrylamide (PAAm) backbone to replace the polyacrylic acid (PAAc) backbone used in previous research (Zhao et al., 2016) to facilitate curing under ambient temperature conditions instead of at elevated temperature and for reducing peroxide initiator usage. The curing rate was

also improved from longer than 1 day to several minutes (under ambient temperature). This new soil stabilizing material provides the ability to control solidification of the polymer precursor fluid, which results in a controllable and tunable treatment depth (i.e. crust thickness) and minimizes the potential for pollution to ground water. This material is also more ductile than our earlier formulations, reducing the chance of crack formation in the surface crust under traffic loads. Furthermore, it does not exacerbate CO_2 emissions and exhibits good water affinity for vegetation growth.

The rational design concept of **d**urable, **d**uctile **d**ouble-network (D^3) soil stabilizer is shown in **Figure 1**. Specifically, to improve the "**water durability**" of treated soil, tunable hydrophilicity is achieved by molecular-level design using a copolymer composed of both hydrophilic and hydrophobic units. The overall hydrophobicity of the copolymer network is determined and tuned by the "backbone: co-monomer" ratio. With more hydrophobic units, the water binding ability within polymer is weaker, so the undesirable swelling which is usually observed in hydrogels can be reduced.

To mitigate fracture in the treated surface due to deformation caused by human activity and traffic, we employ a "**double-network**" design that utilizes milli-/micro-scale polymer network to reinforce the inorganic-cemented soil network with "**ductility**", inspired from microfiber reinforcement of concretes, where polymer microfibers provide ductility in concrete matrix and sandy soil (Durairaj and Janaki Sundaram, 2015; Liu et al., 2017). These treatments are proven to be capable of transforming matrix bulk characteristics from brittle to malleable, which provide impact dissipation ability and prevent crack or fracture upon external strain. With these micron-scale fiber-based network, peak strength and strain at fracture of reinforced soil are

improved (Liu et al., 2017). Therefore, we anticipated polymer network to mechanically hold soil particles in place and leads to higher fracture toughness.

On the other hand, EICP and MICP have been demonstrated to be effective for binding cohesionless soil particles (Hamdan and Kavazanjian, 2016; Kavazanjian et al., 2017; Meyer et al., 2011; Mujah et al., 2017) by providing cementation at the inter-particle contacts but results in a relatively brittle structure. Here, we combined an EICP-based inorganic crystal network with the above-described copolymer-based organic network to both bind soil particles and create ductility. By selecting polymers capable of forming resilient, dynamic intermolecular bonding, including the hydrogen bond between polymer chains and between polymer and soil particles (shown in **Figure 1(d)** as dashed lines) as well as increased anchoring points on soil particle surface, a higher toughness of treated soil can be achieved via increased bulk "ductility". In addition, both the copolymer network and the EICP treatment can be applied from aqueous solution at ambient temperature. This common merit facilitates an in-situ curing process that can trap stabilizer solution at ground surface and provide precise control of the solution penetration into soil, mitigating any potential for contamination of ground water.

2. MATERIALS AND METHODS

2.1 Materials

F60 silica sand was provided by US Silica. Acrylamide (AAm, 98%, extra pure), (hydroxyethyl)methacrylate (HEMA, 97%, stabilized), acrylic acid (AAc, 98%, extra pure, stabilized), ammonium persulfate (APS, 98%, ACS grade), tetramethylethylenediamine (TEMED),

calcium chloride (96%, extra pure), and urea (bioreagent grade) were purchased from Fisher Scientifics and used as received without further purification. Urease from jack beans, Canavalia ensiformis, (reported activity of 34960 units/g), and N,N'-methylenebisacrylamide (BIS, 99%) were purchased from Sigma Aldrich and used as received.

2.2 Instrument

Scanning electron microscopy (SEM) images and energy dispersive X-ray spectroscopy (EDS) samples were first sputtered with ~5 nm thickness of gold, and then examined in NOVA NanoSEM 230, under low vacuum (~50 Pa) condition. Unconfined compressive dtress tests were conducted in a “GCTS Testing Systems” and “Instron 5966 universal testing machine”. Powder X-ray diffraction (XRD) spectra of soil samples were obtained using Cu-Kα radiation on a Panalytical X’Pert Pro Powder X-ray Diffractometer.

2.3 Preparation of D^3 stabilization precursor solutions

(1) For preparing the D^3 stabilization precursor solution of poly(AAm-co-HEMA)-EICP as depicted in **Figure 1(c)**, a 4g mixture of AAm and HEMA (70:30 molar ratio), 0.2g of BIS as crosslinker, and 25μL of TEMED as catalyst were dissolved in 10mL of distilled water. Then, this polymer precursor solution was mixed with the EICP precursor solution, a mixture of $CaCl_2$ (1.25M), urea (1.875M), and free urease enzyme (jack bean urease = 4.5mg/mL) in a 5:4:1 volume ratio. Last, to initiate the polymerization, APS as initiator was added to the mixture at 0.5% w/w ratio with respect to the total polymer concentration. (2) To prepare the two control agents, polyacrylamide (PAAm)-EICP precursor and polyacrlic acid (PAAc)-EICP precursor, the AAm

and HEMA mixture was replaced by respectively 4g of AAm or 4g of AAc (added dropwisely), with other components kept the same.

2.4 Preparation of soil samples for unconfined compressive strength (UCS) tests and SEM inspection

Unconfined compressive strength (UCS) was performed to evaluate inter-particle bond strength in the treated samples, which indicates how strong the treated sample is against erosion. To achieve uniform soil columns for UCS, the precursor solution was mixed with the soil. Ottawa F-60 sand (with the specifications presented in **Table 1**) was used in this study as it has particle size that has been reported to be highly susceptible to air erosion (Garrels, 1951). 180g of F-60 sand was thoroughly mixed with 50 mL of precursor solution. Then, the mixture was poured into a cylindrical plastic mold with an inner diameter of 1 3/4". Relative density of the soil was around 40%. Air bubbles were removed carefully by gently stirring the mixture within the plastic mold, followed by sufficient settlement of sand particles. Then, the samples were cured at ambient temperature for 5~30 minutes (depending on precursor composition) until the samples were solidified. After the curing, the soil sample was extracted from the mold and then oven-dried for 48 hours at 50°C. The purpose of oven-drying is to accelerates the drying process, and since it is applied after gelation, which is the characteristic phenomena indicating polymerization completion, the oven-drying has negligible impact on the polymerization reaction. Each sample was approximately 4.00 cm in diameter and 7.60 cm in height. After oven drying, each sample was subject to UCS testing at a strain rate of 1.27 mm/min. A small piece of each sample was also used for SEM examination. The sample was placed on the SEM sample holder by carbon tape and then sputter-coated with a 5nm-layer of gold to prevent charging of the material by the electron beams.

Table 1: Specifications of F-60 sand.

Silica Content	**D_{10}** (mm)	**D_{30}** (mm)	**D_{50}** (mm)	**D_{60}** (mm)	**e_{max}**	**e_{min}**	**G_s**	**Hydraulic conductivity at D_r = 40%** (cm/s)
99.7	0.15	0.19	0.23	0.26	0.83	0.60	2.65	0.022

2.5 Powder XRD analysis

Powder XRD specimens were prepared by collecting the supernatant during soil sample molding, followed by precursor gelation, dried overnight in oven to form clear-white granules, and carefully ground into white powder with ceramic mortar. The powder was placed in rectangular sample holders for examination, and the resulting spectrum were analyzed by built-in database on Panalytical X'Pert Pro Powder X-ray Diffractometer.

2.6 Treatment depth examination

We have examined the treatment solution infiltration depth as well as the thickness of crust formed on the treated surface. Precursor solutions with different initiator concentrations were applied to the top surfaces of the untreated soil sample columns and the infiltration depth was measured. The precursor solutions were allowed to infiltrate into soil by gravity and the solution infiltration depth was traced by the progression of wet-dry interface. The samples were allowed to cure under the 25°C ambient condition for 5~30 minutes (depending on precursor composition) and then the soil samples were placed into an oven at 50°C for 48 hours to remove residual water. Afterwards, the non-bound soil was removed carefully from the bottom of each soil sample and the thickness of surface crust was recorded as actual treatment depth.

2.7 Water infiltration test

A water infiltration test was conducted on dried treated soil samples using a lab-scale method modified from the single-ring infiltrometer method (ASTM International, 2018; Johnson, 1963) sometimes used in the field. A transparent test tube with graduation marks was placed in the center of each sample before curing. Then, the samples were prepared using the same protocol as for UCS tests. To measure the water infiltration rate, distilled water was added into the tube to a certain height above the sample's surface and the cumulative volume of water infiltrated into soil was calculated by measuring the reduction in height of the water column above the soil surface. The infiltrated volume was plotted versus elapsed time. The infiltration rates increased with time and eventually reached a maximum value. The saturated infiltration rate (i.e. slope of linear part on the plot) was taken as the hydrated water infiltration rate. The infiltration rates between samples with and without hydrophobic monomer HEMA, i.e., soil samples treated by PAAm-EICP and P(AAm-co-HEMA)-EICP, were compared.

2.8 Wet-dry cycle durability tests

To evaluate bond strength under cycles of wetting and drying and swelling under wet condition in the treated samples, the completely dried soil samples (treated with the same amount of stabilizer precursor solutions, 50mL per 180g of F-60 sand) were first immersed in distilled water for 8 hours to remove precursor residual and achieve equilibrium swollen volume. Next, the wet samples were again oven-dried for 48 hours at 50°C. The UCS test was conducted on these samples and stress-strain curves as well as toughness were obtained. Volumes of bare polymers and soil samples after 1~3 wetting and drying cycles were directly measured by their dimensions with a digital vernier scale at 0.01mm precision. The results were compared with those samples

which were not subject to wetting and drying cycles. The volume of each sample after wetting to the volume of the same sample at dry condition was defined as swelling ratio.

2.9 Long-term heat durability.

To evaluate the long-term durability of the samples, we employed the accelerated thermal degradation test described in our previous work (Zhao et al., 2016). In this test, small-scale poly(PAAm-co-30% HEMA)-treated cylindrical soil samples (2.50 cm × 1.85 cm) were placed in an oven under 50°C for 30 days. By applying kinetic equations of chemical reactions (i.e., Arrhenius relationships, $\ln k = \ln A - \frac{E_a}{R}\frac{1}{T}$, in which the logarithm of reaction rate constant k is linearly related to the reciprocal of reaction temperature T), it was estimated that this accelerated thermal degradation condition is equivalent to more than 3 months exposure under 25°C. After the 30-days of exposure at 50°C, the strength of the samples was determined using UCS testing. The change in strength and toughness before and after the heat exposure is reported as an indication of long-term thermal durability.

3. RESULTS AND DISCUSSION

3.1 Evidence of soil particle binding

Under SEM examination, we observed that the copolymer materials used in this study have good affinity with sandy soil particles surface. As **Figure 2(a)** shows, the soil particles are surrounded and bonded tightly by cured polymer. **Figure 2(b)** shows the calcium carbonate precipitates formed from EICP reaction, observed as spheres with 1~2 μm diameter. The chemical

composition of each microstructures observed in SEM were further confirmed by EDS mapping. In **Figure 2(d)**, three representative elements, namely carbon, silicon, and calcium, were selected to mark polymer region, soil particle region, and calcite region, respectively. The EDS mapping result showed that soil particles (silicon-rich region) were surrounded by polymer network (carbon-rich region), while the universally existing calcium may indicate calcium carbonate precipitates embedded within polymer and on soil particle surfaces or calcium ion trapped within polymer network, as depicted in **Figure 2(c)**.

To further confirm the existence of calcium carbonate precipitates, powder XRD was conducted, and the spectrum shown in **Figure 2(e)** was taken on supernatant retrieved while molding the sand samples. The supernatant was solidified by polymer network, dried, and ground into powder, and this powder contains a poly(AAm-co-HEMA) matrix embedding both calcite and suspended sand particles. The diffraction peaks noted indicate a significant amount of quartz, which is the main component of F60 sand, while the characteristic peak at $2\theta=29°$ indicated the existence of calcium carbonate in rhombohedral calcite form. The broad hill at small angle region is originated from the amorphous poly(AAm-co-HEMA) matrix. It is reported that precipitation of calcium carbonate on soil particle surface can improve the mechanical properties of bulk soil with increased cohesion between soil particles (Kavazanjian et al., 2017; Meyer et al., 2011; Mujah et al., 2017). Also, researches focusing on composite materials showed that nanoscale mineral precipitates, such as calcium carbonate, calcium phosphate, as well as clay particles within polymer network, enhanced the mechanical properties of the matrix (Rauner et al., 2014; Rauner et al., 2017; Schexnailder and Schmidt, 2009; Thoniyot et al., 2015). In such system, these mineral particles can physically strengthen the matrix as filler (Rai and Singh, 2004) or forms reversible non-covalent bonding (Gao et al., 2015), which contributes to strength and toughness.

In addition, uniformly distributed calcium overlapping the polymer region in EDS mapping in **Figure 2(d)** could also indicate the metal complex formed between calcium ion and the metal-chelating amide groups (-NH_2) within polyacrylamide. These calcium chelating sites were also reported to function as reversible, non-covalent crosslinking, which contributes to the ductility, toughness and the ability to recover from deformation of composite network (Li et al., 2014; Sun et al., 2012; Yuk et al., 2016). Therefore, we believe that the microstructure characteristic we observed contributes to its enhanced mechanical properties, which will be discussed in latter sections.

3.2 Evidence of Bond Strength

To address the efficacy of the binder material for creating enough inter-particle cohesion to resist against wind erosion, UCS test on the treated sand columns was used as an indication of inter-particle bond strength. A higher UCS represents a greater inter-particle cohesion, which means a higher velocity of eroding agent (i.e., wind) is required to cause particles detachment. In addition, the UCS shows how resistant the surface is against fracture due to the loads caused by human activity and traffic on the surface. As shown in **Table 2**, UCS of the treated specimens ranges between 1.7 MPa and 5.4 MPa, which is comparable with pavement materials (Bondietti et al., 2004). This demonstrates that all these materials have the potential of application for surficial treatment of low volume unpaved roads and construction sites which are two of the main sources of dust generation.

Table 2: Mechanical properties of soil samples treated with PAAm-EICP and P(AAm-co-HEMA)-EICP with different HEMA ratios showed robust mechanical behavior in contrast with PAAc-EICP treatment. After wet and redried, these samples also showed significantly improved retainment of mechanical properties, comparing to the disastrous loss in PAAc-EICP treated soil.

	Original		Wet-redried	
	Peak Strength (kPa)	Strain at Peak Strength (%)	Peak Strength (kPa)	Strain at Peak Strength (%)
PAAc	1755	8.98	1917	1.79
PAAm	5419	3.89	5205	7.46
P(AAm-co-10% HEMA)	4743	3.61	5498	5.56
P(AAm-co-20% HEMA)	4255	3.46	4201	4.53
P(AAm-co-30% HEMA)	3498	2.67	3557	4.16
P(AAm-co-40% HEMA)	3992	3.34	4167	4.24

3.3 Treatment depth control

Controlling the thickness of the crust on the surface and preventing the treatment solution to run-off or penetrate deep into ground water are essential factors that should be considered in soil surface treatment for dust control. To demonstrate the potential for precise control of treatment depth, we have achieved different solution infiltration rate by altering the reaction rate of precursor solution with different initiator concentrations, as shown in **Figure 3(a)**. Here, the precursor

solution was applied to soil sample by pouring onto the top surface of soil column, and the progression of precursor infiltration front can be traced by the movement of interface between wet soil and dry soil. PAAm-EICP precursor solutions with initiator to total polymer weight ratio of 0.25%, 0.50%, and 1.00% resulted in increasing curing speed and thus decreasing precursor infiltration depths from >12.0cm to 10.0cm and 6.0cm, respectively. However, the final treatment depth is a result of the competition between curing speed and infiltration speed. In **Figure 3(b)**, a slower curing rate of 30 minutes (with 0.25% initiator) results in more solution runoff and dilution of reactive agents. The incomplete polymerization led to less dense, crumbled structure of bound soil and relatively shallower treatment depth of only 6.5 cm (left), in contrast with its >12 cm infiltration depth. Meanwhile, those treated with 0.50% (middle) and 1.00% initiator (right) resulted in final treatment depths of 8.5 cm (10.0 cm infiltration) and 6.0 cm (6.0 cm infiltration), showing more effective solidification within their infiltration depths. The shallowest surface treatment depth with the most densely bound soil (right) was achieved with the rapist curing rate of 3 minutes, in which curing occurred before the precursor could infiltrate deep into the soil. The deepest treatment depth (middle) was achieved with medium curing rate of 10 minutes, in which the curing rate and precursor solution infiltration rate were more optimally coupled. We also observed that the precursor solutions are initially capable of infiltrating quickly into soil due to their low viscosity. Then, the solution infiltration slowed down due to viscosity increase as the polymerization took place and eventually solidified when the reaction completed. Therefore, with the tunability and flexibility in reaction speed of our method, the infiltration rate can be accelerated or decelerated to adapt into soil with different permeability. Our solutions can also be tailored for various soil condition and applications, such as surface and ground treatment. Furthermore, this

high controllability of solidification is a crucial property of our method to avoid chemical pollution and unnecessary disturbance to surroundings.

3.4 Durability: Water affinity and stability

We proposed a copolymer composed of both hydrophilic and hydrophobic units with tunable hydrophilicity in aim of improving "**water durability**" of treated soil. However, our preliminary results revealed that surfactants in the polymer precursor solution, which are essential in mediating the copolymerization reaction of hydrophilic acrylamide with hydrophobic units, significantly lower the reactivity and increase the viscosity of the precursor solution. As a result, the presence of surfactant in the precursor solution causes severe difficulties in practical application. Thus, we selected a co-monomer that is less hydrophilic than the backbone AAm monomer but still with acceptable solubility in water, namely (hydroxyethyl)methacrylate (HEMA), to fabricate poly(AAm-co-HEMA) in this research. The highly bio-compatible polyHEMA derivatives have long been used as contact lens material in many ophthalmic applications, owing to their malleability when wet and robustness when dried (Childs et al., 2016). Use of HEMA monomer as a property modifier to improve the fracture strength of acrylic and methacrylic hydrogels has also been reported (Omidian et al., 2010).

We aimed to reduce swelling behavior of our soil stabilization treatment during wet-dry cycles, while still retaining good vegetation compatibility. As shown in **Figure 4(a)**, the initial water infiltration rate of the dried poly(AAm-co-HEMA)-EICP treated soil is increased, reflecting a higher water affinity. The hydrated infiltration rate (linear part) of soil samples also increased to 0.472 (cm/hour) when treated by poly(AAm-co-HEMA) in contrast with 0.123 (cm/hour) of PAAm. The faster hydrated infiltration rate may indicate a higher porosity or good water affinity

of treated soil, both properties are essential for vegetation root system development (Hamza and Anderson, 2002; Hamza and Anderson, 2003; Hamza and Anderson, 2005). Thus, an improved vegetation compatibility can be achieved with poly(AAm-co-HEMA) owing to good water retention nature of hydrogels and good porosity, comparing to low vegetation compatibility from compacted, water-blocking layer of traditional cement and inorganic soil stabilizers.

For swelling behavior characterization, poly(AAm-co-HEMA)-EICP treated soil showed swelling ratio reduction. Bare poly(AAm-co-HEMA) copolymers with increasing HEMA content showed reduction in swelling ratio from 760% to 500% (w/w), as depicted in **Figure 4(b)**, which is critical for reducing soil structure damage upon wet-dry cycles. As a result, in **Figure 4(c)**, soil samples treated with the less-swelling poly(AAm-co-HEMA) also showed a significant volumetric swelling reduction, in which the swelling ratios are reduced to approximately 0%. Furthermore, this beneficial effect on soil crumble prevention also applied to multiple wet-dry cycles. PAAc-EICP as well as PAAm-EICP treated soil samples not only showed higher volumetric swelling ratios, but also an increased swelling with more wet-dry cycles. This phenomenon can be attributed to the repeated swelling of polymer, which enlarges the pores within soil samples and provide extra spacing for even more severe polymer swelling. In comparison, swelling ratio of poly(AAm-co-HEMA)-EICP treated soil remained at negligible level, leading to significantly enhanced water durability.

We also traced the changes in mechanical properties and micro-morphologies when soil samples were exposed to multiple wet-dry cycles, and the results indicated that modification with hydrophobic comonomer successfully improved water durability of treatment. In **Figure 5(a)**, the macroscopic appearances of soil samples after wet-dry showed that samples treated with PAAm-

EICP and poly(AAm-co-HEMA)-EICP have smoother surfaces with less visible micro-pores and are thus less crumbled after wet-redried comparing to previously reported PAAc-EICP treatment. We further examined the SEM images of soil samples treated by poly(AAm-co-HEMA)-EICP before and after up to 3 wet-dry cycles, as shown in **Figure 5(b)**. There is little change in micro-morphology after multiple wet-dry cycles, indicating that inter-particle binding by double network remained intact even after multiple wet-dry cycles.

To sum up, according to better vegetation compatibility, less volumetric change upon wetted, and stable microstructure after wet-dry cycles, we have proved that incorporation of poly(AAm-co-HEMA) is a more suitable soil stabilization choice under wet condition than both PAAc and PAAm.

3.5 Durability: Strength loss after wetting and drying cycles

To evaluate the improvement in water durability, we compared the mechanical performance via unconfined compressive strength (UCS) tests before and after rewetting the soil samples treated by PAAm-EICP derivatives and previously reported PAAc-EICP stabilizers for comparison. The averaged peak strengths and corresponding strains are shown in **Table 2**, and the representative stress-strain curves are shown in **Figure 6**. The zigzag fluctuations in stress-strain curves was observed in the brittle samples when detachment of sand particles and small chunks at the edges of the samples occurred during compressive loading before the whole sample fails. Before rewetting, for the freshly made and dried samples, all PAAm-EICP derivatives treated soil showed a more robust behavior comparing to PAAc-EICP treated samples, with 200%~250% of strength enhancement, while sacrificing 60% of the maximum strain and ~25% of elastic modulus.

In **Figure 7,** to compare the mechanical performance before and after wet-dry, the peak strength, strain at peak strength, and toughness of the samples after one wet-dry cycle and freshly prepared were recorded accordingly. The ratio of each property after wet-dry to freshly prepared were then calculated and compared. As shown in **Figure 7 (b),** after wet and redried, samples treated with PAAc-EICP lost 80% of deformability (strain at peak strength) and exhibited highly brittle mechanical behavior; by contrast, samples treated with PAAm-EICP and P(AAm-co-HEMA)-EICP increased in ductility and deformability. Loss of deformability indicated a significant loss of adhesion between polymer network and soil particles, which caused by the enormous polymer volume change upon water-induced swelling and shrinkage. Therefore, by introducing PAAm and HEMA with less swelling behavior as the organic network, we effectively retained the ductility and the peak strength of the treated soil after wet-dry cycle. These results and explanation are verified by their macroscopic structures in **Figure 5**. PAAc-EICP treated soil became porous (**Figure 5 (a)**) from polymer swelling and this resulted in crumbled structure after wet-dry cycle; by contrast, PAAm-EICP treated samples remain intact as revealed by the microstructures shown in **Figure 5 (b-d)**. This improvement can be attributed to the non-charged nature of PAAm in water, which effectively reduced the swelling, compared to the negatively charged PAAc with high swelling ratio. Hence, with the high ductility well retained or even increased due to minimized loss of organic network adhesion, PAAm and its copolymers are more water-durable choices in the organic-inorganic double-network stabilizer than PAAc. Furthermore, the peak strengths and the respective strains of these sandy soil samples treated by ~5 wt% of our copolymers and EICP reaction lie at ~4000 kPa and ~3%, respectively. This reported method has achieved significantly improved mechanical performance, especially more ductile and resilient than the state-of-the-art polymeric fiber reinforcement (Ilies et al., 2017; Liu et al., 2017; Oncu

and Bilsel, 2017) or treatments using inorganic or organic single-network stabilizer alone (Chang et al., 2016; Chang et al., 2015a; Choi et al., 2017).

Among the poly(AAm-co-HEMA)-EICP treated samples, we also observed that the peak strength of samples treated with PAAm-EICP was well maintained, and those treated with poly(AAm-co-HEMA) effectively improved by 5-16% (**Figure 7 (a)**). With increasing HEMA:AAm ratio, the treated soil sample become more robust but less deformable. Thus, copolymerization of HEMA with AAm also allows for fine-tuning between robustness and ductility by varying the HEMA:AAm ratio. This good tunability and customizability make our modular-designed copolymers more flexible to fit various applications.

3.6 Ductility: Toughness

To evaluate impact-damping ability, we also calculated the toughness of treated soil samples by integrating the area below stress-strain curves before peak strength, and compare the results before and after samples were wet and redried. In **Figure 8**, after one wet-dry cycle, samples treated with PAAc-EICP lost over 80% of its original toughness, while samples treated with PAAm-EICP and poly(HEMA-co-HEMA)-EICP showed increased toughness up to 229% of the original value. To sum up, soil stabilizer utilizing both PAAm-EICP and poly(AAm-co-HEMA)-EICP are superior to PAAc-EICP in terms of better sustainability of both mechanical strength and overall energy-damping capability (i.e., toughness), which lead to dramatically improved water resistance and durability especially in wet condition.

By comparing the toughness of samples with different HEMA contents, we also observed that incorporating more HEMA co-monomer within poly(HEMA-co-HEMA) causes decrease in soil sample overall toughness as well as smaller toughness improvement after wet-dry cycle. Therefore, to balance the overall toughness and water durability, an optimum HEMA:AAm ratio can be found at around 10%. Summarizing the toughness data with peak strength, strain at peak strength and elastic modulus in previous section, the incorporation of HEMA in the PAAm-EICP stabilizer makes the treated dry soil more rigid and strong, owing to polyHEMA's rigid nature, as the hydrophobic methyl side on polyHEMA turns outward around its central carbon under dry condition.

3.7 Long-term heat durability

Since the dust problem is mainly occur in arid area, for practical application, it is crucial to keep the polymer networks intact during exposure to ambient heat. As shown in **Figure 9**, all mechanical properties of poly(AAm-co-30% HEMA) treated samples slightly increased after 30 days of thermal exposure at 50°C, which possibly arose from continuous hardening of polymer under elevated temperature. This indicated good long-term thermal durability in terms of mechanical strength.

4. Conclusions

In summary, we have achieved our design concept of the "D^3 soil stabilizer", which features high ductility and durability via organic-inorganic double-network, by replacing traditional hydrogel with poly(AAm-co-HEMA) copolymers. These exceptional properties were verified by analyzing the observations and quantitative data from SEM image, EDS and powder

XRD spectrum, UCS tests, wet-dry cycle degradation tests, and long-term thermal stability tests. These results proved this design to be effective in significantly improving the ductility, toughness and water-durability of current stabilization method with high cohesion strength for dust suppression. We have also demonstrated the ability of precise and tunable solidification, as well as the flexibility of tuning soil physical properties by varying copolymer composition. These extra benefits accompanied with excellent water-durability enable our treatment method to be utilized in situations where pollutant erosion into the drain should be avoided and impact to surroundings should be controlled, such as drainage basin and mine tailings, to prevent soil erosion, and minimized stabilizer loss, and being adaptive to broader environmental conditions.

ACKNOWLEDGMENTS

This work was supported by the National Science Foundation under grant CMMI-1742759 and grant CMMI-1233658. The authors are grateful for the NSF support. Any opinions or positions expressed in this paper are the opinions and positions of the authors only, and do not reflect any opinions or positions of the NSF.

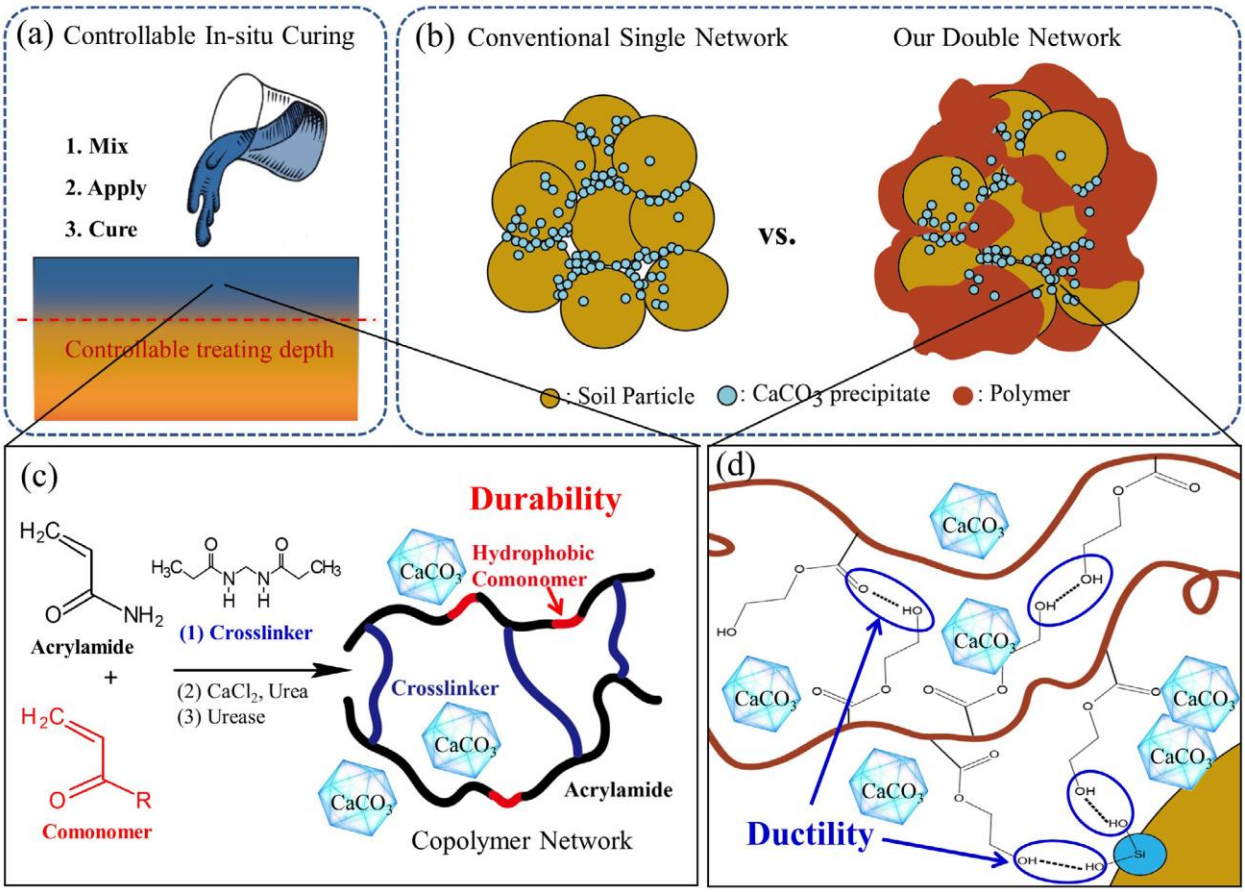

Figure 1: Design concept of the durable and ductile double-network (D^3) dust suppressant: (a) in-situ curing of liquid-form agent of D^3 dust suppressant with tunable curing time results in controllable treatment depth, (b) improved binding ability with carbonate-polymer double network. Rationally designed copolymerization achieves (c) improved water durability with reduced polymer swelling and (d) good ductility with reversible intermolecular hydrogen bonds (shown in dashed lines).

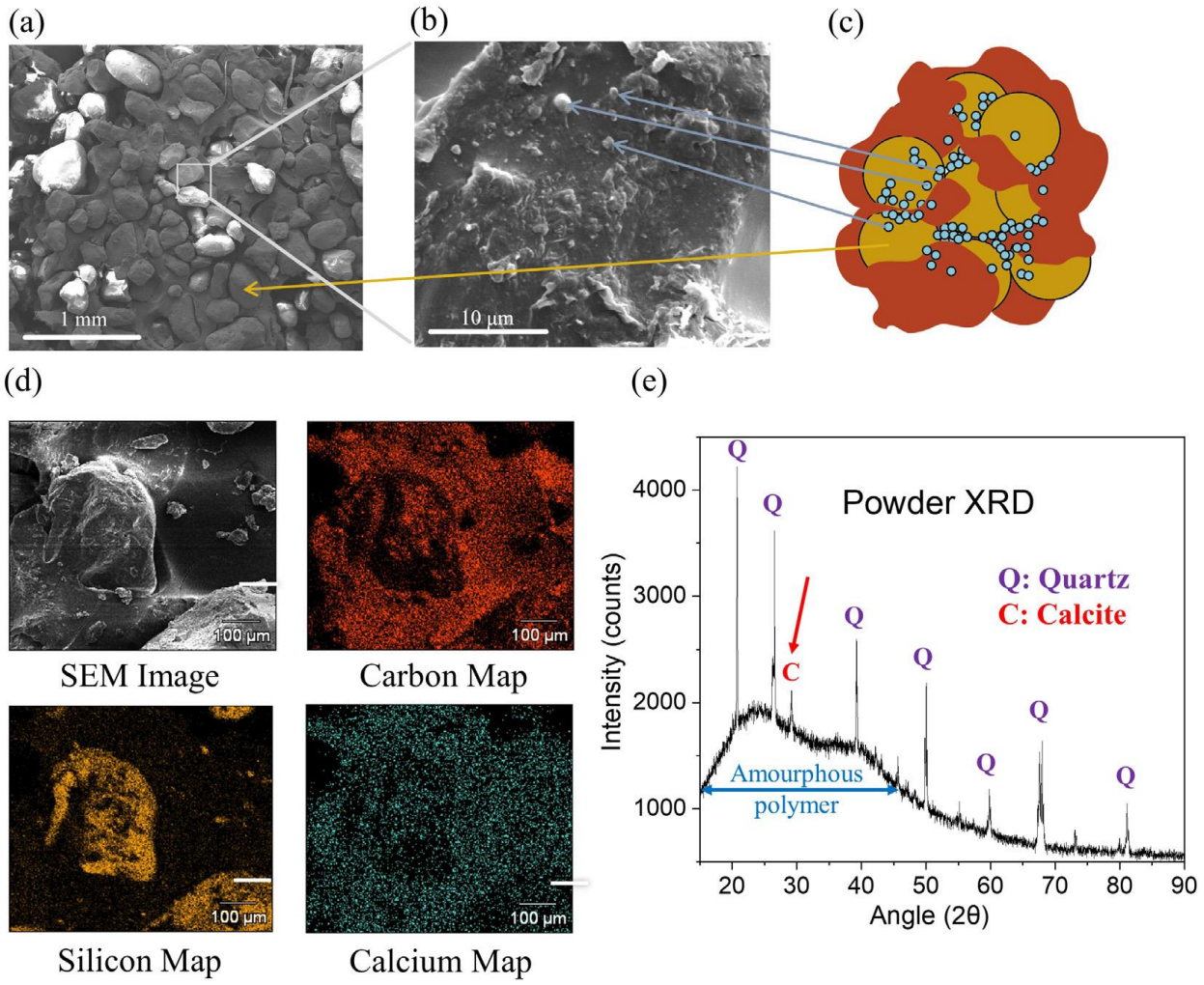

Figure 2: SEM images showing microstructure of (a) treated soil particle, reinforced by polymer network and (b) calcium precipitate. (c) Conceptual image depicting distribution of each composition. (d) The conceptual image in (c) is based on our observation from EDS mapping of carbon, silicon and calcium. (e) Powder XRD spectrum of supernatent showing characteristic peaks of calcium carbonate in rhombohedral calcite form at 2θ=29° (symbolled with C). The broad hill is originated from the amorphous polymer, and the rest of peaks (symbolled with Q) are originated from quartz.

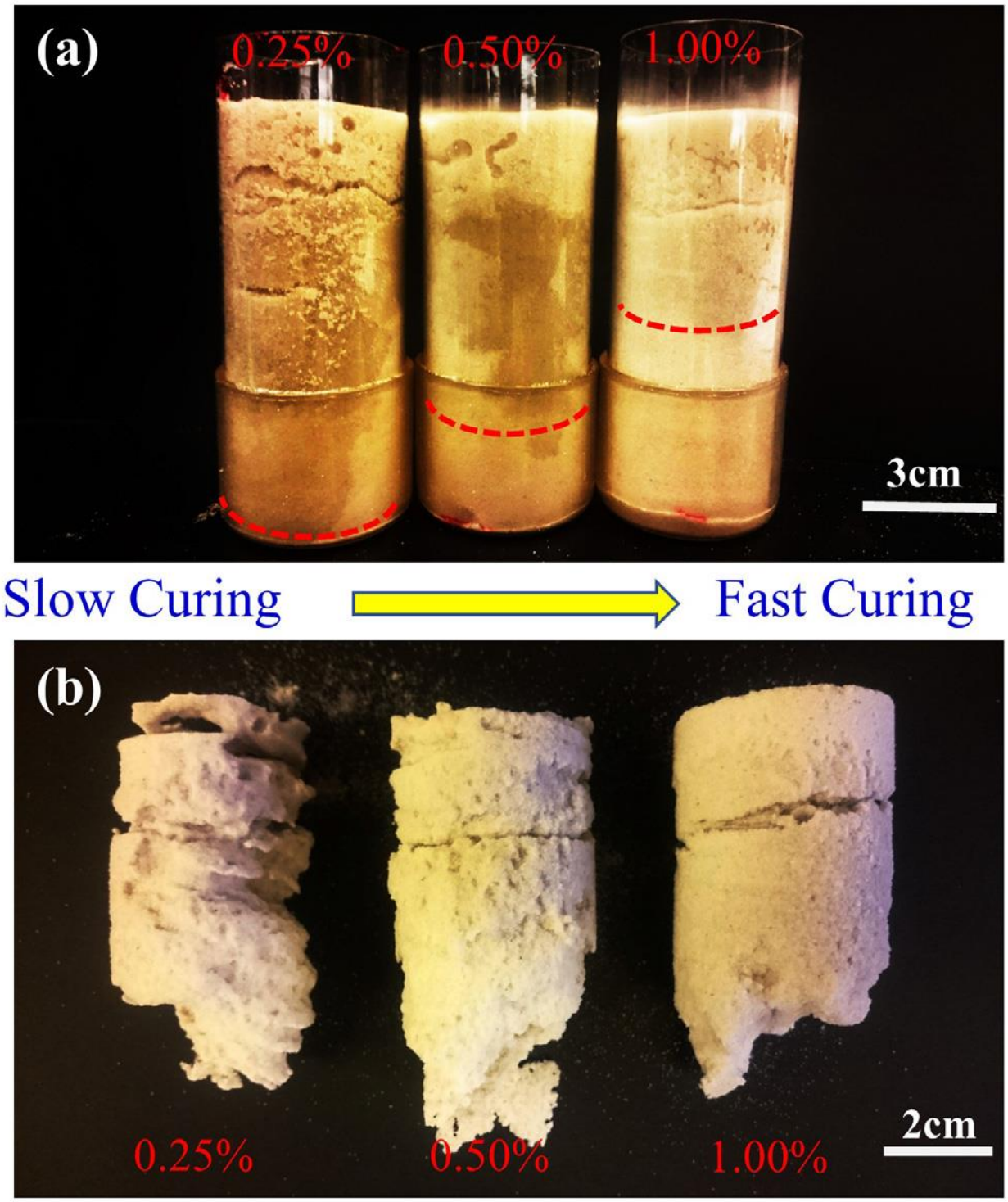

Figure 3: Soil samples treated with slower hardening (far-left) to faster hardening (far-right). (a) shows different, controllable solution-infiltration depth and (b) shows the actual treatment depth.

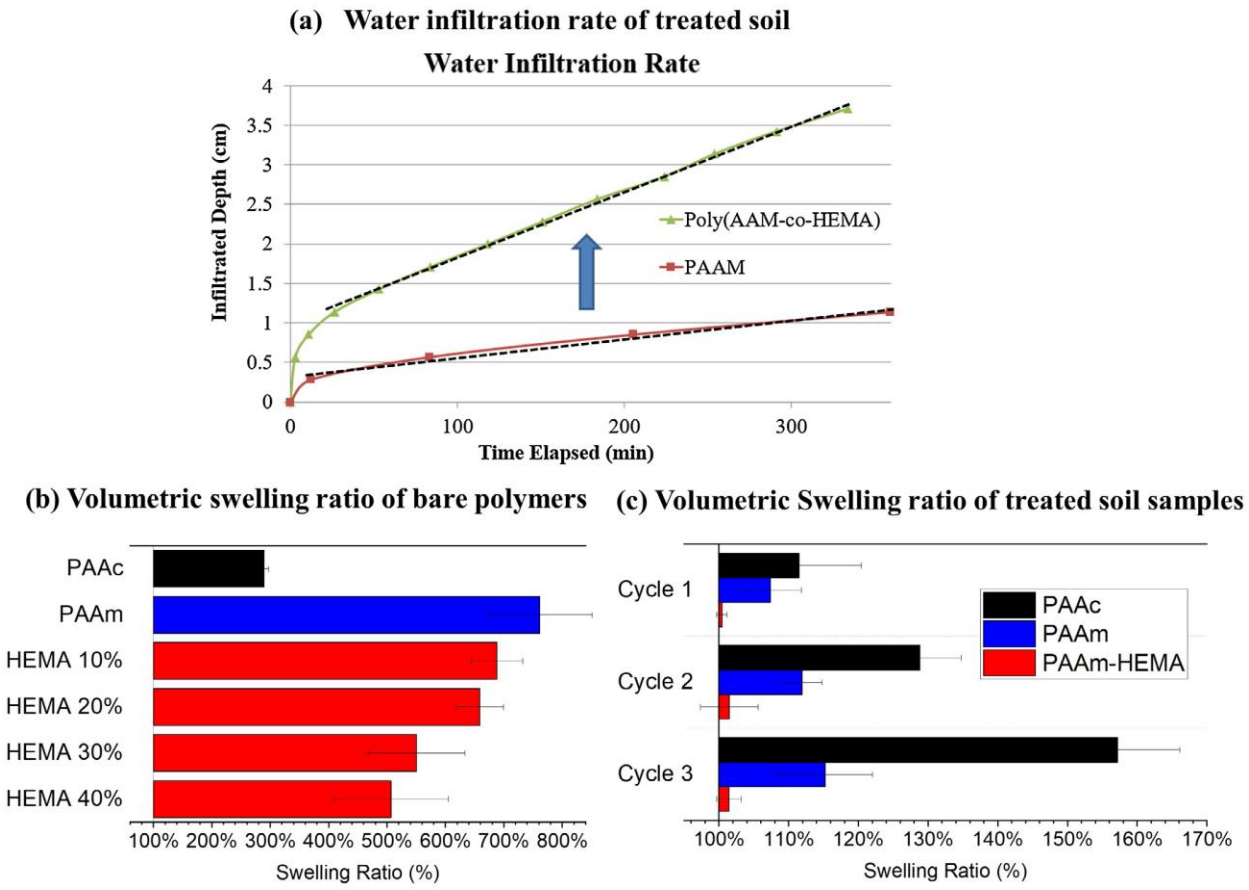

Figure 4: (a) Water infiltration rate conducted on soil samples treated with PAAm-EICP (red line) and poly(AAm-co-HEMA)-EICP (green line). (b) Swelling ratio (w/w) of poly(AAm-co-HEMA) copolymers are reduced with higher HEMA content. (c) Volumetric swelling behavior of PAAc-EICP treated samples become worse after multiple wet-dry cycles, while poly(AAm-co-HEMA)-EICP treated samples remain nearly un-swollen.

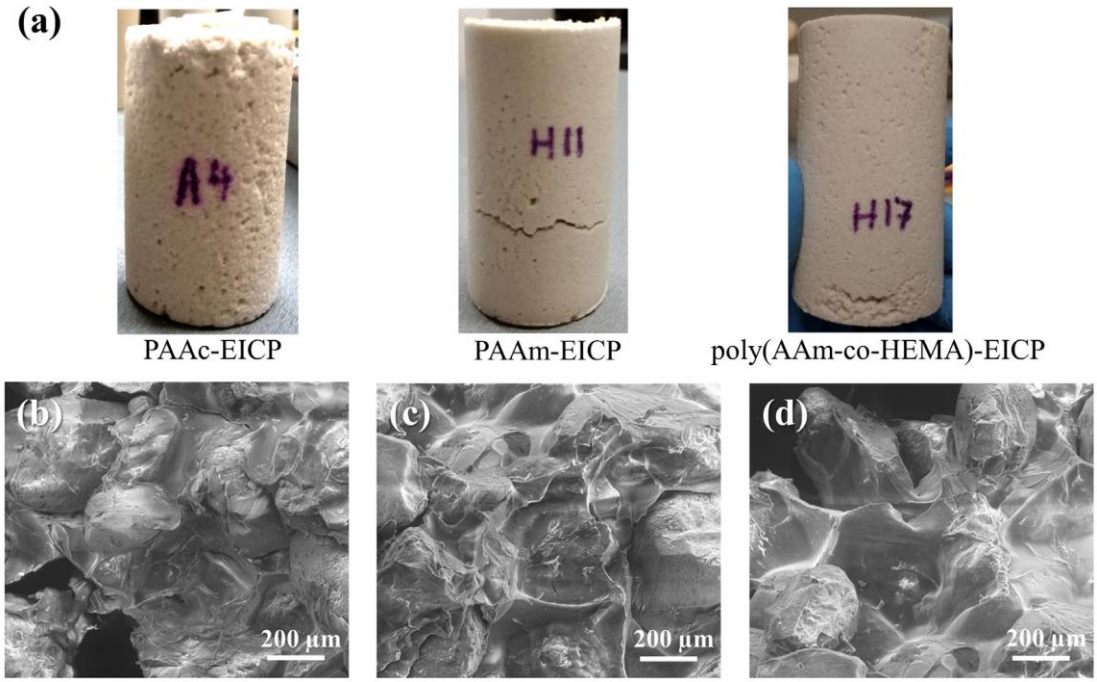

Figure 5 (a) Appearance of soil samples treated with PAAc-EICP, PAAm-EICP and poly(AAm-co-HEMA)-EICP. The numerous visible pores on PAAc-EICP and PAAm-EICP treated samples are caused by polymer swelling. SEM images of poly(AAm-co-HEMA)-EICP treated soil samples (b) before wet-dry cycles, (c) after 1 cycle, and (d) after 3 cycles. Little degradation of these binding networks occurred.

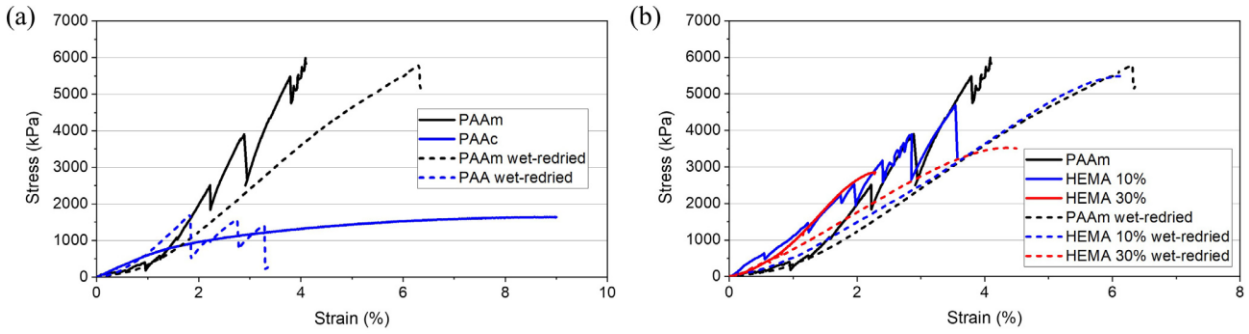

Figure 6: The UCS stress-strain curves of (a) PAAc-EICP and PAAm-EICP treated samples, and (b) PAAm-EICP and poly(AAm-co-HEMA)-EICP treated samples.

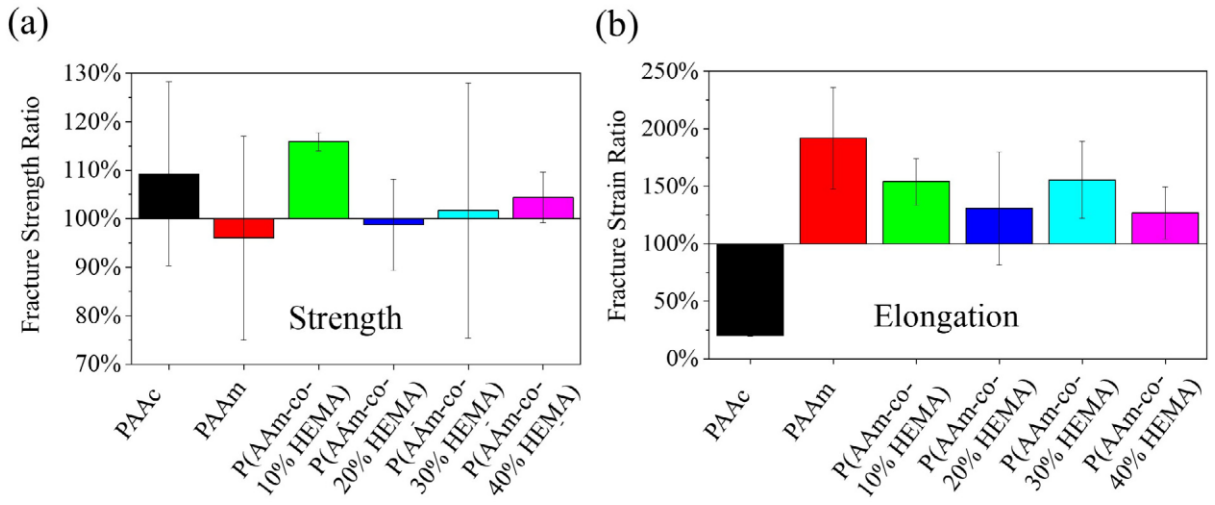

Figure 7: Comparison of (a) fracture strength and (b) strain at fracture before and after wet-dry process. The ratios are taken as the mechanical properties after wet-dried over their original values. The deformability can be retained when incorporating PAAm and poly(AAm-co-HEMA) copolymers. Characteristics also varies with different HEMA:AAm ratio.

(a)

Properties / Samples	Original	Rewet-redried	Change
	Toughness (J/m³)	Toughness (J/m³)	%
P(AAm-co-10% HEMA)	115150.30	14235.70	12.36%
P(AAm-co-20% HEMA)	85582.34	170904.80	199.70%
P(AAm-co-30% HEMA)	62751.64	143812.50	229.18%
P(AAm-co-40% HEMA)	68364.55	97182.19	142.15%
P(AAm-co-10% HEMA)	46591.83	78918.29	169.38%
P(AAm-co-20% HEMA)	61134.05	81345.21	133.06%

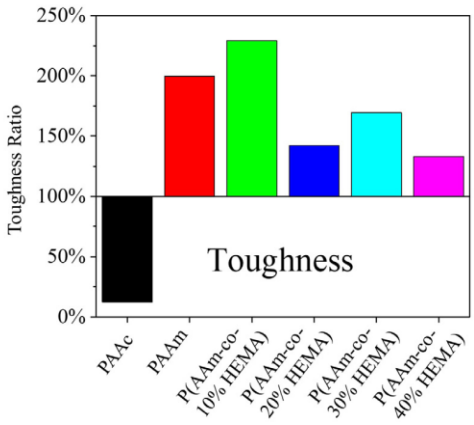

Figure 8: Toughness of soil samples treated with (a) different recipes and their respective change after wet-dry process, and (b) bar chart comparing the toughness change of all samples. Samples treated with PAAc-EICP lost over 80% of its original toughness, while samples treated with PAAm-EICP and poly(AAm-co-HEMA)-EICP showed increased toughness.

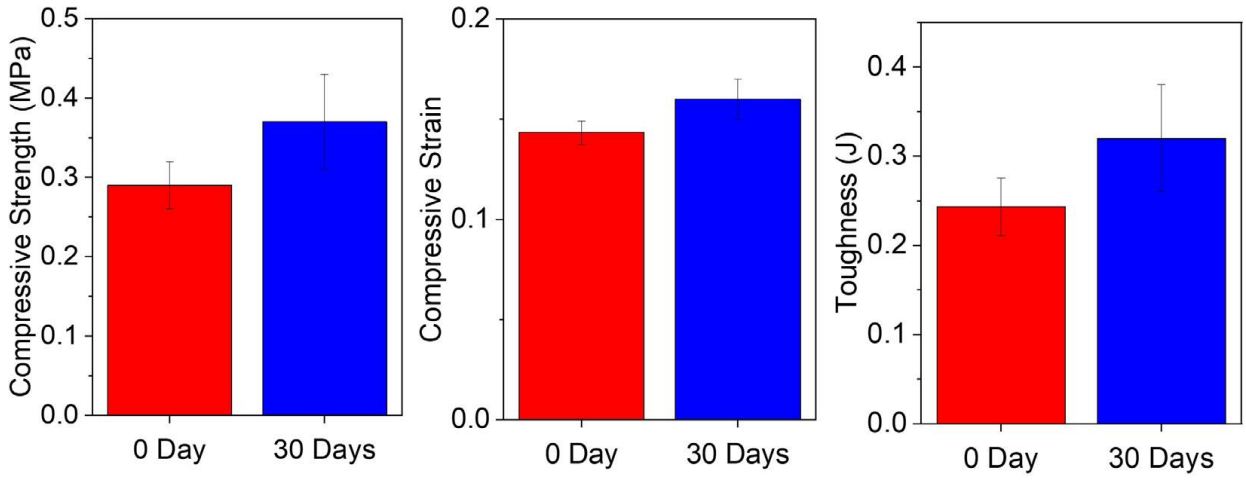

Figure 9: Long term stability test: the mechanical properties of poly(AAm-co-30% HEMA) treated soil after 30 days under 50°C well maintained even with slight increase.

Reference:

Andersen, F.A., 2005. Amended final report on the safety assessment of polyacrylamide and acrylamide residues in cosmetics. International Journal of Toxicology 24, 21-50.

ASTM International, W.C., PA, 2018. ASTM D3385-18 Standard Test Method for Infiltration Rate of Soils in Field Using Double-Ring Infiltrometer.

Bang, S.S., Bang, S., Frutiger , S., Nehl , L.M., and Comes , B.L., 2009. Application of Novel Biological Technique in Dust Suppression, Transportation Research Board 88th Annual Meeting, Washington DC, United States, pp. 0831.

Barvenik, F.W., 1994. POLYACRYLAMIDE CHARACTERISTICS RELATED TO SOIL APPLICATIONS. Soil Science 158(4), 235-243.

Berndt, W.O., Bergfeld, W.F., Boutwell, R.K., Carlton, W.W., Hoffmann, D.K., Schroeter, A.L., Shank, R.C., 1991. FINAL REPORT ON THE SAFETY ASSESSMENT OF POLYACRYLAMIDE. Journal of the American College of Toxicology 10(1), 193-203.

Bondietti, M., Murphy, D., Jenkins, K., Burger, R., 2004. Research on the stabilisation of two different materials using bitumen emulsion and cement, Proceedings of the 8th Conference on Asphalt Pavements for Southern Africa (CAPSA'04). Citeseer, pp. 16.

Chang, I., Im, J., Cho, G.C., 2016. Introduction of Microbial Biopolymers in Soil Treatment for Future Environmentally-Friendly and Sustainable Geotechnical Engineering. Sustainability 8(3).

Chang, I., Im, J., Prasidhi, A.K., Cho, G.C., 2015a. Effects of Xanthan gum biopolymer on soil strengthening. Construction and Building Materials 74, 65-72.

Chang, I., Prasidhi, A.K., Im, J., Cho, G.C., 2015b. Soil strengthening using thermo-gelation biopolymers. Construction and Building Materials 77, 430-438.

Chang, I., Prasidhi, A.K., Im, J., Shin, H.D., Cho, G.C., 2015c. Soil treatment using microbial biopolymers for anti-desertification purposes. Geoderma 253, 39-47.

Chen, R., Lee, I., Zhang, L.Y., 2015. Biopolymer Stabilization of Mine Tailings for Dust Control. Journal of Geotechnical and Geoenvironmental Engineering 141(2).

Childs, A., Li, H., Lewittes, D.M., Dong, B., Liu, W., Shu, X., Sun, C., Zhang, H.F., 2016. Fabricating customized hydrogel contact lens. Scientific Reports 6.

Choi, S.G., Chu, J., Brown, R.C., Wang, K., Wen, Z., 2017. Sustainable Biocement Production via Microbially Induced Calcium Carbonate Precipitation: Use of Limestone and Acetic Acid Derived from Pyrolysis of Lignocellulosic Biomass (vol 5, pg 5183, 2017). Acs Sustainable Chemistry & Engineering 5(8), 7449-7449.

Durairaj, S., Janaki Sundaram, S., 2015. Shear improvement in soft soil using fiber in a random manner. Journal of Chemical and Pharmaceutical Sciences 8(4), 798-800.

Eith, A.W., Koerner, R.M., 1992. FIELD-EVALUATION OF GEONET FLOW-RATE (TRANSMISSIVITY) UNDER INCREASING LOAD. Geotextiles and Geomembranes 11(4-6), 489-501.

Federation, W.E., Engineers, A.S.C., 1998. Urban Runoff Quality Management. WEF.

Firoozi, A.A., Olgun, C.G., Baghini, M.S., 2017. Fundamentals of soil stabilization. International Journal of Geo-Engineering 8(1).

Foley, G., Cropley, S., Giummarra, G., Ltd, A.T.R., 1996. Road Dust Control Techniques: Evaluation of Chemical Dust Suppressants' Performance. ARRB Transport Research Limited.

Gao, G.R., Du, G.L., Sun, Y.N., Fu, J., 2015. Self-Healable, Tough, and Ultrastretchable Nanocomposite Hydrogels Based on Reversible Polyacrylamide/Montmorillonite Adsorption. Acs Applied Materials & Interfaces 7(8), 5029-5037.

Garrels, R.M., 1951. A Textbook of Geology. Harper.

Hamdan, N., Kavazanjian, E., Jr., 2016. Enzyme-induced carbonate mineral precipitation for fugitive dust control. Geotechnique 66(7), 546-555.

Hamdan, N., Zhao, Z., Mujica, M., Kavazanjian, E., He, X.M., 2016. Hydrogel-Assisted Enzyme-Induced Carbonate Mineral Precipitation. Journal of Materials in Civil Engineering 28(10).

Hamza, M.A., Anderson, W.K., 2002. Improving soil physical fertility and crop yield on a clay soil in Western Australia. Australian Journal of Agricultural Research 53(5), 615-620.

Hamza, M.A., Anderson, W.K., 2003. Responses of soil properties and grain yields to deep ripping and gypsum application in a compacted loamy sand soil contrasted with a sandy clay loam soil in Western Australia. Australian Journal of Agricultural Research 54(3), 273-282.

Hamza, M.A., Anderson, W.K., 2005. Soil compaction in cropping systems - A review of the nature, causes and possible solutions. Soil & Tillage Research 82(2), 121-145.

Horak, D., Cervinka, M., Puza, V., 1997. Hydrogels in endovascular embolization .6. Toxicity tests of poly(2-hydroxyethyl methacrylate) particles on cell cultures. Biomaterials 18(20), 1355-1359.

Ilies, N.M., Circu, A.P., Nagy, A.C., Ciubotaru, V.C., Kisfaludi-Bak, Z., 2017. Comparative Study on Soil Stabilization with Polyethylene Waste Materials and Binders. 10th International Conference Interdisciplinarity in Engineering, Inter-Eng 2016 181, 444-451.

Johnson, A.I., 1963. A field method for measurement of infiltration. 1544F.

Kavazanjian, E., Jr., Almajed, A., Hamdan, N., 2017. Bio-Inspired Soil Improvement Using EICP Soil Columns and Soil Nails. Grouting 2017: Grouting, Drilling, and Verification (288), 13-22.

Kavazanjian Jr, E., Iglesias, E., Karatas, I., 2009. Biopolymer soil stabilization for wind erosion control.

Koerner, R.M., 2012. Designing with Geosynthetics - 6Th Edition. Xlibris US.

Li, J.Y., Illeperuma, W.B.K., Suo, Z.G., Vlassak, J.J., 2014. Hybrid Hydrogels with Extremely High Stiffness and Toughness. Acs Macro Letters 3(6), 520-523.

Liu, J., Feng, Q., Wang, Y., Bai, Y.X., Wei, J.H., Song, Z.Z., 2017. The Effect of Polymer-Fiber Stabilization on the Unconfined Compressive Strength and Shear Strength of Sand. Advances in Materials Science and Engineering.

Liu, Y., Nie, W., Jin, H., Ma, H., Hua, Y., Cai, P., Wei, W., 2018. Solidifying dust suppressant based on modified chitosan and experimental study on its dust suppression performance. Adsorption Science & Technology 36(1-2), 640-654.

Meyer, F.D., Bang, S., Min, S., Stetler, L., S. Bang, S., 2011. Microbiologically-Induced Soil Stabilization: Application of Sporosarcina pasteurii for Fugitive Dust Control, 2011.

Mirzababaei, M., Arulrajah, A., Ouston, M., 2017. Polymers for stabilization of soft clay soils. Proceedings of the International Scientific Conference Transportation Geotechnics and Geoecology (Tgg-2017) 189, 25-32.

Mujah, D., Shahin, M.A., Cheng, L., 2017. State-of-the-Art Review of Biocementation by Microbially Induced Calcite Precipitation (MICP) for Soil Stabilization. Geomicrobiology Journal 34(6), 524-537.

Omidian, H., Park, K., Kandalam, U., Rocca, J.G., 2010. Swelling and Mechanical Properties of Modified HEMA-based Superporous Hydrogels. Journal of Bioactive and Compatible Polymers 25(5), 483-497.

Oncu, S., Bilsel, H., 2017. Influence of Polymeric Fiber Reinforcement on Strength Properties of Sand-stabilized Expansive Soil. Polymer-Plastics Technology and Engineering 56(4), 391-399.

Orts, W.J., Roa-Espinosa, A., Sojka, R.E., Glenn, G.M., Imam, S.H., Erlacher, K., Pedersen, J.S., 2007. Use of synthetic polymers and biopolymers for soil stabilization in agricultural, construction, and military applications. Journal of Materials in Civil Engineering 19(1), 58-66.

Paganyas, K.P., 1975. RESULTS OF THE USE OF SERIES K COMPOUNDS FOR THE CONTROL OF IRRIGATIONAL SOIL EROSION. Soviet Soil Science 7(5), 591-598.

Rai, U.S., Singh, R.K., 2004. Synthesis and mechanical characterization of polymer-matrix composites containing calcium carbonate/white cement filler. Materials Letters 58(1-2), 235-240.

Rauner, N., Meuris, M., Dech, S., Godde, J., Tiller, J.C., 2014. Urease-induced calcification of segmented polymer hydrogels - A step towards artificial biomineralization. Acta Biomaterialia 10(9), 3942-3951.

Rauner, N., Meuris, M., Zoric, M., Tiller, J.C., 2017. Enzymatic mineralization generates ultrastiff and tough hydrogels with tunable mechanics. Nature 543(7645), 407-+.

Schexnailder, P., Schmidt, G., 2009. Nanocomposite polymer hydrogels. Colloid and Polymer Science 287(1), 1-11.

Sun, J.Y., Zhao, X.H., Illeperuma, W.R.K., Chaudhuri, O., Oh, K.H., Mooney, D.J., Vlassak, J.J., Suo, Z.G., 2012. Highly stretchable and tough hydrogels. Nature 489(7414), 133-136.

Thoniyot, P., Tan, M.J., Karim, A.A., Young, D.J., Loh, X.J., 2015. Nanoparticle-Hydrogel Composites: Concept, Design, and Applications of These Promising, Multi-Functional Materials. Advanced Science 2(1-2).

Wang, X., Polymer-Modified Microbially Induced Carbonate Precipitation Treatment Method for Surface Erosion Prevention.

Wilson, R.G., Smith, J. A., Miller, S. D., & Fornstrom, K. J, 2001. Sugarbeet Production Guide. University of Nebraska–Lincoln.

Yuk, H., Zhang, T., Parada, G.A., Liu, X.Y., Zhao, X.H., 2016. Skin-inspired hydrogel-elastomer hybrids with robust interfaces and functional microstructures. Nature Communications 7.

Zhao, Z., Hamdan, N., Shen, L., Nan, H.G., Almajed, A., Kavazanjian, E., He, X.M., 2016. Biomimetic Hydrogel Composites for Soil Stabilization and Contaminant Mitigation. Environmental Science & Technology 50(22), 12401-12410.

Chapter 2. Highly Stretchable Self-Sensing Actuator Based on Conductive Photothermally-Responsive Hydrogel

Chapter 2 is reprinted with minor edition with permission from Elsevier Science & Technology Journals.

Chiao-Yueh Lo,[1,‡] Yusen Zhao,[1,‡] Cheolgyu Kim,[1,‡] Yousif Alsaid,[1] Roozbeh Khodambashi,[2] Matthew Peet,[3] Rebecca Fisher, [4,5] Hamid Marvi,[6] Spring Berman,[6] Daniel Aukes,[2] Ximin He[*,1]

[1]Department of Material Science and Engineering, University of California Los Angeles, Los Angeles, CA, 90095 USA

[2]The Polytechnic School, Ira A. Fulton Schools of Engineering, Arizona State University, Mesa, AZ, 85212 USA

[3]Department of Mechanical and Aerospace Engineering, Arizona State University, Tempe, AZ, 85287 USA

[4]School of Life Science, Arizona State University, Tempe, AZ, 85287 USA

[5]Department of Basic Medical Sciences, University of Arizona College of Medicine-Phoenix, Phoenix, AZ, 85004 USA

[6]School for Engineering of Matter, Transport and Energy, Arizona State University, Tempe, AZ 85287 USA

‡These authors contributed equally.

*Correspondence: Ximin He, ximinhe@ucla.edu

Keywords: photothermal responsive hydrogel, conducting polymer, LCST, strain sensor, self-monitoring, soft actuator, soft robotics

Abstract

Soft robots built with active soft materials have been increasingly attractive. Despite tremendous efforts in soft sensors and actuators, it remains extremely challenging to construct intelligent soft materials that simultaneously actuate and sense their own motions, resembling living organisms' neuromuscular behaviors. This work presents a soft robotic strategy that couples actuation and strain-sensing into a single homogeneous material, composed of an interpenetrating double-network of a nanostructured thermo-responsive hydrogel poly(N-isopropylacrylamide) (PNIPAAm) and a light-absorbing, electrically conductive polymer polypyrrole (PPy). This design grants the material both photo/thermal-responsiveness and piezoresistive-responsiveness, enabling remotely-triggered actuation and local strain-sensing. This self-sensing actuating soft material demonstrated ultra-high stretchability (210%) and large volume shrinkage (70%) rapidly upon irradiation or heating (13%/^{o}C, 6-time faster than conventional PNIPAAm). The significant deswelling of the hydrogel network induces densification of percolation in the PPy network, leading to a drastic conductivity change upon locomotion with a gauge factor of 1.0. The material demonstrated a variety of precise and remotely-driven photo-responsive locomotion such as signal-tracking, bending, weightlifting, object grasping and transporting, while simultaneously monitoring these motions itself via real-time resistance change. The multifunctional sensory actuatable materials may lead to the next-generation soft robots of higher levels of autonomy and complexity with self-diagnostic feedback control.

1. Introduction

Living organisms can sense external stimuli (exteroception) and their own movement (proprioception) while moving automatically in response to the environment, attributed to their somatosensory and neuromuscular systems. Specifically, human fingers and other entirely soft animal structures (e.g. octopus arms and elephant trunks) can perform complex tasks with serial movements. In contrast, man-made robots are conventionally rigid and accomplish sensory motion tasks by coupling sensors, external cameras, and actuators with computational control systems; these coupled systems enable motion-monitoring to provide feedback on locomotive gaits and terrain conditions[1]. For typical robots, achieving actuation with closed-loop control requires mounting sensing devices, such as encoders, accelerometers, triboelectric nanogenerators, or linear variable differential transformers. These complex multi-electronics integrations restrict the size miniaturization and higher-level motility[2].

Soft robots made of compliant materials can conform to their surroundings through continuous and dexterous maneuvers. Despite tremendous efforts, realizing intelligent soft actuators with self-sensing capabilities remains a challenge. Specifically, current state-of-the-art actuation strategies such as asymmetric expansion[3,4], pneumatic inflation[5], and hydraulic actuation[6] usually utilize materials that serve purely structural purposes and cannot themselves be stimulated by trigger signals; thus, they are unable to sense their own motions. To achieve self-sensing function in actuators, roboticists have physically laminated or embedded various sensing devices based on optical loss [7-9], capacitance[10], electroluminescence [10], triboelectricity [11], and piezoresistivity [3,10,12-18]. However, device damage at the interface can arise from modulus mismatch between the sensor

and actuator[19]. The sensing and actuation modules are also predefined, restricting deformation when dealing with a complicated and ever-changing environment.

To mimic the large deformation, fast environmental response, and multifunctional motion of living creatures, people have developed actuators made from new stimuli-responsive polymers such as liquid crystalline elastomers (LCEs)[20], electroactive polymers (EAPs)[21], shape memory polymers (SMPs)[22], and stimuli-responsive hydrogels[23]. These materials are intrinsically stimuli-responsive and are thus capable of realizing local deformation with high dexterity and complexity. Among these soft responsive polymers, hydrogels carry the potential to achieve multi-functionality due to their ability to experience significant volumetric change in response to a variety of environmental stimuli such as temperature[24,25], light[26], pH[27,28], electric field[29], and chemicals[30]. Their unique and attractive abilities as actuators has led to multifarious applications in soft robotics at various length scales ranging from micro-robots for drug delivery[31,32] to macro actuators for object manipulation[33,34]. Additionally, serving as sensors, hydrogels can withstand ultra-high tensile strains[35].

Stretchable polymeric matrices embedded with conductive fillers have been widely used as strain sensors due to their ultra-high stretchability, direct current (DC) compatibility, facile fabrication, and tunable deformation-dependence of resistivity achieved via changing the percolation of the conductive filler network. Carbon black[36], carbon nanotubes[37], graphene derivatives[38], and liquid metals[18] have been reported as effective conductive fillers, and their sensing range can reach up to 400% strain[39]. However, the immiscible filler particles in the composite naturally tend to aggregate during fabrication, hindering the adaptive movements and causing irreversible device damage[40]. Conducting polymers (CPs) offer promising alternatives as conductive and piezo-resistivity fillers due to their neuron-like electrical conductivity [41-43].

However, CPs are typically stiff and lack stretchability due to their huge, planar electron conjugating system and rigid molecular chains. One route to address the issues of elasticity and flexibility in both sensing and actuation systems is to homogeneously incorporate interconnected CPs in soft, flexible matrices.

By molecularly integrating the stimuli-responsive hydrogel and CPs, the actuation and sensing can be achieved simultaneously. Although CP-percolated hydrogels have been reported[44], self-sensing actuation remains unachieved because of the following issues: a) hydrogels are typically weak and CPs are brittle, leading to low flexibility and stretchability; b) diffusion of CPs into hydrogel network is slow using conventional solution-based fabrication techniques, resulting in a percolation only on the hydrogel skin[45]; c) actuation performance is usually diffusion-limited, with a slow response time of minutes to hours[46]. Hence, creating a CP-percolated stimuli-responsive hydrogel with high stretchability, high homogeneity, fast response, and capability for deformation sensing (proprioceptive and exteroceptive) is highly desired.

Herein, we have demonstrated a two-in-one functional hydrogel that couples independent actuation and strain-sensing capabilities from the photo-thermal-mechanical pathway and piezoresistive mechanism, respectively. The homogeneous CP-percolated double-network hydrogel was constructed by combining thermal-responsive, soft, and elastic poly(N-isopropylacrylamide) (PNIPAAm), the actuator component, with black conducting polymer polypyrrole (PPy), the light absorbing and piezoresistive component. The nano-structured PNIPAAm hydrogel enabled high stretchability (>210%), high response rate (6-fold faster than conventional PNIPAAm) and substantial volume change ($\triangle V/V=70\%$) in water. The PPy network was incorporated into the PNIPAAm with a modified solution method, which not only effectively

prohibited delamination and filler aggregation, but also provided uniform PPy distribution for samples up to 3 mm in thickness. We fabricated a compositionally and geometrically homogeneous cylindrical pillar as a light-responsive actuator, capable of rapidly and omni-directionally self-orienting towards incident near-infrared (NIR) light, resembling living plants' phototropic behavior. Meanwhile, the piezoresistive sensing behavior was observed up to >200% tensile strain and with a gauge factor (GF, $\Delta R/R_0/\varepsilon$) of 1.0, which are within the typical range for high-strain soft sensors[47]. Furthermore, the self-sensing actuation abilities have been demonstrated by photo-induced tracking, bending, weightlifting, grasping and object moving with real-time sensing via resistance change. With its demonstrated high sensitivity and actuation strain, this conductive self-sensing hydrogel can lay the foundation for unconventional soft robots with a self-diagnostic feedback-controlled higher level of autonomy.

2. Results and Discussion

To build a composite hydrogel actuator with self-sensing ability, we chose to combine PNIPAAm and PPy into a double-network as an exemplary material. PNIPAAm provides both thermo-responsive actuation and mechanical flexibility, while PPy acts as a photothermal transducer, piezoresistive sensor, and mechanical strengthener. Under light illumination, the optical energy is absorbed by PPy and converted into thermal energy, resulting in temperature increase of the material. When temperature increases over the lower critical solution temperature (LCST) of PNIPAAm, the resistivity of the hydrogel is significantly reduced as the PPy network becomes more compacted upon temperature-driven shrinkage of the PNIPAAm network (**Fig. 1a**)[48,49].

First, the PNIPAAm network was synthesized. To achieve large volume change under repeated shrinking and swelling, we molecularly synthesized and incorporated 2-hydroxyethyl methacrylate (HEMA)-functionalized poly(NIPAAm-co-AA) nanostructured hydrogel beads (nanogel) into the composite network as crosslinking sites. Particularly, HEMA is esterized with PAA blocks to provide non-reacted double bonds, which is used as bonding sites during crosslinking. Compared to traditional crosslinkers such as N, N'-methylenebis(acrylamide) (BIS), the nanogel crosslinker results in higher elasticity, faster thermal-responsive volume change rate, and larger volume change under deswelling.

Special considerations must be taken when introducing PPy into the as-prepared PNIPAAm hydrogel network. Conventionally, the diffusion of PPy into hydrogels is limited by PPy's relatively large and hydrophobic particle sizes[50] that are difficult to infiltrate into the hydrogel's nanomesh pores[45,51,52]. In addition, the highly exothermic PPy reaction unavoidably increases the local temperature above PNIPAAm's LCST, resulting in the local shrinkage of PNIPAAm that further hinders the diffusion of pyrrole monomers[53]. This process typically results in an inhomogeneous material with a conducting polymer-rich shell and non-conductive core (**Fig. 1b**). To solve the issue, we replaced the aqueous prepolymer solution with a DMSO solution, in which PNIPAAm exhibits an upper critical solution temperature (UCST) behavior and does not shrink upon heating[54]. The kinetics of polymerization is also greatly reduced, enabling the complete mixing of pyrrole with the oxidant prior to polymerization, otherwise impossible with a very fast reaction. Consequently, a much more uniform PNIPAAm/conducting polymer hybrid material was obtained (**Fig. 1b**).

Characterized by scanning electron microscopy (SEM), the nano-structured hydrogel without PPy (termed NanoH) presented a hierarchical porous structure (**Fig. 2b)**. The pore size was significantly larger than the control hydrogel crosslinked with BIS (termed BisH) (**Fig. 2a**). After incorporating NanoH with PPy, the hydrogel (termed c-NanoH) exhibited similar pore size and morphology to NanoH (**Fig. 2c**). Such relatively large pores provided paths of effective water diffusion, leading to the high response and recovery speeds of c-NanoH, in contrast to the BisH. To further confirm the successful PPy incorporation, we utilized FT-IR spectroscopy. The PPy-incorporated c-NanoH exhibited a specific peak at 1046 cm^{-1}, ascribed to the =C–H in-plane vibration of PPy (**Fig. 2d**). In comparison, NanoH without PPy did not show this specific peak.

To examine the deformation capability of the nanostructured hydrogels, we analyzed the temperature-dependent hydrogel shrinkage of c-NanoH, NanoH, and BisH after 15 min immersion in water of different temperatures. As shown in **Fig. 2e**, both NanoH and c-NanoH achieved large phase transition when heated to near the LCST (30°C~35°C), demonstrating a remarkable equilibrium volume change of 13%/°C, substantially higher than that of BisH (6%/°C). Note that the overall volume changes of both c-NanoH and NanoH were also significantly larger (70% and 84% shrinkage, respectively) than BisH (57% shrinkage). This enhanced deswelling performance possibly arose from the nano-sized crosslinking sites as well as the loosely crosslinked, flexible PNIPAAm chains grafting onto the nanogel[55]. Upon immersion in water at elevated temperatures, the flexible PNIPAAm chains can freely aggregate with the nanogel, leaving sufficient space for water to diffuse out of the network. The slightly decreased shrinkage of c-NanoH compared to NanoH can be attributed to the stiff and non-thermal-responsive PPy network, but the overall c-NanoH network was still more thermal-responsive than BisH. To further evaluate the thermal response rate, the three hydrogels were cut into 1.0 cm × 1.0 cm × 0.4 cm samples and swollen

sufficiently in water at 25°C followed by immersion in a hot water tank. The hydrogel volumes were recorded gradually with time, and the volumetric change rates were compared (**Fig. S1**). The initial volumetric shrinkage rates of NanoH (16.6%) and c-NanoH (23.6%) within the first 30 seconds were significantly faster than that of BisH (4.0%). This result was consistent with the larger pore sizes demonstrated by the SEM images in **Fig. 2 (a)~(c)**.

We utilized stress-strain curves from uniaxial stretching to characterize and describe the mechanical properties of the composite hydrogel. The fracture stress of the composite hydrogel after introducing a PPy network (c-NanoH) increased to 30 kPa, compared to 13 kPa for NanoH. Interestingly, c-NanoH also demonstrated an enhanced fracture strain of 210%, compared to 115% for NanoH (**Fig. 2f**). Although pure PPy is rigid and lacks elasticity, we speculate that this enhanced elastic behavior can be attributed to the interpenetration of PPy and NanoH networks. Because the PNIPAAm polymer chains are more entangled in DMSO while in-situ polymerizing PPy, the PNIPAAm polymeric chains are confined by PPy in the coil state. This higher degree of entanglement of polymeric chains and the nanostructure in the c-NanoH hydrogels resulted in improved elastic properties and stretchability[55].

To realize self-sensing capability, we utilized the resistivity change mechanism of c-NanoH upon stretching. The sensing measurement was conducted by connecting the c-NanoH hydrogel in a circuit. As depicted in **Fig. 3a**, the resistance change of c-NanoH under external strain or stimulated actuation can be attributed to two factors: 1) the structural effect, involving the passive elongation along the tensile direction and the Poisson contraction along the lateral direction. For a conducting polymer hydrogel, the resistance ratio follows $R/R_0 < \lambda^2$ due to the reorientation and alignment of coiled conducting polymer along the stretching direction, where R/R_0 is the normalized resistance under strain and λ is the axial stretch ratio[56]; 2) the density effect: in the

stimuli-induced shrinkage of the hydrogel network, PPy density is increased, and microstructure transits from a loosely compact, disconnected network to a highly compact, connected network. Such a highly compact state facilitates the overlap between delocalized π-orbitals and a higher probability for electrons to migrate via intra-chain migration and inter-chain hopping[44].

Under external stretching or compression, the PPy chains are stretched or contracted to modulate the resistance. Notably, we observed the structural effect under very small compression deformation (axial stress <1 kPa), as shown in **Fig. 3b (Video S1)**. The resistance change can also be approximated as linear. With respect to tensile stretching, the resistance continued to increase with strain. The resistivity calculated according to the dimensional change decreased at larger tensile strains **(Fig. 3c)**. This might be attributed to the chain alignment of the PPy chains along the stretching direction[57]. In **Fig. 3d,** the calculated gauge factor (i.e., the slope of ΔR/R vs. strain) increased with strain and reached a maximum value of 1.0 at the fracture point.

During passive mechanical deformation under external force, the hydrogel composite experiences no volume change. However, under (photo)thermal response, the volume actively shrinks locally at the response site. To monitor the resistance change under its active deformation, we fixed the hydrogel at two terminals to restrict the axial contraction and illuminated NIR light to induce photothermal shrinkage (**Fig. 3e**). The resistance was measured in real-time along the axial direction. Interestingly, it was observed that when the gel was photothermally heated, the resistance initially increased then abruptly decreased. The light actuation-recovery shown in Fig. 3e includes following three stages: The step I (0~20 sec) involved the rapid sample shrinkage and simultaneous resistance increase due to reduced cross-sectional area and internal stress along the restricted axial direction. However, the shrinkage is not sufficient to change the percolation network of PPy. The overall resistivity remained constant and the appeared resistance increased to

be stable. The step II (20~26 sec) involved a phase change of PPy, which triggered an abrupt further shrinkage (the cliff at 20 sec). However, the resistance change was opposite to the predicted geometric effect in the first step. It is proposed by the percolation conduction theory that, above such a threshold density, percolation conduction is enabled by the formation of a fully-continuous PPy network[58], rendering the composite significantly more conductive. This resistivity effect subsequently dominated over the geometric effect and resulted in decreased apparent resistance at larger shrinkage volumes. The step III (after 26 sec) showed that the sample geometry and resistance recovered to their initial values after the NIR source was switched off.

Fig. 4a and **Fig. 4b** depict the cyclic and reversible change of resistance under periodic stretching-releasing of c-NanoH samples. The response time was observed to be much less than 1 second, comparable to typical hydrogel strain sensors. To demonstrate the application as a practical sensor, a test was performed where c-NanoH served as an electronic skin affixed to the joint of a human forefinger, and the corresponding variations in resistance upon multi-cycle deformations were observed to be rapid and stable, as seen in **Fig. 4c**, **Fig. 4d**, **Fig. S3** and **Video S2**.

The interpenetrating PPy particles play several roles in the composite hydrogel, as pathways for electron transport and photothermal transducers. Underwater, we measured that the local temperature of hydrogel with PPy increased from 25℃ to as high as 38℃ within 20 seconds under NIR irradiation. We also demonstrated that increasing PPy concentration, exposure time, and illumination intensity can substantially improve the photothermal effect (**Figure S4**). Therefore, besides the function of strain sensing, the composite hydrogels exhibited photo-responsiveness via photo-thermal-mechanical conversion. The composite hydrogels are chemically homogeneous without an observed composition gradient, able to actuate with large flexibility. In addition, we synthesized c-NanoH hydrogel pillars with cylindrical geometry. When NIR light was illuminated

on the side of the pillar at an oblique angle, it was able to bend and self-orient towards the light direction. Such directional, asymmetric motion was attributed to the temperature gradient across the hydrogel by controlling appropriate light intensity[59]. As depicted in simulation snapshots in **Fig. 5**, when NIR laser is irradiated on the hydrogel pillar, a temperature gradient is generated across the pillar cross-section, in which the temperature on the illuminated side is elevated above the LCST while the temperature on the non-illuminated side remains lower than the LCST; this causes local shrinking solely on the illuminated side, ultimately resulting in precise pillar bending towards the light source.

Furthermore, this self-sensing actuator could perform omni-directional actuation due to its homogeneous and isotropic structure and local deformation, in contrast to conventional actuators with restricted directionality, anisotropic structure, and uniform deformation. Previously, we have reported isotropic responsive materials that successfully achieved phototropism in response to green and white light based on a negative feedback mechanism [60,61]. In this work, the cylindrical pillar exhibited rapid and omni-directional tracking performance stimulated by NIR light. The tracking capability was demonstrated at an incident light angle of 90°, showing precise control (**Fig. 5a**). The bending speed reached 34.6°/s. The diffusion time scale was in the range of seconds, which was an order of magnitude faster than the conventional PNIPAAm gels[62]. To further improve the response speed, one can manipulate the hydrogel morphology from closed pore to open pore, leading to enhanced water diffusion rate.[63-65] In addition, the hydrogel pillar could precisely track light sources from different azimuthal angles in the x-y plane, as demonstrated in **Fig. 5b**. The simulation results showed an excellent match with experimental observation (**Fig. 5c**, **Video S4)**. Therefore, the fast and omni-directional light-tracking behavior confirms the versatility of this photo-responsive actuator design.

Based on the separately demonstrated strain sensing with a broad actuation range and fast photothermal response, we further realized combined function of real-time self-sensing actuation. The c-NanoH hydrogel was illuminated with NIR light, causing multiple types of shape change, while the electrical signal across the two terminals of the hydrogel was collected; in this experiment, we were able to accurately monitor the shape change in real-time. Firstly, we mounted and dangled the hydrogel vertically, with electrodes attached to its two ends. The NIR light was illuminated horizontally on the body of the hydrogel. Various photo-actuated motions have been demonstrated, such as uniaxial shrinkage (**Fig. 6a**, **Video S5**) with a load attached to the gel bottom and light tracking (**Fig. 6b**, **Video S6**) while suspended in air. The hydrogel was strong enough in the air to lift a small weight from uniaxial shrinkage and to perform "sit-ups" from light tracking. During this process, we found that the resistance dropped dramatically during the deformation, due to the percolation-induced conductivity increase associated with the volume shrinking. We also demonstrated that the self-sensing actuation was stable and completely reversible from the submerged cyclic bending experiment, provided there is enough water (**Fig. 6c**, **Video S7**). The moving pattern of the bending angle coincided with the resistance change pattern, as shown in **Fig. 6d**. Furthermore, we showcased c-NanoH's self-sensing ability by remotely controlling an a hydrogel octopus arm with NIR light to curl up, grasp, and move an object with real-time motion sensing enabled by monitoring the resistance change between attached electrodes (**Fig. 6e**, **Video S8**). The capability of simultaneous self-sensing and actuation provides substantial potential for closed-loop control with no additional external components, helpful for actively predicting and manipulating the motion based on sensing signals. In addition, we anticipate that the future study of the work is going to differentiate the deformation modes for complex robotic application, which

can be achieved by incorporation of multiple self-sensing actuators component or embedding multiple pairs of electrodes in one hydrogel.

3. Conclusions

We presented a self-sensing actuator by in-situ polymerizing a conductive PPy polymer network inside an ultra-stretchable and rapid thermal-responsive nanostructured PNIPAAm hydrogel matrix. The self-monitoring actuator was realized by combining actuation and sensing capabilities into a single composite material. This unique design prevents potential cracking and long-term damage associated with modulus mismatch at the sensor-actuator interface. Precisely controlled local actuation was achieved by NIR laser illumination, where PPy acted as both photothermal transducer and electrical conductor. With a homogeneous structure, the hydrogel could exhibit various omni-directional and anisotropic locomotion through manipulating the light stimulus. Agile, delicate, and on-demand motions were achieved. The presented composite hydrogel was able to translate the local strain, curvature, bending angle, and surrounding heat into a more visualized quantitative electric signal. Thus, the presented self-sensing, photothermal responsive actuator provides a platform for intrinsic self-monitoring without the need for bulky external equipment, enabling unprecedented closed-loop control of miniature untethered soft robots.

Acknowledgements

All authors acknowledge ONR awards N000141712117. C. Lo, Y. Zhao, Y. Alsaid, and X.H. acknowledges N00014-18-1-2314, AFOSR awards FA9550-17-1-0311, FA9550-18-1-0449 and FA9550-20-1-0344, and NSF CAREER award 1724526.

Supplementary material

The Supplementary Material for this article can be found online at:

https://doi.org/10.1016/j.mattod.2021.05.008

References

1. McEvoy, M. A., and Correll, N., Science (2015) **347** (6228), 1261689

2. Yang, G.-Z., et al., Science robotics (2018) **3** (14), eaar7650

3. Amjadi, M., and Sitti, M., Advanced Science (2018) **5** (7), 1800239

4. Cheng, H. H., et al., Acs Nano (2016) **10** (10), 9529

5. Yang, D., et al., Advanced Materials Technologies (2016) **1** (3), 1600055

6. Yuk, H., et al., Nature communications (2017) **8**, 14230

7. To, C., et al., Highly Stretchable Optical Sensors for Pressure, Strain, and Curvature Measurement. In IEEE/RSJ International Conference on Intelligent Robots and Systems (IROS), Hamburg, GERMANY, (2015), pp 5898

8. Zhao, H., et al., IEEE Robotics Automation Magazine (2016) **23** (3), 55

9. Zhao, H., et al., Science Robotics (2016) **1** (1), eaai7529

10. Larson, C., et al., science (2016) **351** (6277), 1071

11. Yuan, X., et al., Soft tactile sensor and curvature sensor for caterpillar-like soft robot's adaptive motion. In Proceedings of the 2019 International Conference on Robotics, Intelligent Control and Artificial Intelligence, (2019), pp 690

12. Spina, F., et al., Flexible Printed Electronics (2019) **4** (3), 035001

13. Fang, X., et al., A Soft Actuator with Tunable Mechanical Configurations for Object Grasping Based on Sensory Feedback. In 2019 2nd IEEE International Conference on Soft Robotics (RoboSoft), IEEE(2019), pp 25

14. Elgeneidy, K., et al., Mechatronics (2018) **50**, 234

15. Truby, R. L., et al., Soft Robotic Fingers with Embedded Ionogel Sensors and Discrete Actuation Modes for Somatosensitive Manipulation. In 2019 2nd IEEE International Conference on Soft Robotics (RoboSoft), IEEE(2019), pp 322

16. Truby, R. L., et al., Advanced Materials (2018) **30** (15), 1706383

17. Wei, S., et al., J Journal of Materials Chemistry C (2019) **7** (22), 6786

18. Dickey, M. D., Advanced Materials (2017) **29** (27), 1606425

19. Yeo, J. C., et al., Advanced Materials Technologies (2016) **1** (3), 1600018

20. Zeng, H., et al., Advanced Materials (2018) **30** (24), 1703554

21. O'Halloran, A., et al., Journal of Applied Physics (2008) **104** (7), 9

22. Liu, C., et al., Journal of Materials Chemistry A (2007) **17** (16), 1543

23. Jeon, S.-J., et al., Accounts of Chemical Research (2017) **50** (2), 161

24. Chen, L., et al., Soft Matter (2010) **6** (12), 2708

25. Zhang, X. B., et al., Nano Letters (2011) **11** (8), 3239

26. Ma, C., et al., Advanced Functional Materials (2016) **26** (47), 8670

27. Schmaljohann, D., Advanced Drug Delivery Reviews (2006) **58** (15), 1655

28. De, S. K., et al., Journal of Microelectromechanical Systems (2002) **11** (5), 544

29. Han, D., et al., Acs Applied Materials & Interfaces (2018) **10** (21), 17512

30. Matsumoto, A., et al., Biomacromolecules (2004) **5** (3), 1038

31. Qiu, Y., and Park, K., Advanced Drug Delivery Reviews (2001) **53** (3), 321

32. Ang, K. L., et al., Materials Science & Engineering C-Biomimetic and Supramolecular Systems (2007) **27** (3), 347

33. Mori, Y., et al., Journal of Materials Science (1997) **32** (2), 491

34. Zhao, L., et al., Acs Applied Materials & Interfaces (2017) **9** (13), 11866

35. Yang, C., and Suo, Z., Nature Reviews Materials (2018) **3** (6), 125

36. Wu, X. D., et al., Advanced Functional Materials (2016) **26** (34), 6246

37. Zhao, J. H., et al., Composites Part a-Applied Science and Manufacturing (2013) **48**, 129

38. Liu, H., et al., Journal of Materials Chemistry C (2016) **4** (1), 157

39. Ryu, S., et al., Acs Nano (2015) **9** (6), 5929

40. Lei, Z., and Wu, P., Nature communications (2019) **10** (1), 1

41. Cochrane, C., et al., Sensors (2007) **7** (4), 473

42. Yamada, T., et al., Nature Nanotechnology (2011) **6** (5), 296

43. Hu, N., et al., Carbon (2010) **48** (3), 680

44. Shi, Y., et al., Advanced Functional Materials (2015) **25** (8), 1219

45. Wang, K., et al., Advanced Material (2015) **27** (45), 7451

46. Koetting, M. C., et al., Materials Science and Engineering: R: Reports (2015) **93**, 1

47. Jayathilaka, W., et al., Advanced Materials (2019) **31** (7)

48. Lai, P. T., et al., Ieee Electron Device Letters (1999) **20** (11), 589

49. Bentley, J. P., Journal of Physics E-Scientific Instruments (1984) **17** (6), 430

50. Harreld, J., et al., Journal of Non-Crystalline Solids (1998) **225** (1), 319

51. Guo, Y., et al., Small (2018) **14** (14), 1704497

52. Sun, K., et al., ACS Sustainable Chemistry & Engineering (2018) **7** (1), 165

53. Blinova, N. V., et al., European Polymer Journal (2007) **43** (6), 2331

54. Yamauchi, H., and Maeda, Y., The Journal of Physical Chemistry B (2007) **111** (45), 12964

55. Xia, L.-W., et al., Nature communications (2013) **4** (1), 1

56. Lee, Y. Y., et al., Advanced materials (2016) **28** (8), 1636

57. Wang, Y., et al., Science advances (2017) **3** (3), e1602076

58. Liu, H., et al., Journal of Materials Chemistry C (2018) **6** (45), 12121

59. Qian, X., et al., Nature Nanotechnology (2019), 1

60. He, X. M., et al., Nature (2012) **487** (7406), 214

61. Zhao, Y., et al., Science Robotics (2019) **4** (33), eaax7112

62. Gil, E. S., et al., Langmuir (2010) **26** (19), 15614

63. Khodambashi, R., et al., Advanced Materials (2021), 2005906

64. Alsaid, Y., et al., Advanced Materials (2021), 201701938

65. Wu, S., et al., EcoMat (2021), 1

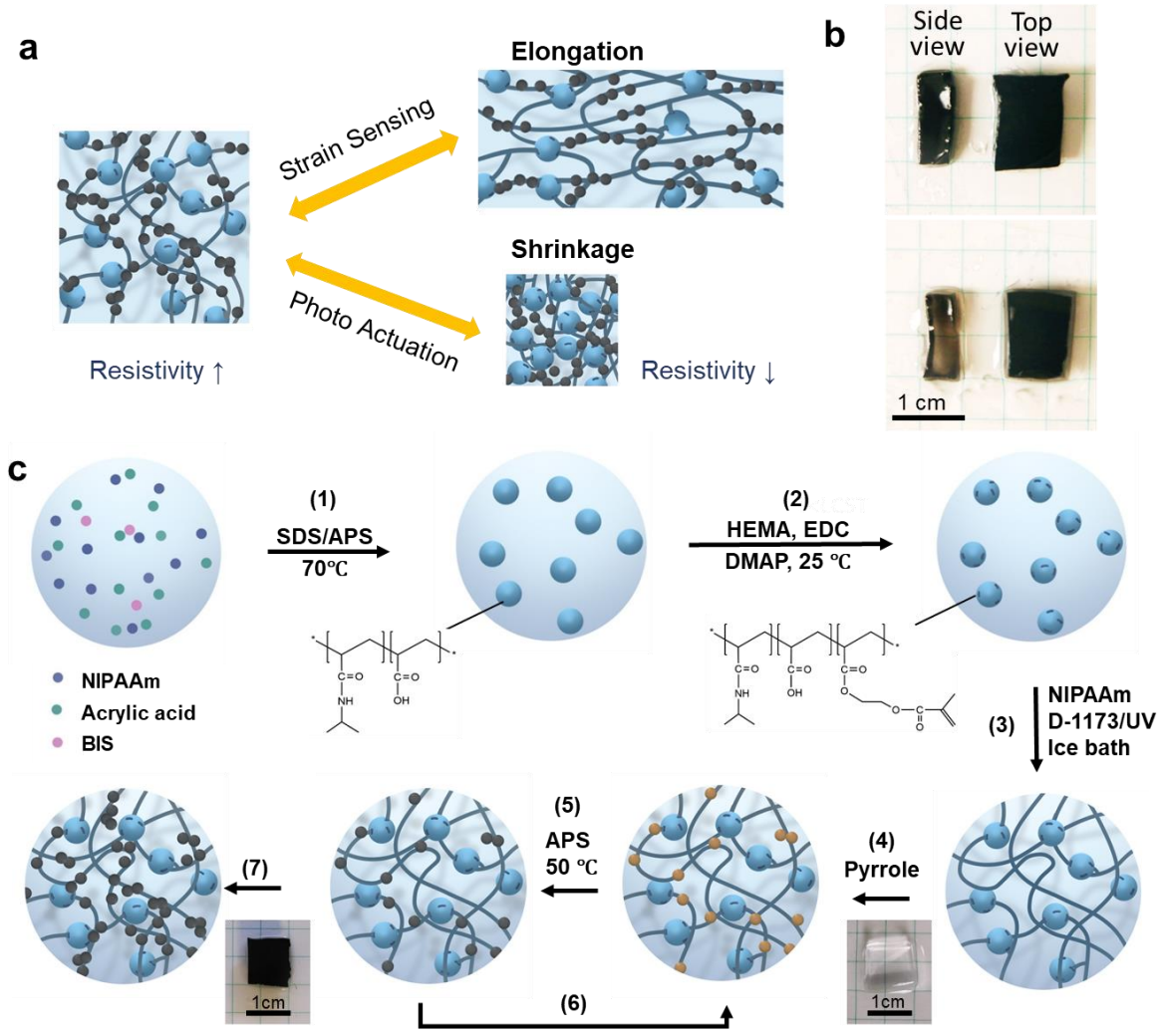

Figure 1. (a) Schematic of mechanism of the self-sensing actuator: Resistivity change of conducting polymer network when exposed to external stress or thermal stimulated volumetric change. (b) Comparison of the conventional synthesis method with poor PPy distribution in the PNIPAAm hydrogel (bottom) with the modified method for homogeneous PPy loading throughout the network (top) (c) Fabrication procedure of P(NIPAAm-co-AA) nanogels and c-NanoH.

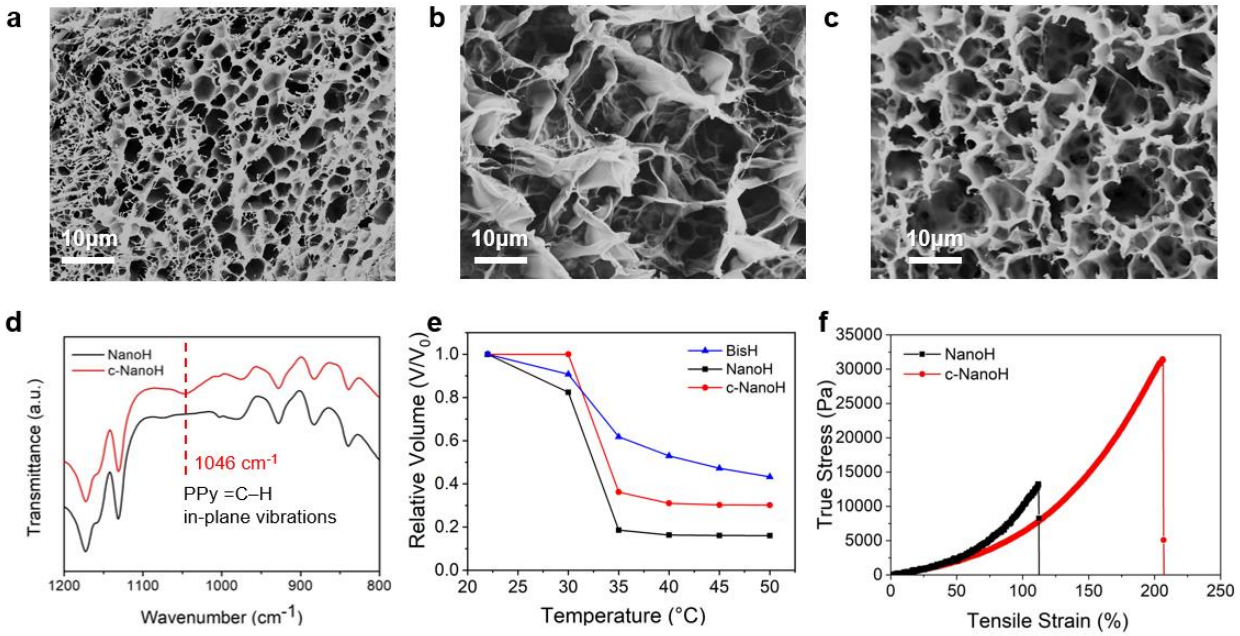

Figure 2. SEM images of (a) conventional BIS-crosslinked PNIPAAm hydrogel (BisH), exhibiting relatively small pores, (b) nanogel-crosslinked PNIPAAM hydrogel (NanoH with large pore crosslinked by nanogel, and (c) c-NanoH after PPy incorporation. Larger porous structure with nanogel enables faster water exchange and phase transition. (d) FTIR spectrum of NanoH before and after PPy incorporation: PPy peak at 1046cm^{-1} confirmed PPy in c-NanoH. (e) Equilibrium deswelling ratio of BisH, NanoH, and c-NanoH from 20 ℃ to 50 ℃. (f) Tensile stress-strain curves of nano-structured hydrogels showing enhanced elongation and fracture strength after coating with PPy.

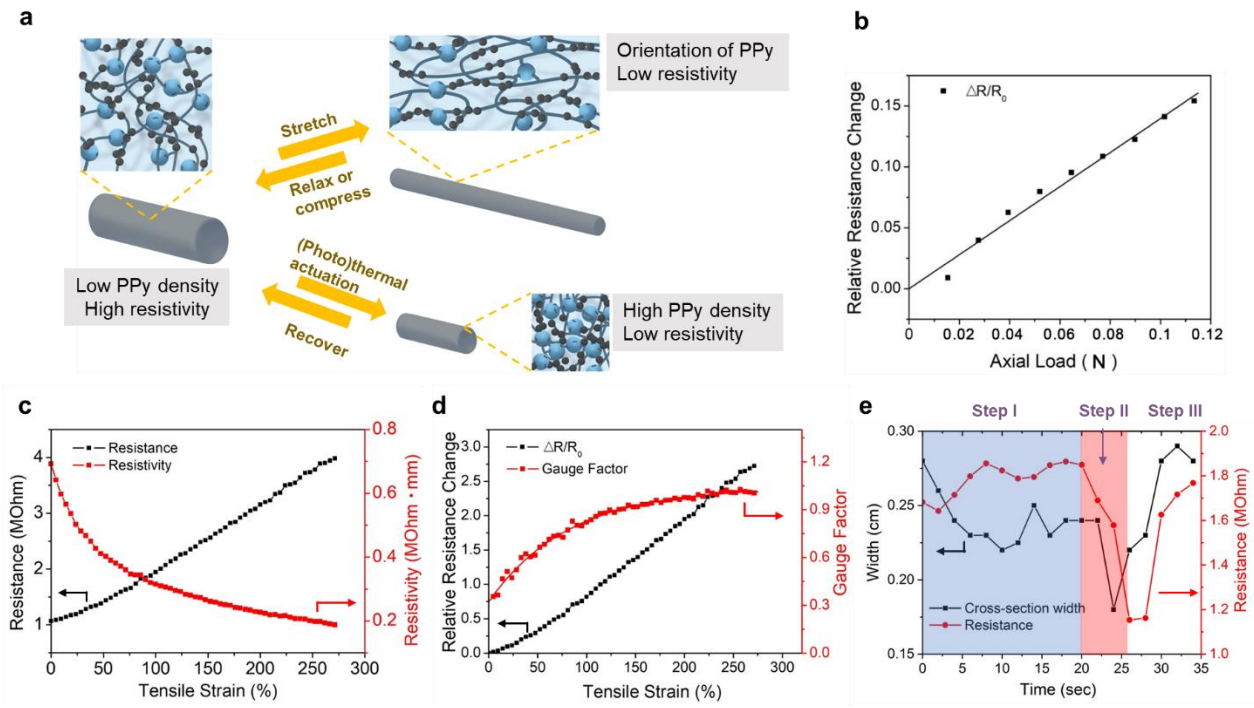

Figure 3 (a) Resistivity changes with stretching, compression, and (photo)thermal actuation due to change in alignment and apparent density of the conducting PPy network. (b) Resistance change as a function of axial load. at small compression deformation (axial stress <1 kPa), showing linear behavior. (c) Resistivity and resistance change as a function of tensile strain, showing that for large tensile stretch, resistivity decreases with strain. The mechanism can be described in (a). (d) Strain sensing performance of c-NanoH, demonstrating ultra-high strain sensing range (up to 280%) with decent sensitivity at high strain (G/F=1) (e) Resistance measurement on c-NanoH with fixed length. In the blue region, the resistance increases possibly due to the isolation during the PNIPAAm phase transition. In the red region, the resistance abruptly decreases due to the density change of the PPy network.

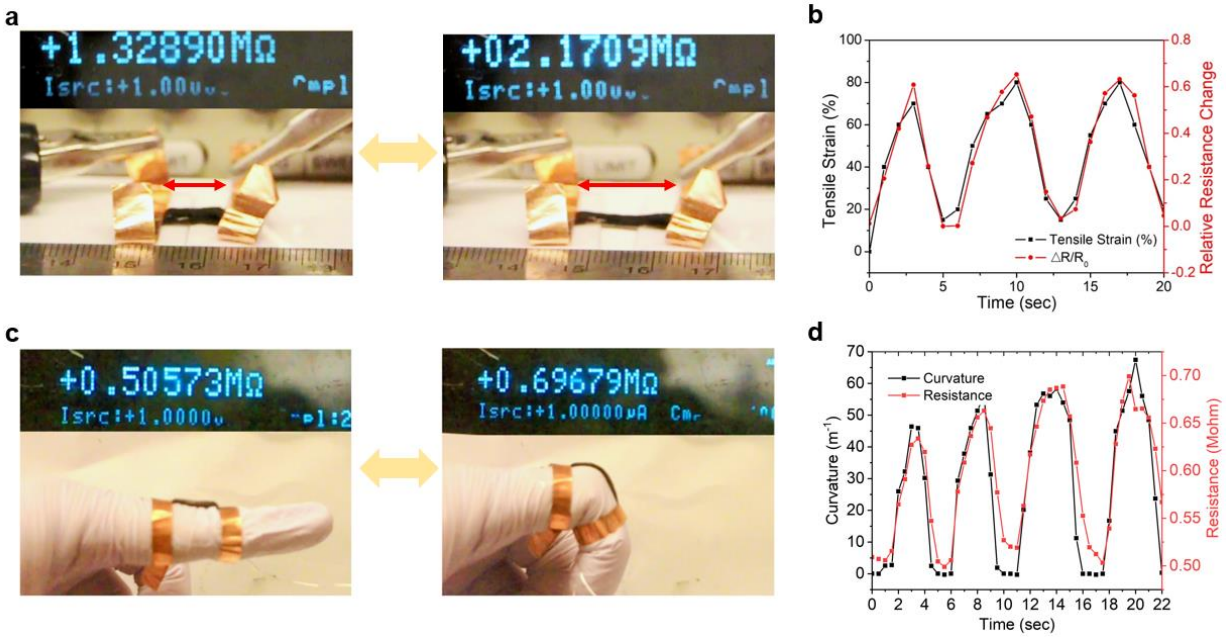

Figure 4. (a)(b) Demonstration of stable real-time cyclic stretch strain sensing, and (c)(d) real-time curvature sensing on a human forefinger.

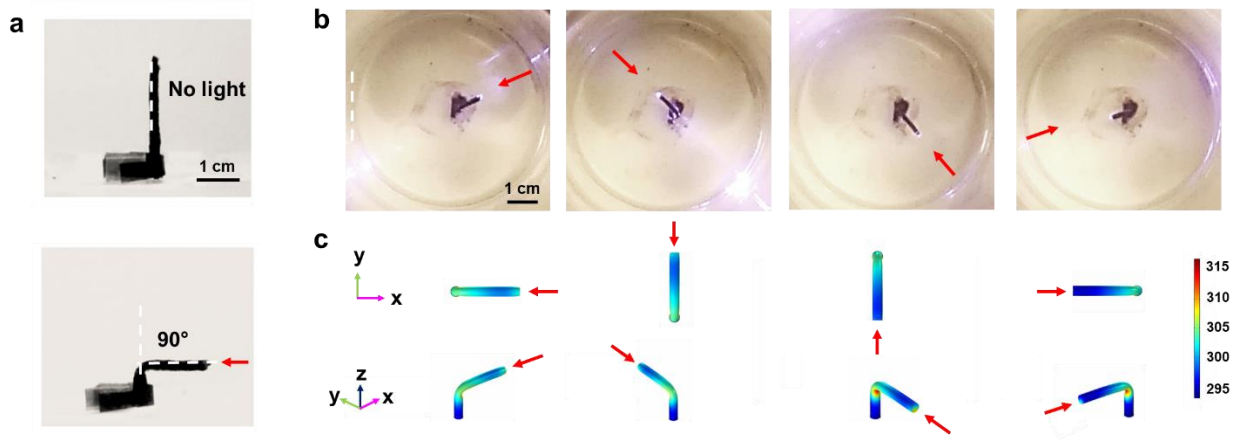

Figure 5. (a) Side view of a (top) c-NanoH pillar standing upright and (bottom) light-induced pillar bending to 90°. (b) Top view of omni-directional light tracking from 4 different directions, showing versatile actuation in response to the direction of light source. (c) Simulation results of shape deformation and temperature gradient on omni-directional tracking pillar. Light from four different azimuthal angles were applied on the pillar and the color indicates the temperature distribution. The unit of the color code is Kelvin.

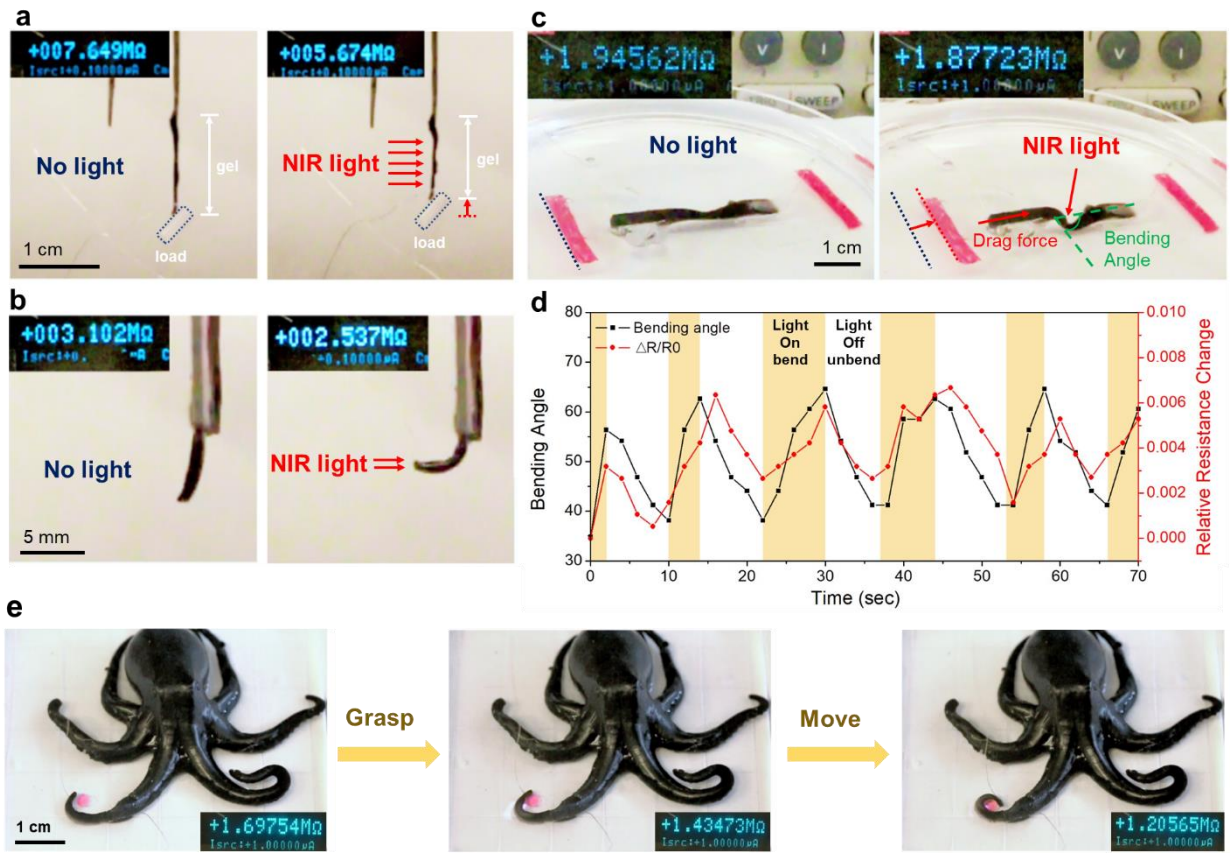

Figure 6. (a) Self-sensing weight-lifting in air. (b) Self-sensing "sit-ups" induced by light tracking in air. (c) Stable and completely reversible self-sensing robot in water. (d) The bending angle coincides with the resistance change in the reversible self-sensing robot in water. (e) Self-sensing grasping motion by NIR manipulated local stimulation.

Chapter 3. Somatosensory Actuator Based on Stretchable Conductive Photothermally-Responsive Hydrogel

Chapter 3 is reprinted with minor edition with permission from American Association for the Advancement of Science.

Authors

Yusen Zhao,[1,‡] Chiao-Yueh Lo,[1,‡] Lecheng Ruan[2], Chen-Huan Pi[2], Cheolgyu Kim[1], Yousif Alsaid[1], Imri Frenkel[1], Rossana Rico[2], Tsu-Chin Tsao[2], Ximin He[1,3*]

Affiliations

[1]Department of Material Science and Engineering, University of California Los Angeles, Los Angeles, CA, 90095 USA; [2] Department of Mechanical and Aerospace Engineering, University of California Los Angeles, Los Angeles, CA, 90095 USA; [3]Califonia Nanosystems Institute, Los Angeles, CA, 90095 USA

*Corresponding author. Email: ximinhe@ucla.edu

Abstract

Soft robots, advantageous in their compliance and flexibility, have advanced smart soft materials towards multifunctionality and local sensing capabilities that approach human dexterity. Mimicking biological neuromuscular systems' sensory motion requires the unification of sensing and actuation in a singular artificial-muscle material, which must not only actuate but also sense their own motions. Here, we report a soft somatosensitive actuating material utilizing an

electrically-conductive and photothermally-responsive hydrogel, which combines the functions of piezoresistive strain/pressure sensing and photo/thermal actuation into a single material. Synthesized through an unconventional ice-templated UV-cryo-polymerization technique, the homogenous tough conductive hydrogel exhibited a densified conducting network and highly porous microstructure, achieving a unique combination of ultra-high conductivity (36.8 mS/cm, 10^3-fold enhancement) and mechanical robustness, featuring high stretchability (170%), large volume shrinkage (49%), and 30-fold faster response than conventional hydrogels. With the unique compositional homogeneity of the monolithic material, the hydrogel solved the limitation of conventional physically-integrated sensory actuator systems with interface constraints and predefined functions. The 2-in-1 functional hydrogel demonstrated both exteroception to perceive the environment and proprioception to kinesthetically sense its deformations in real time, while actuating with near-infinite degrees of freedom. We have demonstrated a variety of light-driven locomotion including contraction, bending, shape recognition, object grasping and transporting with simultaneous self-monitoring. When connected to a control circuit, the muscle-like material achieved closed-loop feedback controlled, reversible step motion. This material design can also be applied to liquid crystal elastomers. This conceptual somatosensitive robotic material represents a step towards next-generation soft robots with life-like adaptiveness and higher-level autonomy.

Summary (125 characters): A somatosensitive actuatable material that molecularly integrates sensing and actuation in a monolith for perceptive closed-loop soft robots

Introduction

One of the unique capabilities that sets living organisms apart from man-made materials is the ability to perceive and manage their motion to adapt to their environment. This is enabled by locally sensing their movement (kinesthetic) and environment (tactile) by proprio-/extero-receptors to provide somatosensory feedback for effectors through the reflex arch or neuromuscular systems (1). For example, octopi exhibit a highly localized and continuous neural system with non-segmented arms that can accomplish various tasks, ranging from basic arm shortening/elongation to complex object grasping, shape morphing, and accessing restricted environment (2) (**Fig. 1A**). One of the ultimate goals for robotics is to demonstrate sensorimotor-like abilities, by mimicking the receptors and effectors in biological somatosensory systems to achieve simultaneous active motion and perception functions. This requires integrating sensors and actuators with conflict-free and matching sensitivity to the deformation range, without compromising the desirable high mechanical flexibility, fast actuation, and real-time sensation. As conventional rigid robots are powered by motors and sensed by motion encoders (3, 4), force load cells (5), or camera to provide feedback on terrain conditions and locomotive gaits, their complex and bulky multi-electronics integration would restrict their motility and miniaturization.

Soft robots, alternatively, which utilize more processable and conformable soft materials (6, 7), offer promising opportunities for sensing-actuation unification. Some somatosensory soft robots have been capable to not only monitor the roughness, softness, and temperature of objects, but also grasp the objects by using control algorithms (8-10). Current state-of-the-art soft sensors are based on optical fibers (9, 11, 12), electroluminescent dyes (6), triboelectricity (13), and piezoresistivity (6-8, 10, 14-18), while soft actuators are based on the asymmetric expansion (16,

19), pneumatic inflation (20), and hydraulic actuation (21). Defined by their specific working mechanisms, these sensors and actuators are all single-function units, still unable to realize sensation and actuation simultaneously. Therefore, add-on functionalities to soft robots have been employed to physically integrate the two individual components by welding (7), 3D printing (8), embedding (9) or laminating sensors and actuators (22). Fabricating such heterogeneous multi-material systems typically involve complex integrating processes with multiple molding and lamination steps and complicated connection terminals (8, 16). These physically-integrated systems with various material interfaces also have potential stress concentration and adhesion issues (1). In terms of robotic performance, the sensing and actuation functionalities are predefined with constrained flexibility when handling complex dynamic environment.

It would be highly advantageous to develop a multifunctional monolithic material containing chemically integrated sensing and actuation components at the molecular level, rather than the system level (1). Such a somatosensory actuatable material can ideally present intrinsic sensing capability and non-predefined actuation simultaneously, without potential delamination or sensing/actuation range mismatching associated with physically-integrated multiplexed design. In addition, the bulk material with molecularly modular design can be chemically customized and physically tuned for optimized mechanical and electrical properties, and further combined with other units for higher-level functionality. However, material designs that seek to accommodate such multifunctionality without a conflict between the signal transductions of the sensing and actuating processes remain limited (23). Designing complex energy transduction mechanisms in existing soft materials (e.g., conducting polymers) may realize multifunction (sensing and actuation); however, the resulting performance would be rather limited and unsatisfactory for the

demanding soft robotics applications (e.g., large, fast and forceful shape changing and high strain sensitivity simultaneously).

Among many active polymers, hydrogels are attractive artificial muscle materials for soft robotics, providing the potential for human-machine interfaces with their three-dimensional hydrophilic polymer networks, mechanical properties similar to biological tissues, and bio-compatibility. This class of stimuli-responsive materials can undergo a significant volumetric change in response to a variety of environmental stimuli (24-30), and thus may serve as a good actuator. To manifest the hydrogel's ability to sense, a piezoresistive mechanism is predominantly utilized, possibly based on ionic or electronic conduction. While ionically conductive materials require low-voltage alternating current (AC) operation due to ion migration, electronic conduction with direct current (DC) operation (31) has advantages with direct readouts to feed the control program for electronic interfaces and for under-water operation without ion leakage issues. Although flexible conductive polymers/hydrogels have been explored for soft electronics applications, these materials lack the stimuli-responsive actuation ability required for soft robotics applications(32). Therefore, to prove the concept, we propose that by molecularly combining a stimuli-responsive hydrogel with a conducting polymer (CP) (33-35) in a single material as an exemplary modal system, both actuation and sensing can be realized simultaneously. The hierarchical porous hydrogel network would allow for both continuous electronic conduction for sensation and efficient mass (water) transport for actuation (36). Although CP-percolated stimuli-responsive hydrogels have been reported (33), multiple obstacles still remain preventing them from serving as sensory actuators: **a)** CPs percolation using conventional two-step methods results in high inhomogeneity, typically with CPs formed only on the hydrogel skin (Fig. S2) (37, 38), and are hence unable to accurately reflect the actual material deformation. **b)** Challenges have been

found when making materials both electrically conductive and capable of withstanding large mechanical deformation (18, 39). Their conductivity and mechanical robustness are relatively low, due to the formation of nano-aggregation and discontinuities of the two polymer networks, leading to unstable sensing signals (34) and poor actuation and load bearing. **c)** The slow actuation due to the slow diffusion in hydrogels with non-continuous channels has a response time of minutes or hours (40). **d**) More importantly, although the state-of-the-art conductive hydrogels can reach either high conductivity, good mechanical properties, fast and substantial actuation, or sensing individually, realizing all the desired features simultaneously in one CP-percolated responsive hydrogel composite remains challenging.

Herein, we present a molecularly innervated CP-percolated hydrogel-based material acting as a soft somatosensitive actuator, capable of performing a variety of feedback-controlled robotic tasks, including octopus-arm-like shortening, elongation, object perceiving and grasping. This homogeneous bulk conductive hydrogel is comprised of an interpenetrating polymer double-network of poly(N-isopropylacrylamide) (PNIPAAm) and polyaniline (PAni), which combines both photo/thermal actuation and piezoresistive sensing into a monolithic material of '2-in-1' functionality. To achieve the high conductivity and high mechanical robustness necessary for simultaneous optimum strain sensitivity and deformability, we developed an unconventional one-pot synthesis method via the ice-templated, UV polymerization of PNIPAAm and cryopolymerization of PAni (ITUC). It successfully solved the aforementioned three issues with **i)** distributing the conductive (sensing) and the stimuli-responsive (actuating) components homogeneously distributed at a molecular level throughout the entire bulk material, **ii)** maintaining a continuous pathway for electron conduction and so high sensitivity, while remaining strong and stretchable (a result of the suppressed CP-nanoaggregate overgrowth under sub-zero reaction and

the densified CP packing by ice templating), and **iii)** possessing open pores for high water diffusion and thus fast actuation.

Such a material exhibited conductivity enhancements of three orders of magnitude and mechanical modulus enhancement of up to 386%, compared to the liquid-phase synthesized hydrogel. As an actuator, the hydrogel can rapidly change to any arbitrary shape and size in response to stimuli and does so with a significantly improved response rate (30-fold faster than conventional PNIPAAm) and a high volume-change ratio (shrinkable to 50% volumetrically). We have demonstrated tracking towards incident near-infrared (NIR) light precisely, presenting an autonomous signal-tracking ability with reflex-like, decentralized open-loop feedback, object lifting (20 times of its weight) and object grasping acting as a soft gripper. As a sensor, exhibiting unique pure ohmic electronic conduction under DC voltage, the hydrogel performed exteroception to detect the mechanical stretching ($GF = \Delta R/R_0/\varepsilon = 2.3$ at 170% stretch), bending, and compression. As this material has non-interfering sensing and actuation (referred as the e-output and photothermal-input), its actuation can be detected in real-time to provide sensory feedback, undisturbed by the photothermal activity in actuation. Thus, the sensory actuator also had proprioception to monitor its responsive elongation/shortening and bending/unbending under NIR light stimulation. As a proof of concept, it was demonstrated that the somatosensitive actuator had the potential to help recognize the shape of an unknown object based on the deformation time and resistance evolution. Furthermore, we developed a closed-loop algorithm for actively controlling the artificial arm elongation/shortening, which could be successfully maintained at targeted lengths precisely. The generality of the modular material design has been demonstrated by successfully realizing CP-percolated liquid crystal elastomer (LCE) material with sensory actuating abilities. Overall, with customizable composition and tunable properties, this class of molecularly

innervated somatosensitive active hydrogels successfully takes a step towards next-generation life-like soft robots with a self-diagnostic feedback-controlled autonomy a reality. Meanwhile, they may be readily applied to and augment current inflatable actuators, prosthetics, exoskeletons, wearable systems, smart textiles, and locomotive robots.

Results

To build a material capable of somatosensitive actuation, we sought out the rational combination of PAni conducting polymer and PNIPAAm hydrogel. In this homogeneous interpenetrating polymer network, PNIPAAm provides both thermo-responsive actuating capability and mechanical flexibility, while the black-colored conductive PAni simultaneously acts as both a photothermal transductor and a piezoresistive sensor. The resistance change upon material deformation results from the synergic deformation of the PAni network to alter the electrical pathway (41). When temperature increases beyond the lower critical solution temperature (LCST) of PNIPAAm, the resistivity of the hydrogel is significantly reduced as the PAni network becomes more compacted through the drastic, temperature-driven shrinkage of PNIPAAm (**Fig. 1A**) (33, 38).

Fabrication and properties

Traditionally, to obtain a CP-hydrogel composite, people used a two-step synthesis method. Due to the incompatibility of the two syntheses (42), hydrogel is formed and subsequently soaked in a CP prepolymer solution to in-situ polymerize the CP around existing hydrogel chains (37, 38, 43, 44). However, the sub-micron-sized pores of hydrogels hardly allow for sufficient penetration

of CP molecules into the entire hydrogel matrix, which results in a CP-rich shell and a non-conductive core, hindering its application in sensing and actuation (i.e., the ITU in-situ gel in **Fig. S2**). To solve the inhomogeneity issue, we designed a one-pot polymerization technique, whereby the PNIPAAm and PAni precursor mixture was first irradiated under UV light to polymerize PNIPAAm and then kept at room temperature overnight to polymerize PAni (**Fig. S1A**). The UV- and thermally-polymerized hydrogel, referred to as a **UT gel**, possesses uniformly distributed PAni throughout the PNIPAAm network (**Fig. S2, S3**). We measured the conductivity of the UT gels using the AC impedance method first, to minimize the potential electrical double layer (EDL) capacitance (35) due to possible dominant ionic conduction. The conductivities ranged from 0.034-0.06 mS/cm at 0.2~0.8 wt.% BIS crosslinking densities (**Fig. 1F**). Under direct current (DC), however, the resistance of the UT gel (1 cm × 2 cm × 0.1 cm) was still unstable over time and at the scale of 1 MΩ, which was close to that of pure water and was therefore unable to accurately reflect the material deformation if it were to serve as a strain sensor. Mechanically, the elastic moduli of the UT gels were 14~44 kPa from the tensile stretching tests (**Fig. 1E**). Despite the high loading of CP (0.8 M PAni with 20 wt.% of PNIPAAm), the resulting conductivity and mechanical properties were relatively low, compared to pure PAni hydrogels (conductivity=110 mS/cm) (35). This necessitated modification to further boost the conductivity to 10-100 mS/cm and the modulus to 0.1-1 MPa, to deliver high-performance sensing and powerful actuation. We speculate that the introduction of the non-conducting PNIPAAm and high-water content in the polymer matrix might have impeded the conductive pathway. Meanwhile, the liquid-phase polymerization gels suffered from uncontrollable reaction kinetics, leading to the formation of disconnected CP nano-aggregates, and so, lacked the desirable compact and interconnected packing needed to ensure continuous electron transport and mechanical strength (42).

To produce dense CP chain packing at micro/nano scale, we modified the UT synthesis by introducing ice-templating and cryopolymerization for PAni (**Fig. 1B**). Specifically, the mixed solution was rapidly frozen under liquid nitrogen (-196℃) to form an ice-template, followed by UV- and cryo-polymerization of PNIPAAm and PAni, respectively, in a sub-zero environment (-20℃). The as-prepared gel is referred to as **ITUC gel**. The modified ITUC gel was much more robust mechanically, capable of bending freely to 180^{o}, being stretched, and twisted to 180^{o} without causing any material damage (**Fig. 1D**). From the tensile tests, the ITUC gels with different crosslinking densities (BIS concentrations) showed a tunable tensile strength up to 0.18 MPa and a 250%-386% modulus enhancement over the UT gels (**Fig. 1E**). Meanwhile, the ITUC gel with 0.2 wt.% BIS presented decent deformability with up to 170% stretch at break, suggesting a broad strain sensing and actuation range. At the same time, the ITUC gels exhibited remarkably high conductivities of 24.6-36.8 mS/cm, which were >10^3 times higher than those of UT gels (**Fig. 1F, Fig. S4**). For more clearly identify the key factors that enabled the high conductivity, we have also made another two control samples by, respectively, UV-cryopolymerizing PNIPAAm followed by liquid-state polymerizing PAni from the PNIPAAm-PAni precursor mixture (denoted as ITUL gel), and UV-cryopolymerizing PNIPAAm followed by immersing in PAni precursor and in-situ polymerizing PAni in liquid state as well (denoted as ITU in-situ gel) (**Table S1, Fig. S2**). It showed that both the mechanical property and conductivity of the ITUC gel were significantly improved, compared to properties of UT, ITUL, ITU in-situ, and literatures using the two-step in-situ polymerization methods (**Fig. S5, 6**). The tremendous enhancement of conductivity can be attributed to the ice densification effect (45) and low-temperature reaction (46, 47) of PAni that allowed for substantially denser packing and effectively mitigated nano-aggregation of PAni, facilitating a continuous electronic pathway (as experimentally compared to ITUL gel with liquid-

state polymerization of PAni). The SEM images also clearly showed the more compact microstructure with more uniform pore sizes 0.5-2 μm, in contrast with 5-10 μm pores of UT gel (**Fig. S3**). Besides, the stability of the ITUC gel constantly soaking in water over time was studied, showing ~46% conductivity drop after a week (**Fig. S7**), which is presumably due to the loss of dopant (phytic acid here) under the long-term neutral pH condition (48). By incorporating PVA in the existing ITUC gel, an improved electronic stability has been achieved (~74% conductivity retention), presumably due to the strong hydrogen bonding of PVA to stabilize the dopant phytic acid (**Fig. S7**). Further stability improvement study will be conducted in future research.

Actuation performance

To examine the actuation capability of the ITUC hydrogels, we analyzed the hydrogel shrinkage at 40°Cand recovery rate at room temperature. The ITUC gel (thickness = 0.1 cm) shrunk up to 49.7% within one minute, with a diffusion time scale (duration of shrinkage to 1/e of its initial volume) of 8 seconds (**Figs. 2A, S8**). Notably, although the hydrogel network was toughened by an ice-induced polymer densification effect, the responsive actuation performance was not significantly compromised, compared to the UT gel (**Fig. S8**). Promisingly, the shrinking of the ITUC gel was 10-100 times faster than that of the conventional hydrogels on a scale of minutes (**Fig. S9**) to hours (33, 49). The significantly fast volume changes of our hydrogels arises from the bicontinuous microstructure with open pores, featuring a unique low tortuosity that facilitates rapid water diffusion in and out of the polymeric network (50), and thus swift actuation shown as follows.

The composite hydrogels can be actuated not only by heat, but also by light via the photo-thermal-mechanical mechanism due to the photothermal property of PAni. Under NIR light

irradiation, the ITUC gel could effectively shrink and lift a weight of up to 171.6 times of its dry polymer weight (**Fig. 2B, movie S1)**. The hydrogel strip with dimensions of 3.41 mm × 1.36 mm × 7.36 mm can produce a force of 0.055 N and strength of 10.7 kPa, which is 20-time higher compared to conventional PNIPAM hydrogels (51-55) (**Fig. S10**). Furthermore, as the composite hydrogels are chemically homogeneous without any composition gradient or interface like those in conventional physically-integrated systems, they allow for actuation in almost all directions with nearly infinite degrees of freedoms (DOFs). When a NIR light shined on the hydrogel strip at an arbitrary angle, the hydrogel bent towards the incoming light and precisely maintain tracking the light source via real-time autonomous reorientation (**Fig. 2C)**. The hydrogel could rapidly recover its original un-deformed configuration when the light was off (**Fig. 2D**). As depicted in our simulated graphs with our multi-physics model that coupled the photo-thermal-stress fields in **Fig. 2C** and **movie S2**, such a directional, asymmetric motion was attributed to the temperature gradient across the hydrogel (27), where the temperature on the illuminated side increased to above the LCST while the temperature on the shaded side still remained below the LCST, resulting in the local shrinking on the illuminated side and the overall bending of the gel. Once the bending strip reached the light's direction (in that it was parallel to the incident light), it steadily aimed at the incident light controlled by a built-in feedback loop arising from the dynamic light-material interaction. Such an autonomous signal tracking behavior demonstrated a decentralized, open-loop self-controlled actuation. Apart from the object tracking achieved by the temperature gradient, we also demonstrated that the ITUC gel can bend to a defined direction under elevated temperature through seamlessly adhering the gel with a passive layer in a bimorph assembly (**Fig. S11**). By assembling four hydrogel arms, we successfully fabricated a cross-shape soft gripper, which could

rapidly grasp an object in hot water (**Fig. 2E, movie S3**). This bimorph also showed that the materials can be facilely combined with other materials to construct a system for complex tasks.

Sensing performance

The ITUC hydrogel provides high conductivity with stretchability, capable of serving as a piezoresistive strain sensor under mechanical deformation. First, the ITUC gel showed a desirable 0^o phase angle at a broad AC frequency range, whereas the UT gel had a $>40^o$ phase angle at low frequency (**Fig. S12**). The high phase angle in the UT gel indicated more ionic conduction, leading to the electrochemical reaction at the electrode interface. Second, the ITUC gel showed a desirable <0.4% resistance change over 400 seconds at direct voltage, in high contrast to the >650,000% large change of the UT gel (**Fig. 3B**). Furthermore, the current-voltage (I-V) curve of the ITUC gel was an ideal symmetric straight line, while the UT gel showed a capacitive behavior with an enclosed area (**Fig. 3C**). All these together indicated that the conductivity of the ITUC hydrogel was dominated by ohmic electronic conduction with minor ion-derived conduction, which is highly desired for high sensing performance. This also showed the effectiveness of this new material synthesis method in solving the aforementioned issues of low electronic conductivity presented by UT gels and conventional conductive gels.

The ITUC gels with high stretchability and responsiveness enabled not only the exteroception to sense passive deformations (**Fig. 3D**), but also the proprioception to monitor its own motion internally in response to stimulation. For exteroception, we first carried out the strain sensing under uniaxial stretching (**Fig. 3D**). The gauge factor ($GF = \Delta R/R_0/\varepsilon$, $\Delta R = R-R_0$), which

is the relative resistance change to strain ratio, reached 2.3 at 70% tensile strain (**Fig. 3D**). The sensitivity is comparably higher than PEDOT/PVA and graphene/PAAm gel sensors at the corresponding tensile strain (34, 56). The improved sensitivity can be attributed to the uniform continuous CPs network without agglomerates by ice-templated low-temperature polymerization. During the passive deformation, the less aggregated microstructure can conformably reflect the macroscopic stretching of the gel, resulting in higher mechanical robustness and sensory capability (34, 56). Apart from the stretching mode, the hydrogel could also detect the bending and compression, which showed its potential as curvature sensors and haptic (tactile) sensors (**Figs. 3E** and **3F, Figs. S13** and **S14**). Regarding the similar mechanical properties to biological tissues and compatibility of hydrogels, the ITUC gel can be used for human motion monitoring. The ITUC gel mounted on a human finger could precisely sense the motion of human finger during the bending and recovery at different angles reversibly (**Fig. S15**).

Somatosensitive actuation

Proprioception was further demonstrated through real-time monitoring of its own active actuation behaviors, which mimicked the self-sensing of physical states and motions in living organisms, such as the self-monitored extension or curling of octopus arms. We first demonstrated the kinesthetic shortening/elongation of a hanging ITUC gel by placing a load at the bottom (**Fig. 4A, movie S4**). Upon illumination by NIR light, the gel strip shortened. The resistance interestingly increased slightly within the first few seconds and then decreased continuously (**Fig. 4B**). We assume the initial relative resistance change ($\triangle R/R_0$) spike was ascribed to the rapid microstructural change of PNIPAAm network into clusters that partially isolated the individual PAni chains (33). The disconnected clusters resulted in the instant resistance increase of the gel.

However, the further shrinkage of the entire dynamic polymer network well enabled the reconnection of the clusters back to the continuous electron pathway, leading to a continuous resistance decrease. Reversely, as the light was switched off, the resistance was initially reduced over the lower limit, followed by a gradual recovery to the initial state. Besides, we find the design principle to be sufficiently broad for other materials system, such as liquid crystalline elastomers percolated by conducting polymers. The composites performed similar proprioceptive actuation but much higher generated force due to its non-water nature (**Fig. S16**).

Similarly, real-time monitoring of photo-responsive bending/unbending actuation was also successfully demonstrated when not mounting a load to the hanging gel (**Fig. 4C, movie S5**). Similar light-regulated motion as shown in **Fig. 2C** was successfully monitored in real-time by the gel itself. We noticed slight over-bending during its shape recovery upon light shutoff, presumably due to the overheating of the front surface without the restriction of the built-in feedback lock (26, 27). A similar spike in the resistance change was observed within the first few seconds of turning the light on and off caused by the rapid polymer network change (**Fig. 4D)**.

To fully demonstrate the utility of the somatosensory feedback in a soft robotic system, we assembled the ITUC gel into an octopus as a soft proprioceptive arm (**Fig. 4E, movie S6)**. Starting with a straight inactive state, the octopus arm bent up upon NIR illumination and wrapped around a series of cylinders rods of different sizes. The recorded resistance profiles represent the processes of perceiving and grasping the three objects of different diameters respectively (5, 10, and 15 mm, **Fig. 4F**). Specifically, a 7% resistance drop occurred when the arm fully wrapped around the 5 mm cylinder, while a 0.8% resistance reduction occurred over a relatively shorter period of time when perceiving and grasping the 15 mm cylinder, reflecting the relatively smaller required

bending deformation (**Fig. 4G**). Therefore, both the magnitude and time of resistance change during grasping provide the potential for the shape recognition of unknown objects by the proprioceptive grasping strategy.

Closed-loop actuation

As an ultimate display of the gel's unification of sensory and actuating functions, we developed a closed-loop control system to mimic a biological neuromuscular system, which involves a nerve impulse passing inward from a receptor to the spinal cord and then outward to an effector, much like a muscle or gland triggering an impulsive approach towards or retraction from an external object or environmental stimulus. Control algorithms were designed to precisely regulate the elongation/shortening deformation of a weight-loaded ITUC gel arm, by feeding the controller with the somatosensory feedback pertaining to the real-time length change and controlling the arm shrinking/relaxation motion accordingly (**Fig. 5A, movie S7**). Specifically, we mounted a gain-scheduled bang-bang controller to collect the resistance feedback and correspondingly manipulate the NIR intensity, which successfully held the arm length at three stepwise levels consistently with a 0.16 mm precision ($\Delta L/L_0$= 2.59±0.66%, 5.00±0.63% and 6.75±0.60%, L_0 = 25.0 mm) by controlling relative resistance change ($\Delta R/R_0$ =2.5%, 5.0%, and 7.5%) for two stable cycles (**Fig. 5B**). As shown in **Fig. 5C** and **5D**, both the strip resistance and strain oscillated around the target values in response to the light intensity modulating. A slight delay in deformation strain change was observed before reaching the equilibrium of the target length when the relative resistance change ramped down (i.e., gel shrinkage going small, during

the 870~1400 second period), while such a delay did not exist during target length ramp-up, attributed to the relatively faster gel shrinkage over its recovery.

The aforementioned abnormal resistance spikes upon strong illumination (**Fig. 4B**), also observed during the controlled arm elongation steps (**Fig. S17**), were well suppressed by lowering the light intensity as shown in **Figs. 5C** and **5D**. Meanwhile, the oscillation was suppressed as well with the effective fine tuning of light, as the rapid shrinkage of PNIPAAm network occurred mildly. It was found that a background non-zero weak illumination significantly increased the response rate and made the resistance responses to the gel shrinking and relaxation more symmetric, which could be attributed to the higher temperature baseline of the sample from continuous illumination. As the sample kept warm at a temperature close to its LCST, a smaller temperature change and shorter time were required to trigger sample deformation. Consequently, such a smaller light intensity difference upon switching also led to smaller oscillation along the target resistance and deformation.

In summary, we have demonstrated the potential of ITUC for closed-loop controlled, self-sensing underwater soft-robotics with stable and stepwise length control with a simple bang-bang controller. Based on this proof of concept, the remaining challenges in the calibration curve stability and oscillation amplitude will be addressed through further understanding and optimizing the ITUC hydrogel's stimuli-responsive kinetics and material decay, evaluation of resistance-temperature dependence, and employing more delicate control methods such as adaptive control for better performance and more complex robotic tasks.

Discussion

In this work, we successfully demonstrated a proof of the concept for implementing molecularly innervated somatosensitive robotic materials, based on conducting hydrogel composites comprised of conductive and responsive polymer networks produced by a one-pot synthesis. Realizing such an integration of both sensing and actuation functions in a single monolithic material was enabled by the unconventional ice-templated cryopolymerization strategy, which effectively resolved the long-lasting conducting polymer hydrogel challenges in inhomogeneity, aggregation formation, and the resulting low conductivity and poor sensory performance under DC voltage. This material preparation method is highly universal, capable of coupling broad choices of sensing and actuating functional components into a variety of smart materials. This hybrid material design can not only retain the functionalities from each component, but also synergistically achieve high mechanical and electrical properties required for sensory actuation. Compared to conventional multi-material integrated systems, the somatosensitive actuating material allows for arbitrary sensing location, offers self-contained multiple sensing nodes, and can be custom-designed for broad applications, including the demonstrated basic robotic tasks of contraction, bending, object lifting, and object grasping with open-loop and closed-loop control algorithms. The method can be also used to fabricate miniature robot with multisensory perception and mobility, which has proved to be a considerable challenge in most current soft robots (57).

Although promising, the presented exemplary hydrogel system still has several aspects to be optimized in future investigation: 1) the diffusion-governed response of hydrogel still limits the actuation rate, which can be further improved by morphological or chemical modification, or utilization of other operation mechanism; 2) in general, the deliverable force of hydrogels is relatively low due to the inherent porous network of high water content, which can be addressed

possibly by adding toughening agents; 3) obtaining high electrical conduction without compromising high stretchability, achieving high reliability of conduction over time, and stability of piezoresistive sensing mechanism under cyclic operation need to be considered for broader and practical soft robotics applications. With these goals to be achieved, the exemplary hydrogel-based somatosensory actuatable materials ultimately may be anticipated to perform remote under-water tasks for marine environment applications, such as sensing of roughness of an object, controllable gripping soft animals like mollusks, bypassing an obstacle, and going through a constrained channel. Beyond this exemplary system, this customizable modular material design can be also extended to other material systems such as liquid crystal elastomers to open up new opportunities.

From the perspective of the correlation between complexity and functionality of materials systems, we believe such materials with intrinsic somatosensitive actuating capabilities may open opportunities for intelligent materials with self-regulating functions and computing ability. With further development, this multifunctional material may lead to the next-generation life-like soft robots with unprecedented autonomy and performance in challenging tasks.

Materials and Methods

Materials preparation

500 mg NIPAAm, 5, 10, 15, or 20 mg BIS (0.2, 0.4, 0.6, or 0.8 wt%), 183 μL of purified aniline, 100 μL Darocur 1173, and a certain amount of DMSO were mixed into 2 mL solution, denoted as Solution A. Then, 365 mg APS was dissolved in 1 mL water solution. The two solutions were rapidly mixed with the volume ratio of A:B = 4:1 and cast in a mold in contact with liquid

nitrogen for freezing. Then, the frozen sample was illuminated under UV light while kept on a -20℃ cooling stage. Subsequently, the sample was kept in a -20℃ fridge for overnight. Finally, the sample was taken out to melt, and immersed in deionized water to remove excess reactant and salt.

General characterizations

Scanning electron microscopy (SEM) micrographs were taken by Zeiss Supra 40VP SEM. The mechanical properties of hydrogels, including the stress-strain behaviors, were investigated by a dynamic mechanical analyzer (DMA, TA Instruments, Q800). The conductivity was measured by attaching two parallel carbon cloth wires as electrodes on the hydrogel film. The AC impedance mode with the frequency sweep from 1-100000 Hz was conducted. The conductivity was calculated according to the formula: $\sigma=L/Rwt$, where w and t were the width and thickness of the sample, L was the distance of two carbon cloth, R was the resistance at 0^o phase angle. More than three samples were tested for one experiment.

Actuation and sensing characterization

The swelling and deswelling test were conducted by placing a round-shape hydrogel in the hot and cold water. The soft gripper was fabricated by growing a chemically crosslinked PVA film on the as-prepared ITUC gel as a passive layer. The exteroceptive sensing tests were carried out by connecting the hydrogel into an electrochemical workstation CHI660E. Strain sensing experiments were carried out by mounting the hydrogel on a stretching machine (Univert, CellScale) while connecting the two ends into a circuit. For proprioceptive contraction, bending,

and shape recognition, we attached the ITUC gel and electrodes with a clip or the as-mentioned PVA glue.

Closed-loop control of somatosensory actuation

The strain of the hydrogel strip-based artificial arm was measured by its resistance change during the light-triggered shortening and elongation, while being cross-monitored by a digital camera and analyzed with a tracker tool (Open Source Physics Java framework). The standard bang-bang controller algorism was written with Python. The arm length regulation logic is described as below: When the resistance was higher than the target resistance, a stronger light illumination was applied, resulting in arm shortening and thus a drop in resistance. When the resistance was lower than the target resistance, a weaker light illumination was applied, resulting in arm elongation and thus a rise in resistance. The regulation process includes three (A, B, and C) different resistance targets corresponding to the three targeted arm lengths, which are ordered in a stepwise ABCBA manner to demonstrate the ability of reversible arm shortening-elongation regulation.

SUPPLEMENTARY MATERIALS

The file includes:

Materials, synthesis, characterizations, and closed-loop control

Simulation

Movie Description

Other Supplementary Material for this manuscript includes the following:

Movie S1. Object lifting under NIR light

Movie S2. Phototropic behavior with computer simulation

Movie S3. Object grasping in hot water

Movie S4. Proprioceptive shortening and elongation

Movie S5. Proprioceptive bending and unbending

Movie S6. Object shape recognition by proprioceptive grasping

Movie S7. Closed-loop deformation control demonstration

References and Notes

1. H. Wang, M. Totaro, L. Beccai, Toward perceptive soft robots: Progress and challenges. Advanced Science **5**, 1800541 (2018).

2. B. Hochner, An embodied view of octopus neurobiology. Current biology **22**, R887-R892 (2012).

3. T. Mouri, H. Kawasaki, K. Yoshikawa, J. Takai, S. Ito, Anthropomorphic robot hand: Gifu hand III. in Proceedings of the 2002 International Conference on Control, Automation and Systems (ICCAS 2002) 1288-1293 (2002).

4. M. C. Carrozza et al., Design of a cybernetic hand for perception and action. Biological cybernetics **95**, 629 (2006).

5. M. G. Catalano et al., Adaptive synergies for the design and control of the Pisa/IIT SoftHand. The International Journal of Robotics Research **33**, 768-782 (2014).

6. C. Larson et al., Highly stretchable electroluminescent skin for optical signaling and tactile sensing. science **351**, 1071-1074 (2016).

7. F. Spina, A. Pouryazdan, J. C. Costa, L. P. Cuspinera, N. Münzenrieder, Directly 3D-printed monolithic soft robotic gripper with liquid metal microchannels for tactile sensing. Flexible Printed Electronics **4**, 035001 (2019).

8. R. L. Truby et al., Soft somatosensitive actuators via embedded 3D printing. Advanced Materials **30**, 1706383 (2018).

9. H. Zhao, K. O'Brien, S. Li, R. Shepherd, Optoelectronically innervated soft prosthetic hand via stretchable optical waveguides. Science Robotics **1**, eaai7529 (2016).

10. R. L. Truby, R. K. Katzschmann, J. A. Lewis, D. Rus, in 2019 2nd IEEE International Conference on Soft Robotics (RoboSoft). (IEEE, 2019), pp. 322-329.

11. C. To, T. L. Hellebrekers, Y. L. Park, Ieee, in IEEE/RSJ International Conference on Intelligent Robots and Systems (IROS). (Hamburg, GERMANY, 2015), pp. 5898-5903.

12. H. Zhao et al., A helping hand: Soft orthosis with integrated optical strain sensors and EMG control. IEEE Robotics Automation Magazine **23**, 55-64 (2016).

13. X. Yuan, J. Zou, L. Sun, H. Liu, G. Jin, in Proceedings of the 2019 International Conference on Robotics, Intelligent Control and Artificial Intelligence. (2019), pp. 690-695.

14. X. Fang et al., in 2019 2nd IEEE International Conference on Soft Robotics (RoboSoft). (IEEE, 2019), pp. 25-30.

15. K. Elgeneidy, N. Lohse, M. Jackson, Bending angle prediction and control of soft pneumatic actuators with embedded flex sensors–a data-driven approach. Mechatronics **50**, 234-247 (2018).

16. M. Amjadi, M. Sitti, Self-Sensing Paper Actuators Based on Graphite–Carbon Nanotube Hybrid Films. Advanced Science **5**, 1800239 (2018).

17. S. Wei et al., Preparation of soft somatosensory-detecting materials via selective laser sintering. J Journal of Materials Chemistry C **7**, 6786-6794 (2019).

18. M. D. Dickey, Stretchable and soft electronics using liquid metals. Advanced Materials **29**, 1606425 (2017).

19. H. H. Cheng et al., One Single Graphene Oxide Film for Responsive Actuation. Acs Nano **10**, 9529-9535 (2016).

20. D. Yang et al., Buckling pneumatic linear actuators inspired by muscle. Advanced Materials Technologies **1**, 1600055 (2016).

21. H. Yuk et al., Hydraulic hydrogel actuators and robots optically and sonically camouflaged in water. Nature communications **8**, 14230 (2017).

22. H. A. Sonar, A. P. Gerratt, S. P. Lacour, J. Paik, Closed-loop haptic feedback control using a self-sensing soft pneumatic actuator skin. Soft Robotics **7**, 22-29 (2020).

23. K. Kruusamäe, A. Punning, A. Aabloo, K. Asaka, in Actuators. (Multidisciplinary Digital Publishing Institute, 2015), vol. 4, pp. 17-38.

24. L. Chen et al., Thermal-responsive hydrogel surface: tunable wettability and adhesion to oil at the water/solid interface. Soft Matter **6**, 2708-2712 (2010).

25. X. B. Zhang et al., Optically- and Thermally-Responsive Programmable Materials Based on Carbon Nanotube-Hydrogel Polymer Composites. Nano Letters **11**, 3239-3244 (2011).

26. Y. Zhao et al., Soft phototactic swimmer based on self-sustained hydrogel oscillator. Science Robotics **4**, eaax7112 (2019).

27. X. Qian et al., Artificial phototropism for omnidirectional tracking and harvesting of light. Nature Nanotechnology, 1-8 (2019).

28. D. Schmaljohann, Thermo- and pH-responsive polymers in drug delivery. Advanced Drug Delivery Reviews **58**, 1655-1670 (2006).

29. S. K. De et al., Equilibrium swelling and kinetics of pH-responsive hydrogels: Models, experiments, and simulations. Journal of Microelectromechanical Systems **11**, 544-555 (2002).

30. A. Matsumoto, R. Yoshida, K. Kataoka, Glucose-responsive polymer gel bearing phenylborate derivative as a glucose-sensing moiety operating at the physiological pH. Biomacromolecules **5**, 1038-1045 (2004).

31. G. Cai et al., Extremely stretchable strain sensors based on conductive self-healing dynamic cross-links hydrogels for human-motion detection. Advanced Science **4**, 1600190 (2017).

32. Y. Zhao et al., Hierarchically Structured Stretchable Conductive Hydrogels for High-Performance Wearable Strain Sensors and Supercapacitors. Matter **3**, 1196-1210 (2020).

33. Y. Shi, C. Ma, L. Peng, G. Yu, Conductive "smart" hybrid hydrogels with PNIPAM and nanostructured conductive polymers. Advanced Functional Materials **25**, 1219-1225 (2015).

34. Y. Y. Lee et al., A strain-insensitive stretchable electronic conductor: PEDOT: PSS/acrylamide organogels. Advanced materials **28**, 1636-1643 (2016).

35. L. Pan et al., Hierarchical nanostructured conducting polymer hydrogel with high electrochemical activity. Proceedings of the National Academy of Sciences **109**, 9287-9292 (2012).

36. Y. Shi, L. Peng, Y. Ding, Y. Zhao, G. Yu, Nanostructured conductive polymers for advanced energy storage. Chemical Society Reviews **44**, 6684-6696 (2015).

37. K. Wang et al., Chemically Crosslinked Hydrogel Film Leads to Integrated Flexible Supercapacitors with Superior Performance. Advanced Material **27**, 7451-7457 (2015).

38. H. Kim, K. Kim, S. J. Lee, Nature-inspired thermo-responsive multifunctional membrane adaptively hybridized with PNIPAm and PPy. NPG Asia Materials **9**, e445-e445 (2017).

39. A. Chortos, J. Liu, Z. Bao, Pursuing prosthetic electronic skin. Nature materials **15**, 937-950 (2016).

40. M. C. Koetting, J. T. Peters, S. D. Steichen, N. A. Peppas, Stimulus-responsive hydrogels: Theory, modern advances, and applications. Materials Science and Engineering: R: Reports **93**, 1-49 (2015).

41. J. Teixeira, L. Horta-Romarís, M.-J. Abad, P. Costa, S. Lanceros-Méndez, Piezoresistive response of extruded polyaniline/(styrene-butadiene-styrene) polymer blends for force and deformation sensors. Materials Design **141**, 1-8 (2018).

42. C. Hu et al., Stable, strain-sensitive conductive hydrogel with antifreezing capability, remoldability, and reusability. ACS applied materials interfaces **10**, 44000-44010 (2018).

43. Y. Guo, K. Zheng, P. Wan, A Flexible Stretchable Hydrogel Electrolyte for Healable All-in-One Configured Supercapacitors. Small **14**, 1704497 (2018).

44. K. Sun et al., A Single Robust Hydrogel Film Based Integrated Flexible Supercapacitor. ACS Sustainable Chemistry & Engineering **7**, 165-173 (2018).

45. J. Lu, H. Wang, Z. Tian, Y. Hou, H. Lu, Cryopolymerization of 1, 2-Dithiolanes for the Facile and Reversible Grafting-from Synthesis of Protein–Polydisulfide Conjugates. Journal of the American Chemical Society **142**, 1717-1221 (2020).

46. P. C. Maity, M. Khandelwal, Synthesis time and temperature effect on polyaniline morphology and conductivity. American Journal of Materials Synthesis & Processing **1**, 37 (2016).

47. P. Adams, P. Laughlin, A. Monkman, A. Kenwright, Low temperature synthesis of high molecular weight polyaniline. Polymer **37**, 3411-3417 (1996).

48. D. Mawad et al., A conducting polymer with enhanced electronic stability applied in cardiac models. Science advances **2**, e1601007 (2016).

49. T. Gan, Y. Guan, Y. Zhang, Thermogelable PNIPAM microgel dispersion as 3D cell scaffold: effect of syneresis. Journal of Materials Chemistry **20**, 5937-5944 (2010).

50. H. Bai, A. Polini, B. Delattre, A. P. Tomsia, Thermoresponsive composite hydrogels with aligned macroporous structure by ice-templated assembly. Chemistry of Materials **25**, 4551-4556 (2013).

51. Y. S. Kim et al., Thermoresponsive actuation enabled by permittivity switching in an electrostatically anisotropic hydrogel. Nature materials **14**, 1002 (2015).

52. Y. Takashima et al., Expansion–contraction of photoresponsive artificial muscle regulated by host–guest interactions. Nature communications **3**, 1-8 (2012).

53. E. Palleau, D. Morales, M. D. Dickey, O. D. Velev, Reversible patterning and actuation of hydrogels by electrically assisted ionoprinting. Nature communications **4**, 1-7 (2013).

54. L.-W. Xia et al., Nano-structured smart hydrogels with rapid response and high elasticity. Nature Communications **4**, (2013).

55. C. Cvetkovic et al., Three-dimensionally printed biological machines powered by skeletal muscle. Proceedings of the National Academy of Sciences **111**, 10125-10130 (2014).

56. H. Zhang, W. Niu, S. Zhang, Extremely stretchable, stable, and durable strain sensors based on double-network organogels. ACS applied materials interfaces **10**, 32640-32648 (2018).

57. J. Hughes et al., Soft manipulators and grippers: a review. Frontiers in Robotics AI **3**, 69 (2016).

58. R. E. Rivero, M. A. Molina, C. R. Rivarola, C. A. Barbero, Pressure and microwave sensors/actuators based on smart hydrogel/conductive polymer nanocomposite. Sensors Actuators B: Chemical **190**, 270-278 (2014).

59. Z. Deng, Y. Guo, P. X. Ma, B. Guo, Rapid thermal responsive conductive hybrid cryogels with shape memory properties, photothermal properties and pressure dependent conductivity. Journal of colloid and interface science **526**, 281-294 (2018).

60. Y. Zhu, S. Liu, X. Shi, D. Han, F. Liang, A thermally responsive host–guest conductive hydrogel with self-healing properties. Materials Chemistry Frontiers **2**, 2212-2219 (2018).

61. W. Hong, X. Zhao, J. Zhou, Z. Suo, A theory of coupled diffusion and large deformation in polymeric gels. Journal of the Mechanics and Physics of Solids **56**, 1779-1793 (2008).

62. W. Hong, Z. Liu, Z. Suo, Inhomogeneous swelling of a gel in equilibrium with a solvent and mechanical load. International Journal of Solids and Structures **46**, 3282-3289 (2009).

63. P. J. Flory, J. Rehner Jr, Statistical mechanics of cross-linked polymer networks I. Rubberlike elasticity. The journal of chemical physics **11**, 512-520 (1943).

64. J. Zhang, X. Zhao, Z. Suo, H. Jiang, A finite element method for transient analysis of concurrent large deformation and mass transport in gels. Journal of Applied Physics **105**, 093522 (2009).

65. Z. Duan, J. Zhang, Y. An, H. Jiang, Simulation of the transient behavior of gels based on an analogy between diffusion and heat transfer. Journal of Applied Mechanics **80**, (2013).

66. R. P. Feynman, R. B. Leighton, M. Sands, The feynman lectures on physics; vol. i. American Journal of Physics **33**, 750-752 (1965).

Acknowledgments

Funding: The research was supported by the ONR Award N000141712117, the ONR Award N00014-18-1-2314, the AFOSR Grant FA9550-17-1-0311, and the AFOSR award FA9550-18-1-0449.

Author contributions: X.H. conceived the concept, planned the project and supervised the research. X.H., Y.Z. and C.L. designed and conducted the experiments and data analysis. Y.Z., C.L. and Y.A. conducted the fabrication and characterization. C. P. and L.R. developed the closed-loop control system under supervision of T.T. C.K. conducted the multiphysics modeling. Y.Z., L.R. X.H., C.L., Y.A., and T.T. wrote the manuscript. All authors have given approval to the final version of the manuscript. ‡These authors contributed equally.

Author Information: Reprints and permissions information is available at (website link). The authors declare no competing financial interests. Correspondence and requests for materials should be addressed to X.H. (e-mail: ximinhe@ucla.edu).

Competing interests: The authors declare that there is no competing interest.

Data and materials availability: All data needed to evaluate and support the conclusions in the manuscript are included in the main text or the Supplementary Materials. Contact Y.Z. and C.L. for any questions.

Figures and Tables

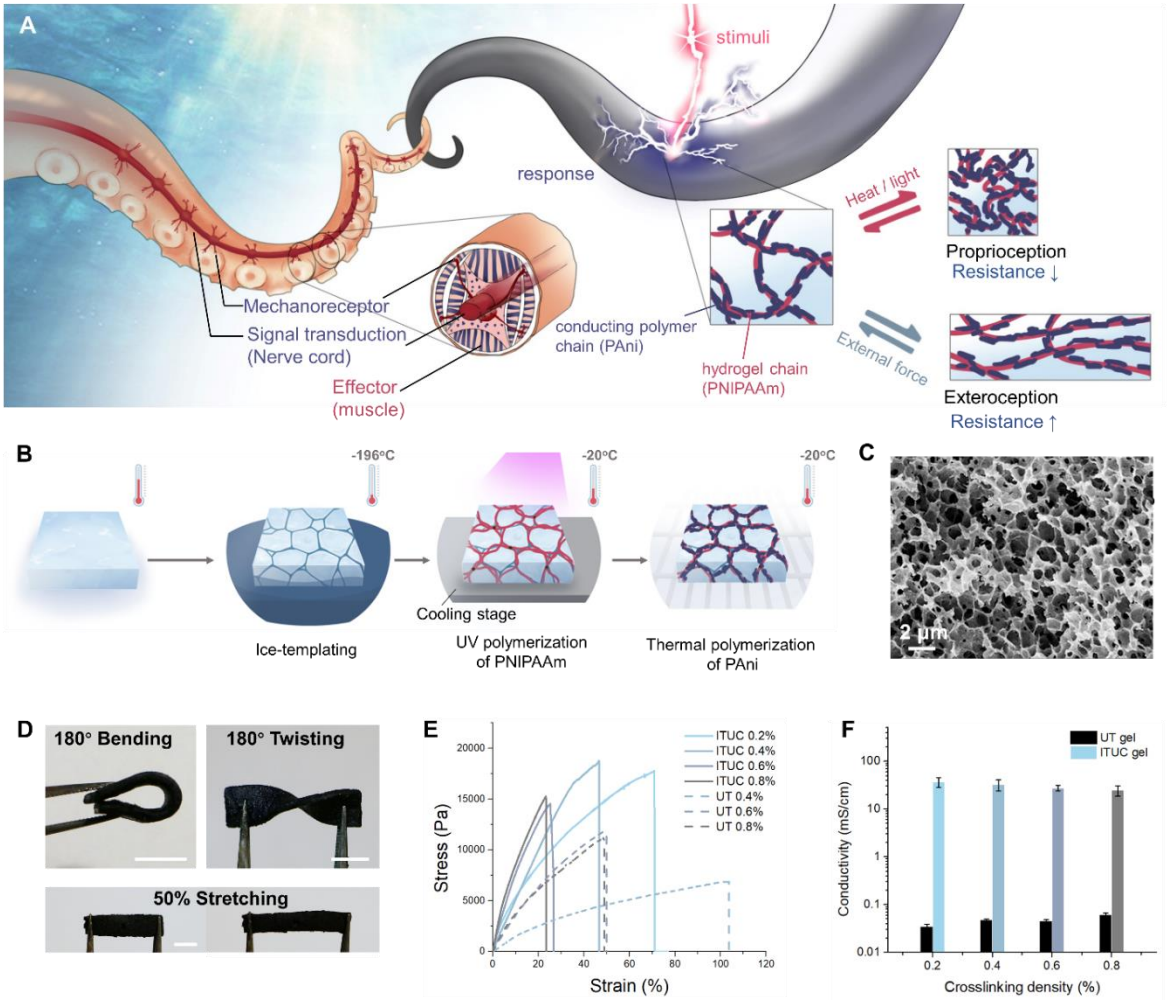

Fig. 1. Design of the somatosensitive actuator based on conducting polymer hydrogel. (**A**) Schematic of the bioinspired self-sensing actuator: Resistance change arose from density change or chain elongation of conducting polymer network when exposed to thermal stimulated volumetric change or external stress. (**B**) Fabrication of ITUC gel using the ice-templating, UV polymerization and cryopolymerization process. (**C**) SEM image of the ITUC gel. (**D**) Images of ITUC gel during bending, twisting and stretching. (**E**) Strain-stress curve of the ITUC gel and UT gel (control sample, without ice-templating) with difference crosslinking densities. (**F**) Conductivities of the ITUC gels and UT gels.

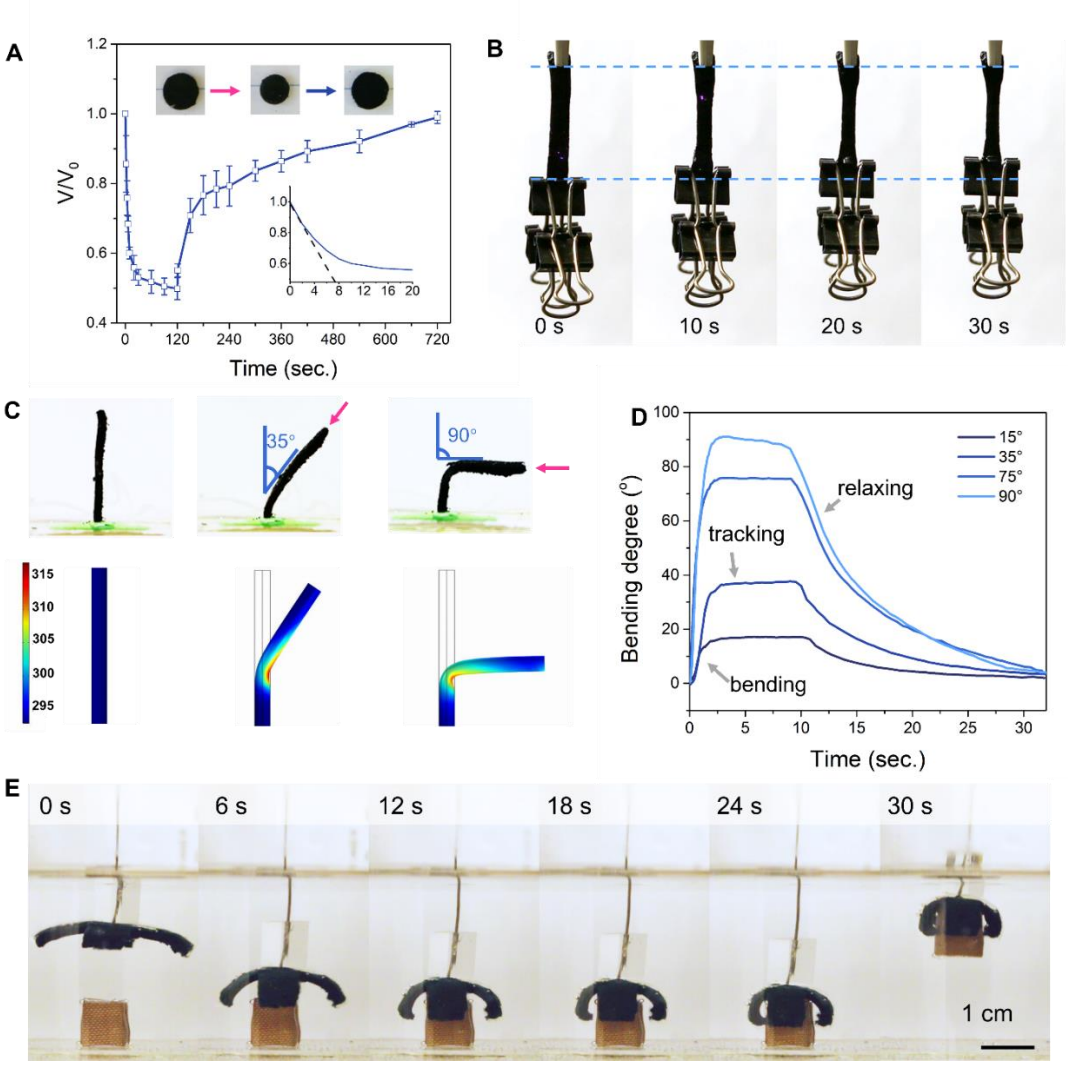

Fig. 2. Actuation performance under thermal or light stimulation. (**A**) Thermal-stimulated volume shrinkage (at 40℃) and recovery (at room temperature) in water. (**B**) Load lifting of ITUC gel under NIR illumination in air. (**C**) Phototropic behavior of ITUC gel that automatically track the light when exposed to a NIR light and the corresponding computer simulation results based on multiphysics model that captured both the bending angle and kinetics. (**D**) The angular evolution of hydrogel tracking to different oblique angles. (**E**) Sequential snapshots of the object grasping using the ITUC gel with a PVA passive layer in 45℃ hot water.

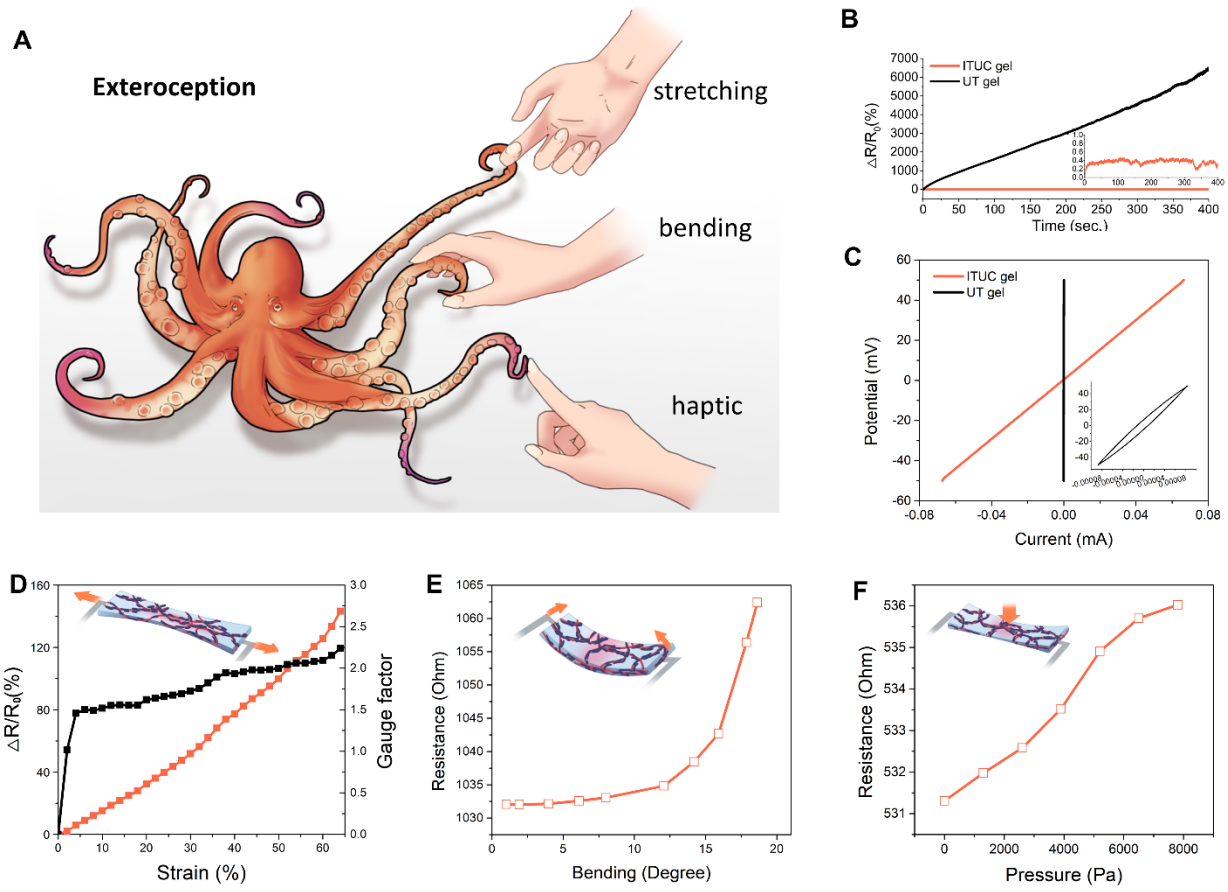

Fig. 3. Exteroceptive sensing of hydrogel. (**A**) Schematic of exteroceptive sensing. (**B**) The resistance of ITUC gel and UT gel over time. The inset shows the zoom-in resistance change for ITUC gel. (**C**) The current-voltage sweep of ITUC gel and UT gel from -50 mV to 50 mV. (**D**) The resistance change and gauge factor of ITUC gel during stretching. (**E, F**) The resistance change of ITUC gel under bending and compression.

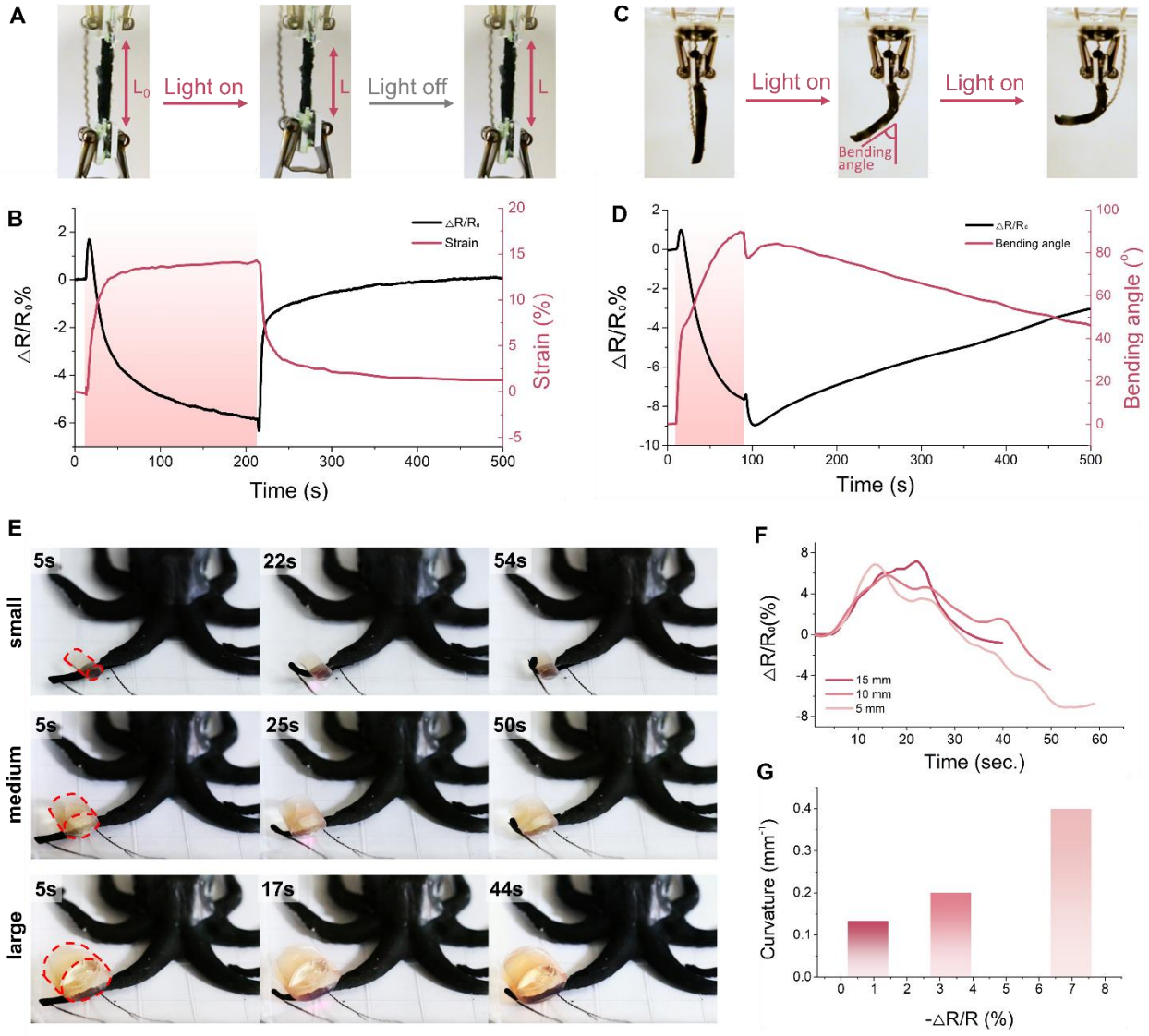

Fig. 4. Proprioceptive sensing of the ITUC gel. (**A**) Proprioceptive shortening and elongation under NIR light. (**B**) Resistance and length change over time. (**C**) Proprioceptive bending and unbending under NIR light. (**D**) Resistance and bending angle over time. (**E**) Shape recognition of an artificial octopus by wrapping the objects and monitoring the resistance. (**F**) Resistance changes of the gel when wrapping different sized objects. (**G**) The correlation of resistance changes and curvatures of objects.

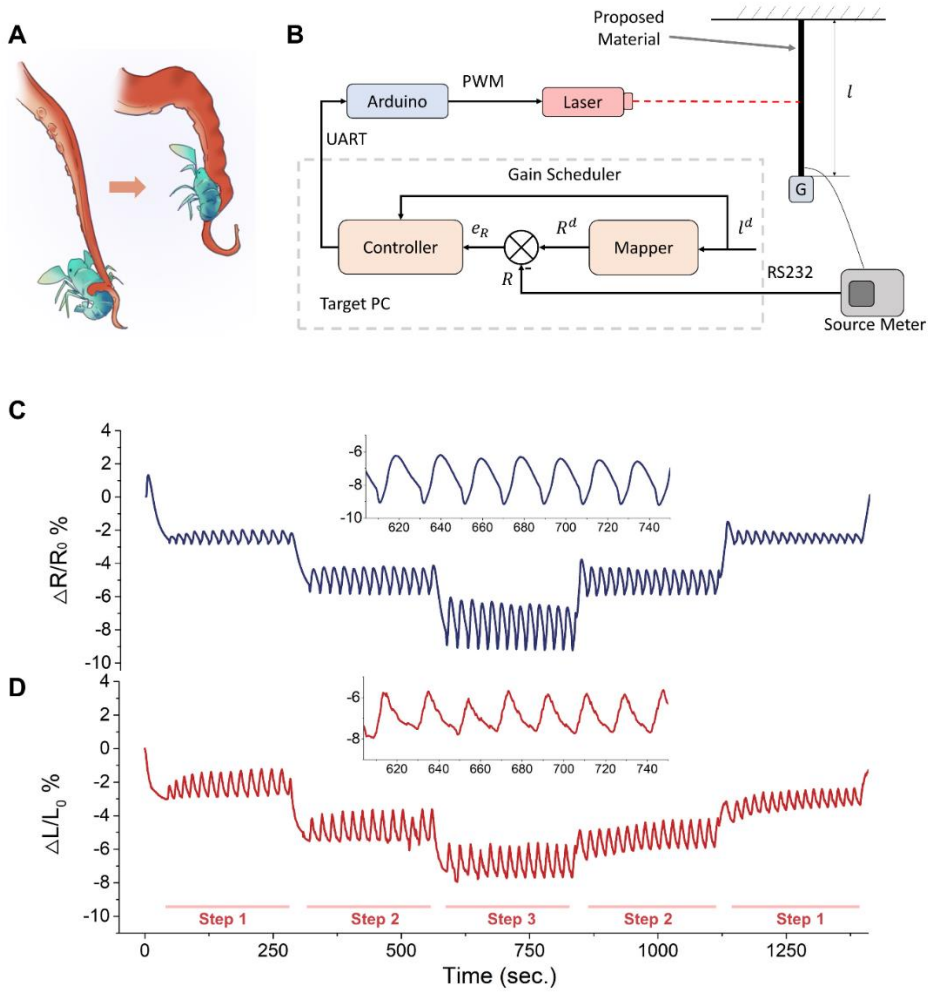

Fig. 5. Closed-loop control setup and performance. (**A**) The schematic of hydrogel arm length shortening control. (**B**) Block diagram of the closed-loop control system. A gain-scheduled bang-bang controller is running on the target PC, taking resistance measurements and sending control command to Arduino, which then generates PWM signals to drive laser intensity. (**C**) The relative resistance change versus time during closed-loop regulation. (**D**) The corresponding hydrogel arm strain versus time during closed-loop regulation, to step-wise reach the targeted arm lengths at three steps (original length L_0 = 25.0 mm, targeted lengths at, respectively, step 1 L_1 = 24.35 mm, step 2 L_2 = 23.75 mm, and step 3 L_3 = 23.31 mm). The insets in (**C**) and (**D**) showed the magnified curves between 600~750 seconds and their oscillations at a ~20-second period.

Supporting Information

Highly Stretchable Self-Sensing Actuator Based on Conductive Photothermally-Responsive Hydrogel

Chiao-Yueh Lo,[1,‡] Yusen Zhao,[1,‡] Cheolgyu Kim[1, ‡], Yousif Alsaid,[1] Roozbeh Khodambashi,[3] Matthew Peet,[4] Rebecca Fisher,[5,6] Hamid Marvi,[7] Spring Berman,[7] Daniel Aukes,[3] Ximin He[*,1,8]

[1]Department of Material Science and Engineering, University of California Los Angeles, Los Angeles, CA, 90095 USA

[2]The Polytechnic School, Ira A. Fulton Schools of Engineering, Arizona State University, Mesa, AZ, 85212 USA

[3]Department of Mechanical and Aerospace Engineering, Arizona State University, Tempe, AZ, 85287 USA

[4]School of Life Science, Arizona State University, Tempe, AZ, 85287 USA

[5]Department of Basic Medical Sciences, University of Arizona College of Medicine-Phoenix, Phoenix, AZ, 85004 USA

[6]School for Engineering of Matter, Transport and Energy, Arizona State University, Tempe, AZ 85287 USA

Experimental section

1 Materials.

N-isopropylacrylamide (NIPAAm, ACROS Organics) was purified by recrystallization from a mixture of hexane and acetone (1:1) and dried in vacuum. Other materials include acrylic acid (AA, Fisher), N,N'-methylenebis(acrylamide) (BIS, Aldrich), ammonium persulfate (APS, ACROS), sodium dodecyl sulfate (SDS, Fisher), 2-hydroxyethyl methacrylate (HEMA), 1-(3-Dimethylaminopropyl)-3-ethylcarbodiimide hydrochloride (EDC·HCl), 4-dimethylaminopyridine (DMAP), Pyrrole (Py, ACROS), Phytic acid solution (50% (w/w) in H_2O, Aldrich), dimethyl sulfoxide (DMSO), acrylamide (AAm), and 2-hydroxy-2-methyl-1-phenyl-1-propanone (Darocur 1173, TCI America)

2 Characterization.

Scanning electron microscopy (SEM) was performed on a Zeiss Supra 40VP SEM at a magnification of 500X. The hydrogel samples were frozen in liquid nitrogen, lyophilized and then coated with gold/palladium by a sputter coater before being observed by SEM. Fourier-transform infrared spectroscopy (FTIR) spectra were obtained using Jasco FT-IR- 420 spectrometer with a KBr pellet as supporting material. Mechanical properties of the tactile hybrid hydrogel, including the stress-strain behaviors and Young's modulus (E), were investigated by a dynamic mechanical analyzer (DMA, TA Instruments, Q800).

3 Synthesis of poly[NIPAAm-co-AA-co-AA(HEMA)] nanogel.

Poly(NIPAAm-co-AA) nanogels were synthesized by free radical precipitation polymerization of NIPAM and AA with BIS as crosslinker, which is initiated by APS in the

presence of SDS[1] . First, 50 mL of deionized water in a round-bottom flask was bubbled with nitrogen gas for 5 min to remove dissolved oxygen. Then, 1.13 g NIPAAm (10 mmol), 0.0721 g AA (1 mmol), 0.0616 g BIS (0.4 mmol) and 0.27 g SDS were added to the flask and mixed with magnetic stir until completely dissolved. N_2 gas was gently passed through the mixture for 1 hour to allow micelles self-assembly, and then the system was heated up and kept at 70°C. Next, 0.023 g APS (0.1 mmol, dissolved in 1mL of water) was added to the solution to initiate the reaction. N_2 gas was continuously passed through the flask above liquid level for another 5 min and then the flask was sealed immediately. The polymerization was allowed to proceed for 50 min and terminated with an ice bath. The resultant nanogels were purified by dialysis (Mw cut-off=3500) in water for 48 hours.

The HEMA-functionalized poly(NIPAM-co-AA) nanogels with crosslinkable double bonds were fabricated by the esterification between HEMA and AA units in copolymer under the catalysis of EDC/DMAP[2]. 1.82 g HEMA (14 mmol), 2.39 g EDC·HCL (12.5 mmol), and 1 g of DMAP were added into the nanogel solution from previous step. The reaction was performed at room temperature and magnetic stirred for 4 hours. The resultant P[NIPAAm-co-AA-co-AA(HEMA)] nanogels were purified by dialysis (Mw cut-off =3500) in water for 48 hours followed by lyophilized into white foam and stored at 4°C.

4 Synthesis of BIS-crosslinked PNIPAAm hydrogel (BisH).

BIS-crosslinked PNIPAAm hydrogel with the same crosslinker density as HEMA in NanoH gel was synthesized by free-radical polymerization of NIPAAm monomer crosslinked with BIS using APS as initiator and TEMED as accelerator at 4°C. Specifically, 0.8476 g of NIPAAm and 7 mg of BIS were dissolved in 5 mL deionized water. Then, 114 μL of APS aqueous solution

(10 wt%) and 20 μL of TEMED were added and mixed thoroughly. The precursor was then rapidly transferred into molds with desired shape and sealed to allow gelation to occur.

5 Synthesis of strengthened nanostructured PNIPAAm hydrogel (NanoH).

0.07g of P[NIPAAm-co-AA-co-AA(HEMA)] nanogels were dispersed into 5 mL deionized water and bubbled with N_2 gas for 5 min to remove dissolved oxygen. Specifically, different amounts of NIPAAm monomer (0.8476 g, 0.5658 g, and 0.2826 g), 2.50 mg of BIS crosslinker, and 5 μL of photo-initiator, Darocur 1173, were added to nanogel solution, and the precursor was cooled down in ice bath to prevent PNIPAM precipitation and structure collapse above LCST which eliminates the thermal-responsive behavior during the exothermic polymerization. The precursor was then injected into customized molds and polymerized under UV irradiation for 60 seconds (Dymax BlueWave 200, 320-395nm, 17W/cm^2) in an ice bath. The NanoH hydrogels fabricated from 0.8476g of monomer were used to carry out the equilibrium deswelling ratio measurements, while the hydrogels fabricated from 0.5658 g of monomer were used to carry out tensile stress-strain curves measurements and soft-robotics fabrication due to their best balance between mechanical properties and responsiveness.

The sample thickness was limited to 3 mm because for thicker polymerization, uniform temperature profile control over the material is more challenging and the mass diffusion is limited. It was found that lack of uniform temperature profile leads to non-uniform physical properties of the resulting gel. This can be further improved by optimizing the hydrogel morphology from closed pore to open pore, leading to improved water diffusion rate[3,4].

6 Synthesis of nanostructured conductive polypyrrole/PNIPAAm hydrogel (c-NanoH).

c-NanoH was fabricated with a 2-step method. First, the nanostructured hydrogel was immersed in DMSO for solvent exchange from water to DMSO. Next, the hydrogel was immersed in DMSO solution containing pyrrole (1.8 mol L^{-1}) doped with phytic acid (0.2 mol L^{-1}) and allowed pyrrole monomer diffusion into gel for 1 hour. The phytic acid serves as the dopant and also crosslinker, crosslinking the continuous network of PPy throughout PNIPAAm matrix[5,6], with each phytic acid molecule providing two out of its six phosphate groups to bind with two PPy polymer chains. The resultant doped and interconnected PPy network offers more available paths for electron transport, which dramatically improved the conductivity of the hybrid hydrogel. Afterwards, the gel was transferred into an DMSO solution containing (0.05 mol mL^{-1}) of APS and heated up from 25 °C to 50 °C within 15 min to initiate PPy polymerization. This process was repeated for different cycles depending on the thickness of each sample. Specifically, for samples thinner than 2mm, PPy polymerization was repeated twice, while for samples thicker than 2mm, the process was repeated 3 times. This tunability of PPy density in the hybrid hydrogel by different repeating cycle was also used to fine-tune the conductivity, stiffness, swelling ratio, as well as response rate of actuators for more precise motion control. After in-situ polymerization of PPy, the resulting hybrid-hydrogel was rinsed and immersed in water to remove reactant residue and DMSO, followed by swollen in water overnight.

7 Measurement of strain-sensing performance.

To demonstrate the performance of our tactile hydrogel as a strain sensor, c-NanoH samples were connected to the electric circuit with a source meter (Keithley 2400) by attaching two copper electrodes on the two ends of each hydrogel. Samples were swollen in water overnight and kept moisten while testing in air. The hydrogel was then stretched to different length until

fracture while the distances between two electrodes and respective resistance values were being recorded and plotted. To further evaluate the resistivity dependence on strain, we assume hydrogels are incompressible with Poisson ratio at 0.5[7,8] to estimate cross-sectional areas under different strain, and the estimated resistivity derived from resistance, cross-sectional area and sample length was plotted over strain. Resistance change of hydrogel under small (<5% fracture strength) axial compressive load was also recorded in real-time and plotted over axial load, showing a nearly linear dependency at small deformation range.

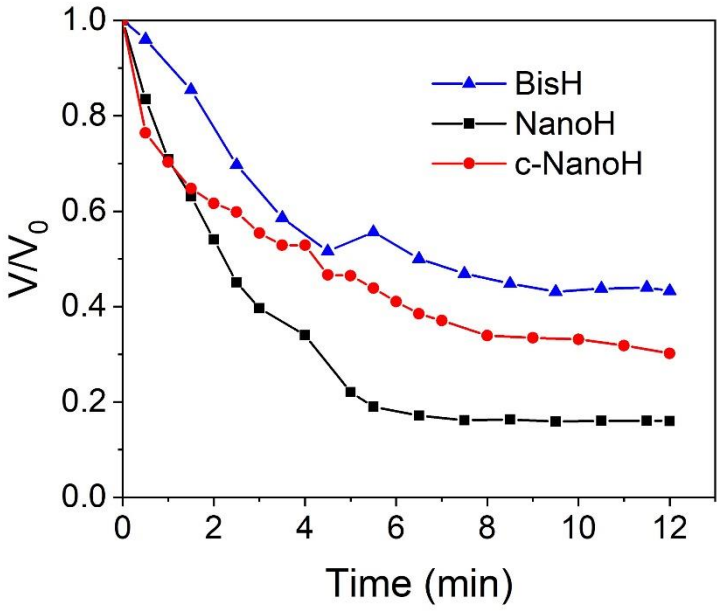

Figure S1: Volumetric shrinkage of different hydrogel actuators with the same crosslinking density in water at 50°C. BisH refers to PNIPAAm crosslinked with Bis, NanoH refers to hydrogel crosslinked with HEMA-modified nanogel, and c-NanoH referes to NanoH gels after in-situ polymerization of PPy.

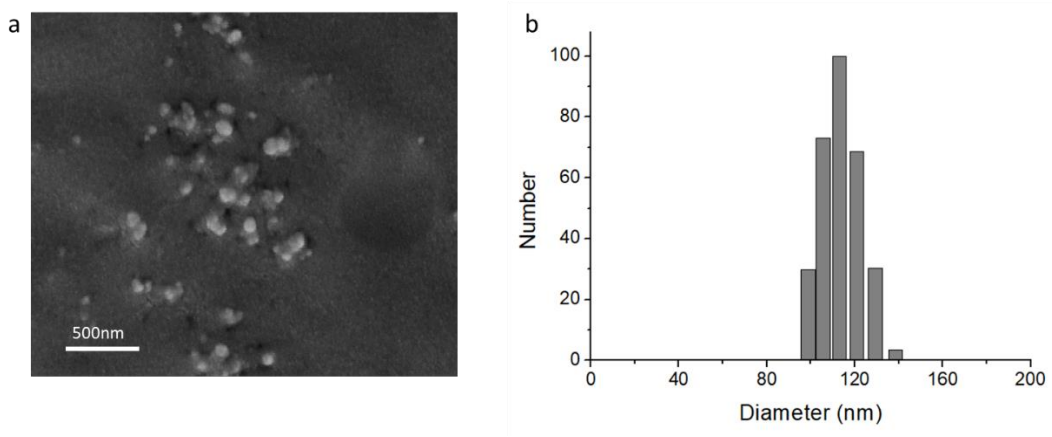

Figure S2: Morphology characterization of nanogel. a) SEM image of diluted nanogel particles. b) size distribution from dynamic light scattering (DLS) measurement.

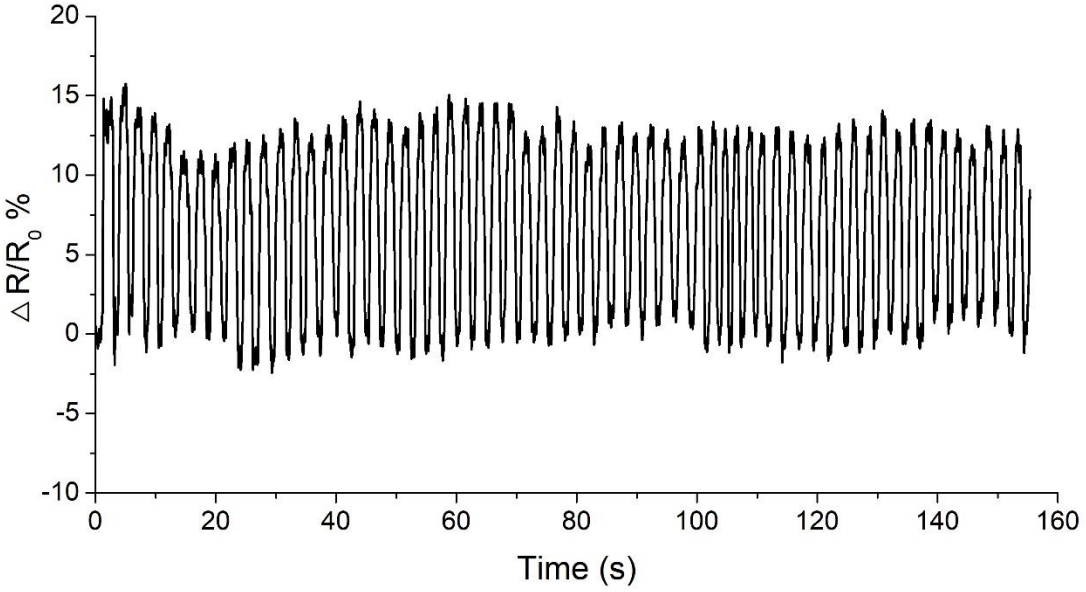

Figure S3: Reliability test of sensing performance of the hydrogel. The hydrogel was mounted on a finger and the resistance was to real-time monitor the finger deformation.

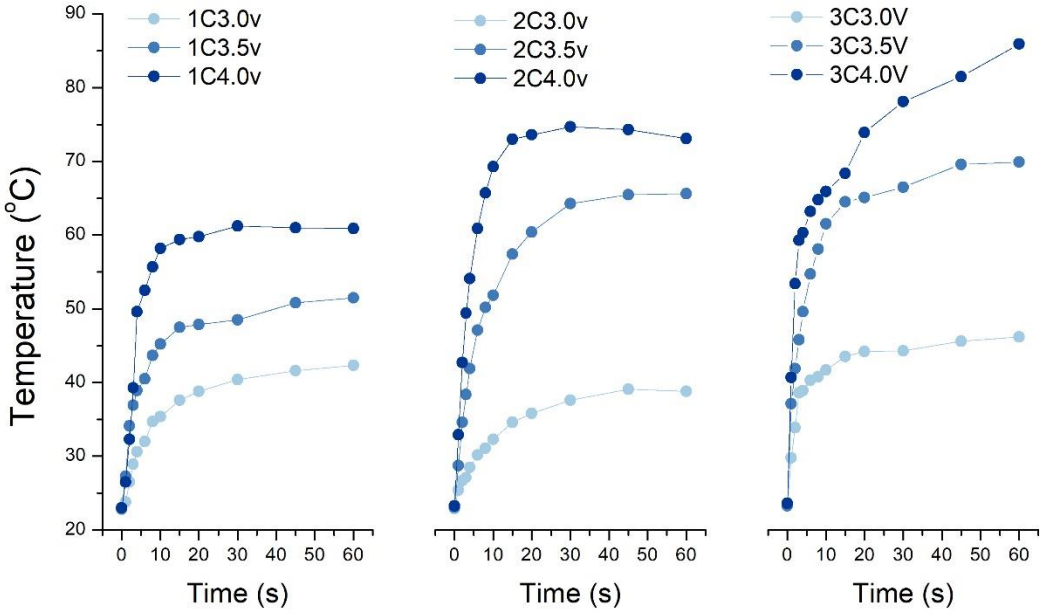

Figure S4: heat generation of hydrogels as a function of exposure time, light absorber amount, and light intensity

Simulation

When the hydrogel is immersed in the solvent, it tends to be swelled due to migration of the small molecules into the polymer network. This migration makes small molecules to interact with the long polymer chains and among themselves. Consequently, the hydrogel can change its shape and volume while the configurational entropy of the network decreases, but the configurational entropy of mixture increases.

To explain this complicated phenomenon, Flory and Rehner [5] developed free energy function which includes the effects of the entropy of stretching the network and the entropy of mixing the network polymers and the solvent molecules. Hong et, al[6],[7] took this Flory and Rehner's free energy function and formulated a theory of coupled mass transport and large deformation by considering nonequilibrium thermodynamics.

First, the stress-free dry state is taken as the reference state. Each small part of the gel network names after its coordinate X in reference state. In deformed state, this part of the network moves to a place with the coordinate $\mathbf{x}(\mathbf{X}, \mathrm{t})$ at time t.

The deformation gradient of hydrogel network can be expressed as

$$\mathbf{F} = \frac{\partial \mathbf{x}(\mathbf{X}, \mathrm{t})}{\partial \mathbf{X}} \tag{1}$$

Assume that the free energy density takes the functional form $\mathrm{W}(\mathbf{F}, \mathrm{C})$ which comes from two molecular processes stretching the network of the polymers (a function of the deformation gradient, **F)** and mixing the polymers and the small molecules (a function of concentration of the solvent, C). As mentioned above, the Flory-Rehner model is chosen for free energy density model and it is given by[5],

$$\begin{aligned} \mathrm{W}(\mathbf{F}, \mathrm{C}) &= \mathrm{W_s}(\mathbf{F}) + \mathrm{W_m}(\mathrm{C}) \\ &= \frac{1}{2}\mathrm{NkT}[\mathrm{F_{ik}F_{ik}} - 3 - 2\log(\det\mathbf{F})] - \frac{\mathrm{kT}}{\mathrm{v}}[\mathrm{vClog}\left(1 + \frac{1}{\mathrm{vC}}\right) + \frac{\chi(\mathrm{T})}{1 + \mathrm{vC}}] \end{aligned} \tag{2}$$

where N is the number of polymeric chains per reference volume, v is the molecule volume of solvent and $\chi(\mathrm{T})$ is a temperature dependent dimensionless property representing the enthalpy of mixing. T and k are the temperature and the Boltzmann constant, respectively.

Since the migration process of the solvent is fairly slows, it is assumed that each differential element of the gel is taken to be locally in a state of equilibrium, even though elements of the gel are not in the equilibrium with each other in different locations. Therefore, it is assumed that local equilibrium by neglecting viscosity associated with local rearrangement of molecules. Define the nominal stress as

$$s_{ik} = \frac{\partial W(\mathbf{F}, C)}{\partial F_{ik}} \tag{3}$$

In addition, when the gel has local equilibrium state with the solvent and the mechanical load, the chemical potential of the solvent is homogeneous in the external solvent and in the gel and can be expressed as

$$\mu = \frac{\partial W(\mathbf{F}, C)}{\partial C} \tag{4}$$

Since the chemical potential of the solvent is a constant at the equilibrium state, another free energy function $\widehat{\mathbf{W}}(\mathbf{F}, \mu)$ is introduced by using a Legendre transformation as**,**

$$\widehat{\mathbf{W}}(\mathbf{F}, \mu) = \mathbf{W}(\mathbf{F}, C) - \mu C \tag{5}$$

Consequently, new free energy function is defined as a function of the deformation gradient of network and the chemical potential of the solvent molecules.

All molecules in a gel are incompressible, and the volume of the gel is the sum of the volume of the dry network and the volume of the pure liquid solvent. So, the condition of incompressibility is expressed by

$$1 + vC = \det\mathbf{F} \tag{6}$$

Combining equation (5) and (6), the equation (2) becomes,

$$\widehat{W}(\mathbf{F},\mu) = \frac{1}{2}NkT[F_{ik}F_{ik} - 3 - 2\log(\det\mathbf{F})]$$
$$-\frac{kT}{v}\left[(\det\mathbf{F}-1)\log\left(1+\frac{1}{vC}\right)+\frac{\chi(T)}{1+vC}\right]-\frac{\mu}{v}(\det\mathbf{F}-1) \quad (7)$$

The relationship between normalized true stress (by kT/v) of hydrogel and the deformation gradient is expressed as a function of the equilibrium swelling ratio λ_{eq},

$$\frac{\sigma}{kT/v} = \frac{\partial\widehat{W}(\mathbf{F},\mu)}{\partial F_{ik}}\frac{F_{ik}}{\det\mathbf{F}} = \frac{Nv}{\lambda_{eq}^2}\left(\lambda_{eq}-\frac{1}{\lambda_{eq}}\right)+\ln(1-\frac{1}{\lambda_{eq}^3})+\frac{1}{\lambda_{eq}^3}+\frac{\chi(T)}{\lambda_{eq}^6} \quad (8)$$

Since hydrogel is stress-free state during free swelling under no mechanical load, the enthalpy of mixing $\chi(T)$ also can be expressed with equilibrium swelling ratio λ_{eq}.

$$\chi(T) = -\lambda_{eq}^6\left(\frac{Nv}{\lambda_{eq}^2}\left(\lambda_{eq}-\frac{1}{\lambda_{eq}}\right)+\ln\left(1-\frac{1}{\lambda_{eq}^3}\right)+\frac{1}{\lambda_{eq}^3}\right) \quad (9)$$

The free energy density function $\widehat{W}$ is function is obtained with a deformation gradient of the network, **F**, and the chemical potential of the solvent, μ, as the independent variables. This function can be implemented in FEM simulation by a user-defined hyperelastic material node under solid mechanics interface to describe the constitutive relation.

To implement transient behavior of gels into FEM simulation, Zhang et, al[9] and Zheng et, al[10], considered the transient behavior of gel diffusion by an analogy between mass diffusion and heat transfer with a rigorous consideration of large deformation.

Let $j_i(X,t)$ be the number of the small molecules per unit time crossing per unit area in the current state. The flux of the solvent is linearly proportional to the gradient of the chemical potential of the solvent and is expressed as a well-known equation[11]

$$j_i = -\frac{cD(T)}{kT}\frac{\partial \mu}{\partial x_i} \tag{10}$$

where c(X,t) is the number of the small molecules per unit volume in the current state and D(T) is the temperature dependent intrinsic diffusivity.

Another expression of the flux is the number of molecules crossing the element are per unit time. Let material element of area be $N_K dA(\mathbf{X})$ in the reference state and $n_i da(\mathbf{X})$ in the current state. The relationship between the reference and the current state can be written as,

$$j_i n_i da = J_K N_K dA \tag{11}$$

From the definition, the true flex related to the nominal flux as,

$$j_i = \frac{F_{ik}}{\det \mathbf{F}} J_K \tag{12}$$

Since, the small molecules are not injected from external source and no chemical reaction occurs, the conservation of solvent molecules in current state is expressed as

$$\frac{\partial c(\mathbf{X}, t)}{\partial \mathbf{t}} + \frac{\partial \mathbf{j_i}(\mathbf{X}, t)}{\partial \mathbf{x_i}} = 0 \tag{13}$$

The true concentration relates to the nominal concentration as

$$c = \frac{C}{\det \mathbf{F}} \tag{14}$$

Combining equations from (10) to (14), the conservation of solvent molecules becomes

$$\frac{1}{\det\mathbf{F}}\frac{\partial(\det\mathbf{F}-1)}{\partial t}+\frac{\partial\left[-\frac{(\det F-1)D(t)}{kT\det\mathbf{F}}\frac{\partial\mu}{\partial x_i}\right]}{\partial x_i}=0 \tag{15}$$

This mass diffusion equation is directly implemented using the PDE interface of COMSOL Multiphysics.

To analyze the heat transfer triggered by photo-thermal conversion, the localized deswelling utilized by heat transfer process. The well-known heat transfer equation is,

$$\rho C_P\frac{\partial T}{\partial t}+\nabla(-k\nabla T)=0 \tag{16}$$

where ρ, C_p and k are the density, specific heat capacity and thermal conductivity of the hydrogel, respectively. The density and the thermal conductivity of dry gel and water are close enough to assume it is same. However, the specific heat capacity of hydrogel depends on amount of water contained in a gel, since specific heat capacity of water is much higher than that of dry gel. Therefore, effective specific heat capacity of the hydrogel is calculated as,

$$C_{P,eff}=\frac{1}{\det\mathbf{F}}C_{p,drygel}+\left(1-\frac{1}{\det\mathbf{F}}\right)C_{p,water} \tag{17}$$

Finally, the free energy density function for hydrogel, the transient swelling model and the heat transfer model are implemented together using solid mechanics, PDE and heat transfer interfaces in COMSOL Multiphysics.

Reference

1. Gan, T., et al., Journal of Materials Chemistry (2010) **20** (28)

2. Chen, M., et al., Angewandte Chemie-International Edition (2013) **52** (38), 9961

3. Khodambashi, R., et al., Advanced Materials (2021), 2005906

4. Alsaid, Y., et al., Advanced Materials (2021), 201701938

5. Zhao, F., et al., Accounts of Chemical Research (2017) **50** (7), 1734

6. Shi, Y., et al., Advanced Functional Materials (2015) **25** (8), 1219

7. Hong, W., et al., Journal of the Mechanics and Physics of Solids (2008) **56** (5), 1779

8. Xiao, Z., et al., Acta Mechanica Solida Sinica (2012) **25** (5), 550

9. Zhang, J., et al., (2009) **105** (9), 093522

10. Duan, Z., et al., (2013) **80** (4), 041017

11. Feynman, R. P., et al., (1965) **33** (9), 750

Chapter 4. Drug Delivery Through Inhalation Using Nanoparticles

1. Introduction

Design concept

This research seeks to develop nanotherapeutics to deliver via inhalation an ultra-short course tuberculosis treatment regimen, for both drug-sensitive and drug-resistant tuberculosis (TB). Currently, an extremely long and burdensome course of antibiotic treatment is required to treat TB, which are 6-9 months for drug-sensitive TB and up to 2 years for drug-resistant TB. If this project is successful in developing nanotherapeutics capable of delivering the TB drugs in this regimen directly to the site of TB infection in the lung, and in particular to infected macrophages, the host cells for TB bacilli in the lung, then it may be possible to reduce the treatment time of TB even further to potentially 1-2 weeks, akin to the treatment time of most other types of lung infection. This would allow TB patients to be treated completely under medical observation and thereby virtually eliminate non-adherence to the treatment regimen and the further spread of TB from infected patients to others. Such an outcome would contribute in a major way to the eventual eradication of TB.

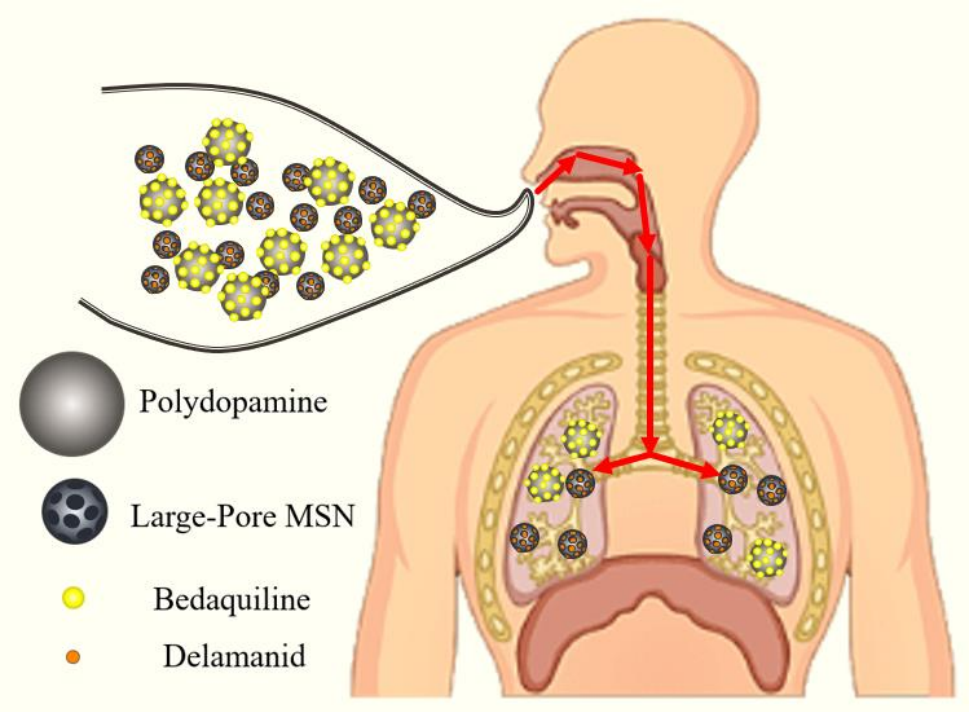

Figure 1. Design concept of the nanotherapeutics that deliver via inhalation an ultra-short course tuberculosis treatment regimen.

PRS Regimen V is a treatment regimen published by Professor Marcus A. Horwitz's research group at UCLA School of Medicine, using artificial intelligence-enabled approach, which consisting of Clofazimine (CFZ), Bedaquiline (BDQ), Delamanid (DLM), and Pyrazinamide (PZA) (**Figure 2**). Previous discoveries [1,2] have yielded a drug treatment regimen that reduces the time needed to treat TB by 85% in a murine model of pulmonary TB, a model highly predictive of treatment outcomes in humans. This novel drug regimen would treat both drug-sensitive TB and most cases of drug-resistant TB. This 4-drug regimen significantly reduces the time needed to achieve relapse-free cure in a mouse model of pulmonary TB to ~3 weeks.

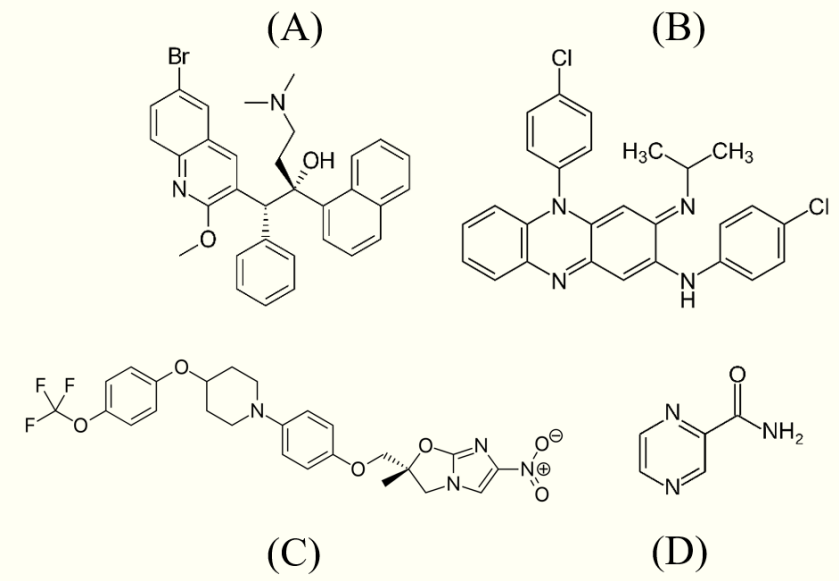

Figure 2. Chemical structures of the four component drugs in PRS Regimen V, namely (A) BDQ, (B) CFZ, (C) DLM, and (D) PZA.

Therefore, we collaborated with Professor Horwitz's group and aimed to deliver all four antibiotics via inhalation to the site of TB infection in the lung so as to further shorten the time needed to treat TB. The medium used in commercial inhalation nebulizers are usually water-based solutions to minimize irritation and toxicity. Although ethanol is a common additive to aid the hydrophobic drug solubility, the ethanol content is very limited due to its irritation to respiratory system. Unfortunately, three (CFZ, BDQ, DLM) out of the four drugs in PRS Regimen V are highly hydrophobic and are insoluble in water and ethanol. Thus, the challenge lies in designing a combination of hydrophilic carriers which can suspend hydrophobic drugs in water aerosols and eventually deliver all of the four drugs safely and effectively to the TB-infected macrophages.

Carriers

To maximize the drug loading for individual drugs, we utilized a mixture of large-pore mesoporous silica nanoparticles (LPMSN) and polydopamine (PDA) nanoparticles as drug carriers. Mixing multiple carriers have allowed us to 1) bring total carrier concentration to above the saturation limit of individual carrier, and 2) take advantage of different drug carriers that has the best affinity to each drug. This concept was further used to improve the overall drug delivery of both BDQ and DLM successfully.

In our previous work, we have already demonstrated that with mesoporous silica nanoparticles (MSN) as the carrier and acetophenone as the chaperone, the CFZ loading capacity can reach as high as 26.8% [3]. Therefore, in this research, we focused on improving the delivery of the other drugs, namely DLM and BDQ, through two strategies. The first strategy was to enlarge the pores in MSN so as to favor entry of large drug molecules into the nanopores. The second strategy was to implement a dual-carrier system to deliver the two target drugs BDQ and DLM simultaneously. The advantages of introducing a dual-carrier system include: 1) adding a second carrier to a saturated single-carrier system pushes the total carrier concentration to above the saturation limit of individual carrier, and 2) individual carrier acts as a minor carrier of the less feasible drug and contributes considerably to the overall drug loading capacity.

MSNs have aroused much attention as a hydrophilic nano-carrier for drug delivery. Their characteristic properties include high surface area (about 1000 m^2/g), large pore volume (1 cm^3/g), tunable pore sizes (2~20nm), easy surface functionalization, and high biocompatibility [4-7]. These exceptional intrinsic properties grant MSNs the flexibility to carry a wide variety of cargos,

such as drugs [3,8,9], genes [10,11], proteins [12,13], and other biomolecules for in vitro or in vivo biomedical applications. The easiness of functionalization also provides the accessibility to effective labeling on MSNs, such as incorporating fluorescence components, rare earth metals, radioactive elements, and magnetic responsive cores. That is to say, with proper integration of labeling and imaging technique, MSNs can simultaneously serve as nano-carriers and image contrast agents for diagnostics and therapeutics [14-17].

In this research, we further synthesized large pore MSNs (LPMSNs) with ~100nm in diameter and 7nm pore size by optimizing a water-cyclohexane emulsion synthesis previously reported in [18] (**Figure 3**) for maximized drug loading capacity. The larger pore size (7nm) makes it a more promising candidate for carrying large organic molecules.

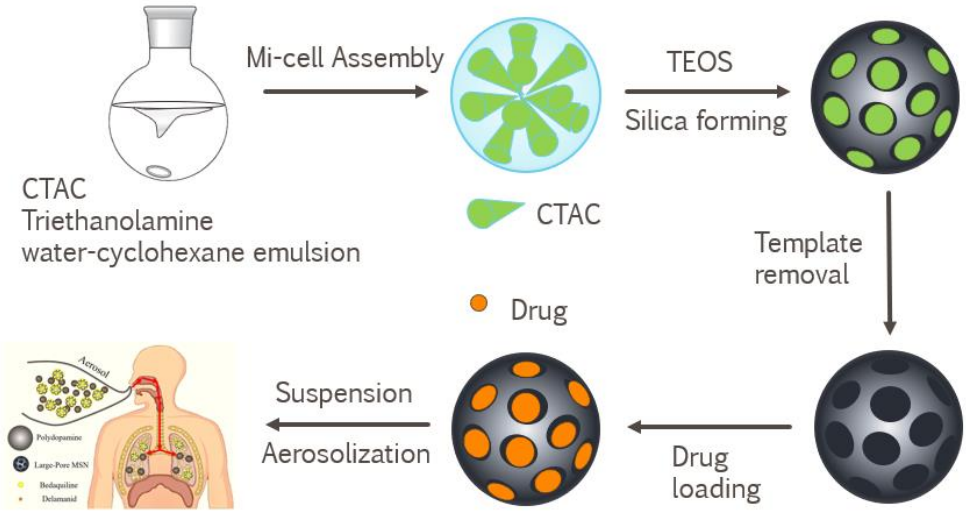

Figure 3. Fabrication protocol of LPMSNs

On the other hand, we found that polydopamine (PDA) nanoparticles are also potentially a highly promising alternative for achieving ultrahigh drug loading capacity for hydrophobic drugs.

PDAs and their derivatives have drawn attention in numerous applications due to their ability to form multiple kinds of secondary bonds with organic molecules, such as π-π stacking, hydrogen bonding, and dipole-dipole interactions [19,20]. PDA is also well known as a strong biomimetic adhesive to a wide variety of surfaces, a strong metal chelator, a visible-light absorbent, and a good bio-compatibility for biomedical applications [21,22].

As shown in **Figure 4**, with its abundant hydroxyl groups, PDA molecules are highly hydrophilic, so the nanoparticles are easily dispersed in water and polar solvents such as DMSO and ethanol. Thus, colloidal stability is not a challenge for PDA nanoparticles, as compared with MSNs. The melanin-like chemical structure of PDA also endows it with good biocompatibility.

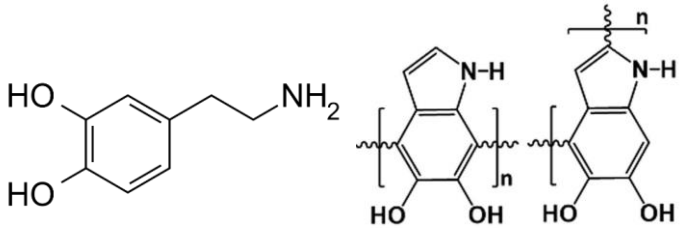

Figure 4. The chemical structures of dopamine (left) and polydopamine (right).

Polydopamine nanoparticles were typically synthesized by oxidative self-polymerization, but can also be synthesized by alkaline-, metal ion-, or oxidant-initiated reaction under neutral or acidic conditions, or via electrochemical methods. The polymerization mechanism of PDA remains controversial, but there is general agreement that the initiation step involves deprotonation and oxidation of dopamine. Specifically, we have synthesized PDA nanoparticles (PDA-Fe) through Fe(III) catalyzed and oxygen initiated polymerization at pH 10 in an ethanol/water mixture (**Figure 5**).

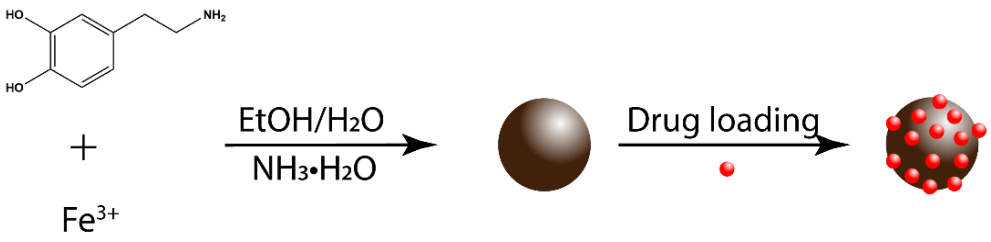

Figure 5. PDA-Fe nanoparticles were synthesized via iron-catalyzed, self-assembly polymerization of dopamine monomers. Afterwards, the drugs were adsorbed on the surface of nanoparticles through polydopamine's strong adhering properties.

Although the synthesis procedure itself is usually simple, the kinetics and proper control of particle morphology are complicated. The formation of nanoparticles involves multiple factors, such as pH, monomer concentration, temperature, solvent composition, and solubility parameters of each component in the system, while each of these factors can influence particle size and shape. Thus, the main challenge of PDA nanoparticle synthesis is finding the proper balance between the aforementioned factors and the optimized process window.

Performance Evaluation

For fundamental characterization, we have assessed particle size distribution using dynamic light scattering (DLS), particle morphologies using Transmission Electron Microscopy (TEM) and Scanning Electron Microscopy (SEM), surface modification properties and dispersibility using zeta-potential technics, and pore properties using nitrogen adsorption BET.

To evaluate the performance of drug carriers, the nanotherapeutics were first characterized with drug loading and release capability under abiotic conditions, and subsequently for safety and capacity to kill Mycobacterium tuberculosis, the causative agent of TB, in vitro in macrophage

cell cultures. Finally, the optimized nanotherapeutics were evaluated for safety and efficacy in treating tuberculosis in a murine model of pulmonary TB when administered via inhalation, both alone and in combination with oral therapy with the same drugs.

2. Key Words

Tuberculosis, Mycobacterium tuberculosis, Therapeutics, Nanotherapeutics, Inhalational Nanotherapeutics, Multi-Drug Resistant Tuberculosis, Extensively Drug-Resistant Tuberculosis, Mesoporous Silica Nanoparticles, Polydopamine Nanoparticles, Nanoparticles for antibiotic drug delivery

3. Results and Discussions

Carrier Fabrication and Fundamental Characterizations

PDA-Fe nanoparticles were synthesized by the aforementioned Fe(III) catalyzed and oxygen initiated polymerization at pH 10 in an ethanol/water mixture. The resulted PDA-Fe nanoparticles were examined under SEM and TEM, as shown in **Figure 6A** and **Figure 6B**. In contrast to PDA-Fe, LPMSN particles are smaller in diameter and with well-defined nanometer scale pores that are capable of physically encapsulating big drug molecules (**Figure 6C, Figure 6D**). Furthermore, the major interactions between PDA-Fe and cargo is secondary bonding, whereas LPMSN adsorbs cargo with a combination of physical adsorption and trapping. In other words, the drug loading capability should be more sensitive to LPMSN's surface properties and chemical modification than to PDA-Fe. It has been found that TEOS precursor concentration

controls the particle size, while reaction temperature and reaction time controls the pore size [18]. The radial large-pore structure formation relies on the self-assembly of CTAC micells, thus the particle morphology is highly dependent on the reaction conditions. Because of this sensitivity, surface modifications must be optimally conducted post-synthesis instead of synthesis using a one-pot reaction. By fine-tuning the TEOS precursor concentration, reaction temperature, and reaction time, we found the condition window to produce 150 nm diameter particles having a narrow size distribution with a 7 nm average pore size, which matched our needs.

To make particles suitable to be engulfed by macrophages for good cellular uptake, and to avoid blocking the nebulizer channel, the nanoparticle size ought to be controlled to ~200nm with narrow size distribution. The particle size distributions of PDA-Fe nanoparticles and LPMSN were measured by dynamic light scattering (DLS), and the surface charge properties were characterized with zeta-potential technique (**Figure 7)**. The micelle-templated LPMSN showed narrow size distribution at 168.1nm, whereas the non-templated PDA-Fe nanoparticles showed a major peak at 195.6nm and an aggregation minor peak at 1408.9nm. The pore size distributions measured by BET suggested cone-shaped pore structure with averaged 7 nm diameter for LPMSN and non-porous sub-structure for PDA-Fe (**Figure 8B~C**), in accordance with the TEM examination (**Figure 6**).

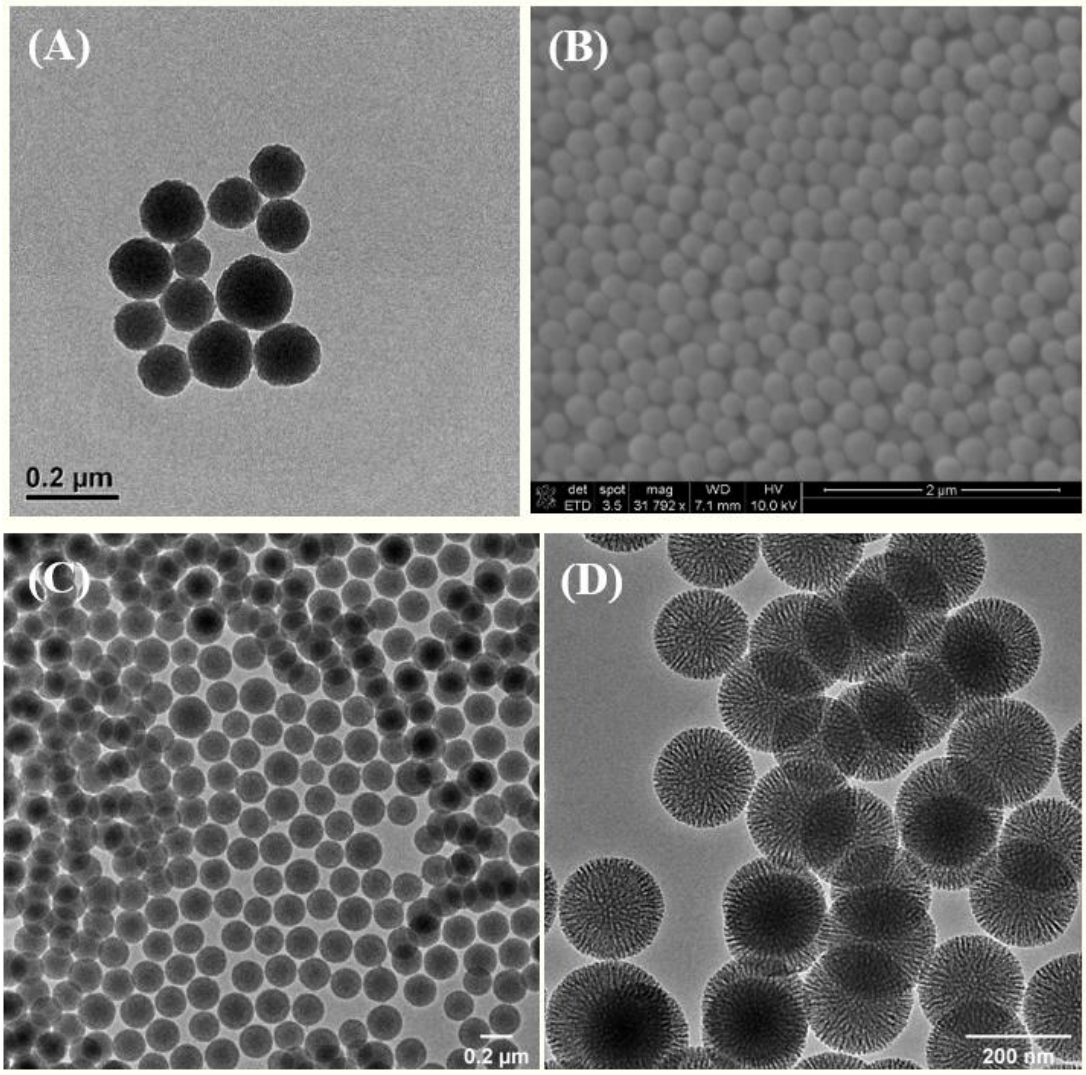

Figure 6. The (A) TEM image and (B) SEM images of PDA-Fe nanoparticles, and (C)(D) TEM images of LPMSNs showing radial, cone-shaped pores.

(A)

Particle	Averaged Hydrodynamic Size (nm)	Zeta Potential (mV)
PDA	301.0nm	-45.99±1.16 mV
LPMSN	168.1nm	-44.12±1.27 mV

(B) **(C)**

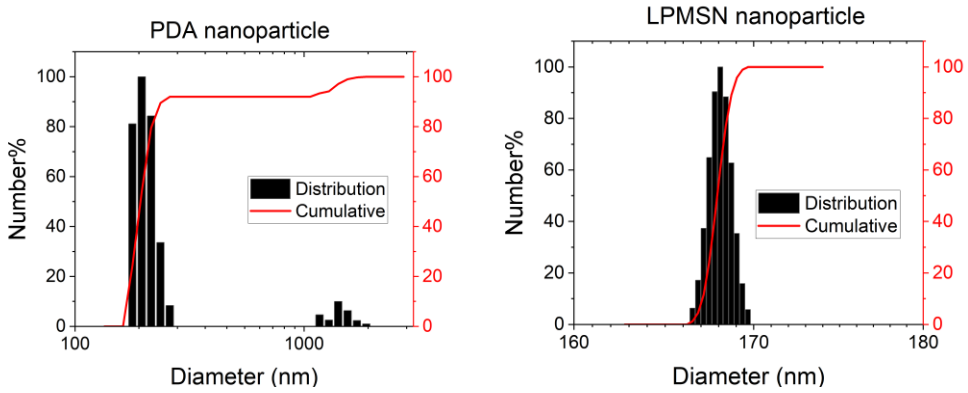

Figure 7. The (A) average hydrodynamic particle sizes measured from DLS, zeta-potentials, and particle size distribution profile of (B) PDA-Fe and (C) LPMSN.

(A)

Particle	Pore Type	Total Pore Volume (cc/g)	Surface Area (m^2/g)
PDA	Non-porous	0.08	31.39
LPMSN	Radial-shaped Nanopore	1.51	775.18

(B) **(C)**

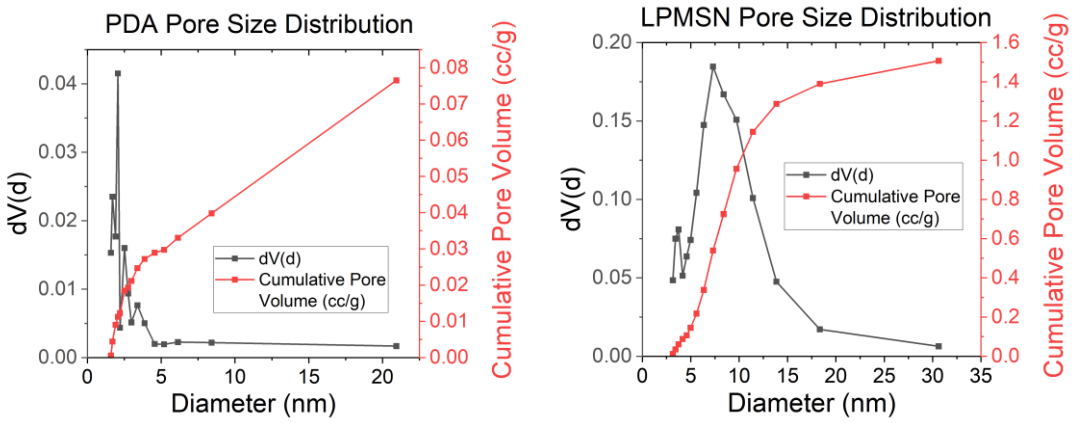

Figure 8. (A) Pore property comparison between PDA-Fe and LPMSN, and detailed pore size distribution of (B) PDA-Fe and (C) LPMSN measured from BET desorption branch.

Drug Loading Capacity of LPMSN

We have fabricated and studied DLM loaded LPMSNs and their capability and performance as drug carriers were evaluated by examination of carriers' DMSO extract with UV-Visible absorption spectroscopy (**Figure 9**). The UV-Vis absorption spectrum of carrier extract was taken and compared with the calibration curve of free drug, as well as the blank nanoparticle sample to evaluate the drug concentration. The DLM loading capacity of LPMSN was measured to be 13.3% (w/w).

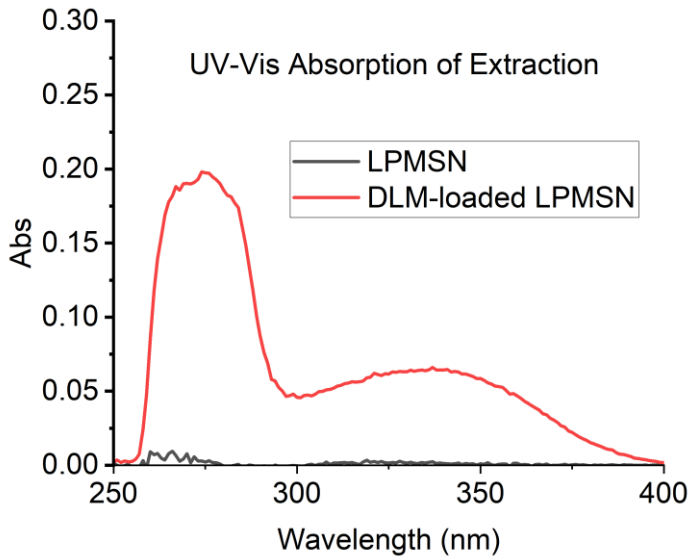

Figure 9. The UV-Visible absorption spectrum of the DMSO extracts of LPMSN (blank) and DLM drug-loaded LPMSN.

The mechanisms that affect loading capacity are complicated and involve changes in pore size and volume, steric hindrance, and altered surface charge. Thus, we modified the surfaces of LPMSNs with -NH_2, -COOH, and phosphonate groups with the intent of improving the DLM

loading capacity. The -COOH and phosphonate groups are generally used as negatively-charged surface modifiers, whereas the -NH_2 group is a typical positively-charged surface modifier. The three modifications successfully altered the surface properties of LPMSN as shown in the hydrodynamic size and zeta-potential results (**Table 1)**. Unfortunately, we found that -COOH modification resulted in a relatively 40.6% reduction in DLM loading capacity, and -NH_2 and phosphonate groups did not affect loading capacity significantly. Based on these results, we moved forward to further studies without surface modification.

Surface Modification	Hydrodynamic Size (nm)	Zeta Potential (mV)
LPMSN	168.1	-44.12±1.27
LPMSN-phosphonate	192.3	-76.18±2.30
LPMSN-NH_2	172.0	+28.81±0.14
LPMSN-COOH	152.0	-39.92±0.94

Table 1. Property and DLM loading capacity comparison when LPMSN surface is modified with phosphonate groups, amine groups, and carboxylate groups.

Drug Loading Capacity of PDA-Fe

We fabricated and studied BDQ loaded PDA-Fe nanoparticles, which have regular spherical shape and ~200nm size by fine-tuning the synthesis factors. Their capability and performance as drug carriers were evaluated by UV-Visible absorption spectroscopy and follow-up in vitro studies in Mycobacterium tuberculosis (Mtb)-infected human macrophages (**Figures S2, S3**). The drug loading capacity was quantified by measuring the concentration of free BDQ in the DMSO extract solution of PDA-Fe-BDQ by UV-Vis spectroscopy using absorption peak at

300nm (**Figure 10**). Note that the PDA-Fe particle is a strong light absorber and has significant absorption in all wavelength regions even at very low concentration (the grey curve in **Figure 10**), so we subtracted the absorption spectrum of blank PDA-Fe extract to compensate this error. The measured drug loading reached 24.9%.

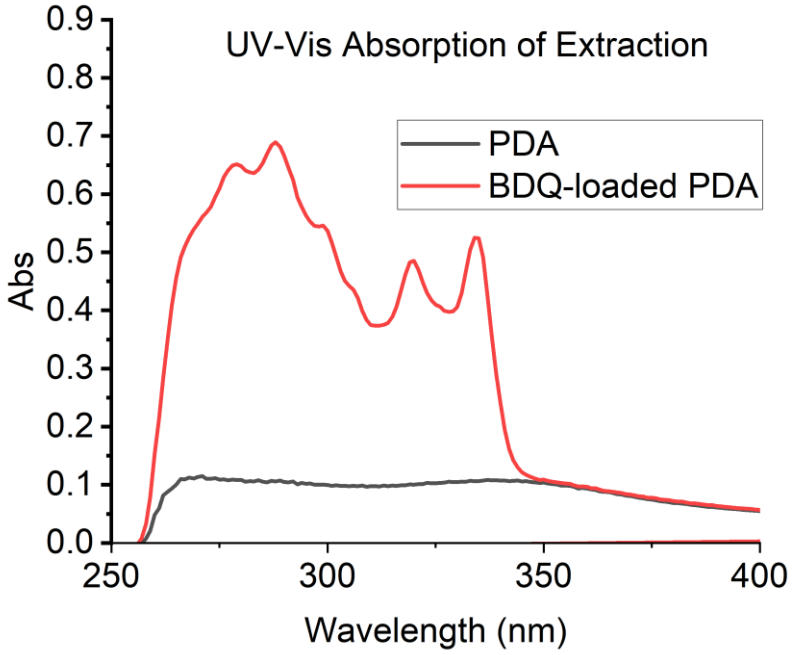

Figure 10. The UV-Visible absorption spectrum of the DMSO extracts of PDA-Fe (blank) and BDQ drug-loaded PDA-Fe (red).

Simultaneous multiple-nanocarriers for multi-drug delivery for inhalation studies

We took a dual-carrier strategy to improve the overall drug delivery of both BDQ and DLM. In our preliminary drug loading evaluation, PDA-Fe has higher DLM affinity than LPMSN, while LPMSN has higher BDQ affinity. Thus, we expect that in our dual-carrier mixture, the main carrier

of DLM would be LPMSN while the main carrier of BDQ would be PDA-Fe. We first examined the interactions between the two carriers by mixing PDA-Fe and LPMSN in pure water near their saturation limits (10mg/mL). Both carriers retained dispersed after 8 hours, and the TEM image of the dispersion showed that the two carriers retained intact structures and without undesired aggregation (**Figure 11**).

The drug-carrier interactions in our dual-carrier, dual-drug delivery system were studied by comparing the total drug loading between different drug-carrier combinations. In **Table 2**, samples #1 and #3 were prepared separately by loading a single drug into their major carrier. Samples #2 and #4 were prepared by loading a single drug into dual-carrier mixture in one-pot. Sample #5 was prepared by loading the two target drugs with dual-carrier mixture in one-pot. The results indicated that direct addition of a second carrier significantly increased the total drug carried. Next, we compared the drug loading capacities of the one-pot dual-carrier system (sample #5) with a reference sample: mixture of two single-carrier, single-drug samples (samples #1 and #3). The reference sample carried BDQ at 2.49mg/mL and DLM at 1.33mg/mL, whereas the one-pot loading sample reached 3.01mg/mL for BDQ and 1.80mg/mL for DLM. The one-pot loading of multi-drugs in multi-carriers not only outperformed the direct mixture of two single-carrier system, but also had a simpler preparation protocol. This result supported our assumption that an individual carrier also acts as a minor carrier of the less feasible drug. Therefore, the one-pot preparation was selected to be the desired preparation protocol for follow-up experiments.

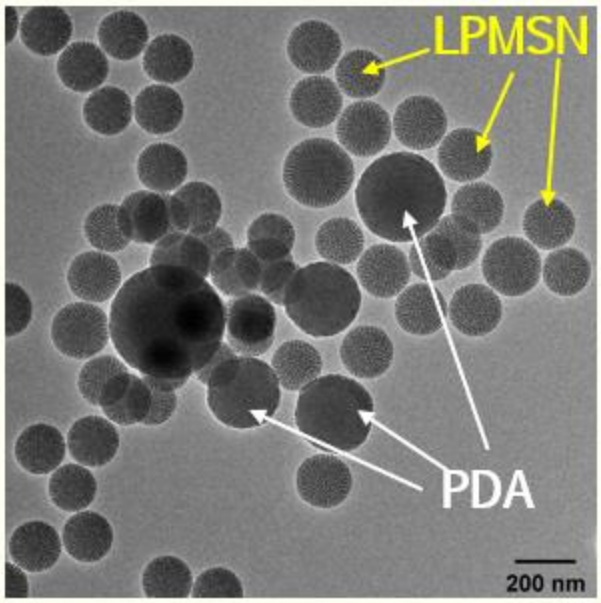

Figure 11. The TEM image of the PDA-LPMSN dispersion showed that the two carriers retained intact structures and without undesired aggregation.

Sample	Sample Composition				Drug Delivered (mg/mL)	
	Carrier (mg/mL)		Drug			
	LPMSN	PDA-Fe	DLM	BDQ	DLM	BDQ
1	10	0	+	-	1.33	-
2	10	10	+	-	2.33	-
3	0	10	-	+	-	2.49
4	10	10	-	+	-	3.56
5	10	10	+	+	1.80	3.01

Table 2. The drug loading capacity survey for one-pot, dual-carrier drug loading system.

Large-scale Fabrication of PDA-Fe Nanoparticles

The main practical challenge to PDA-Fe nanoparticle synthesis for in vivo studies is attaining sufficiently large-scale synthesis. For the in vivo bioassay, specifically for inhalation experiments with mice, several grams of carriers are required, which is a hundred-fold more than for in vitro cell studies. Unlike the synthesis of LPMSN, which yields hundreds of mili-grams of particles, PDA-Fe synthesis are usually in smaller scale and cannot fulfill the high productivity requirement for in vivo bioassay. Unfortunately, in our preliminary experiments, a straightforward multiplication of reagents in the PDA-Fe synthesis did not yield the same particle morphologies as the original synthesis protocol. Further examination revealed that the PDA-Fe nanoparticle morphology is not only dependent on the reactant ratio, but also dependent on the equipment factors such as vortex velocity, container shape, and heat dissipation during the reaction. Therefore, to meet the increased quantitative demand while maintaining good control of particle quality, we revised our synthesis equipment and revisited the relationship between particle morphology and multiple synthesis factors, including precursor concentrations, reaction temperature, solvent composition, and pH value. Eventually, we figured out that the solvent composition is the key factor impacting particle shape, while the pH is the key factor impacting particle size (**Figure 12**). With the optimized synthesis protocol, the yield could be improved by up to two-fold and the overall productivity by 5- to 10-fold while retaining particle properties comparable to that using the small-scale recipe (inset of **Figure 12**.). This new optimized synthesis procedure is expected to be more adequate for the upcoming in vivo studies.

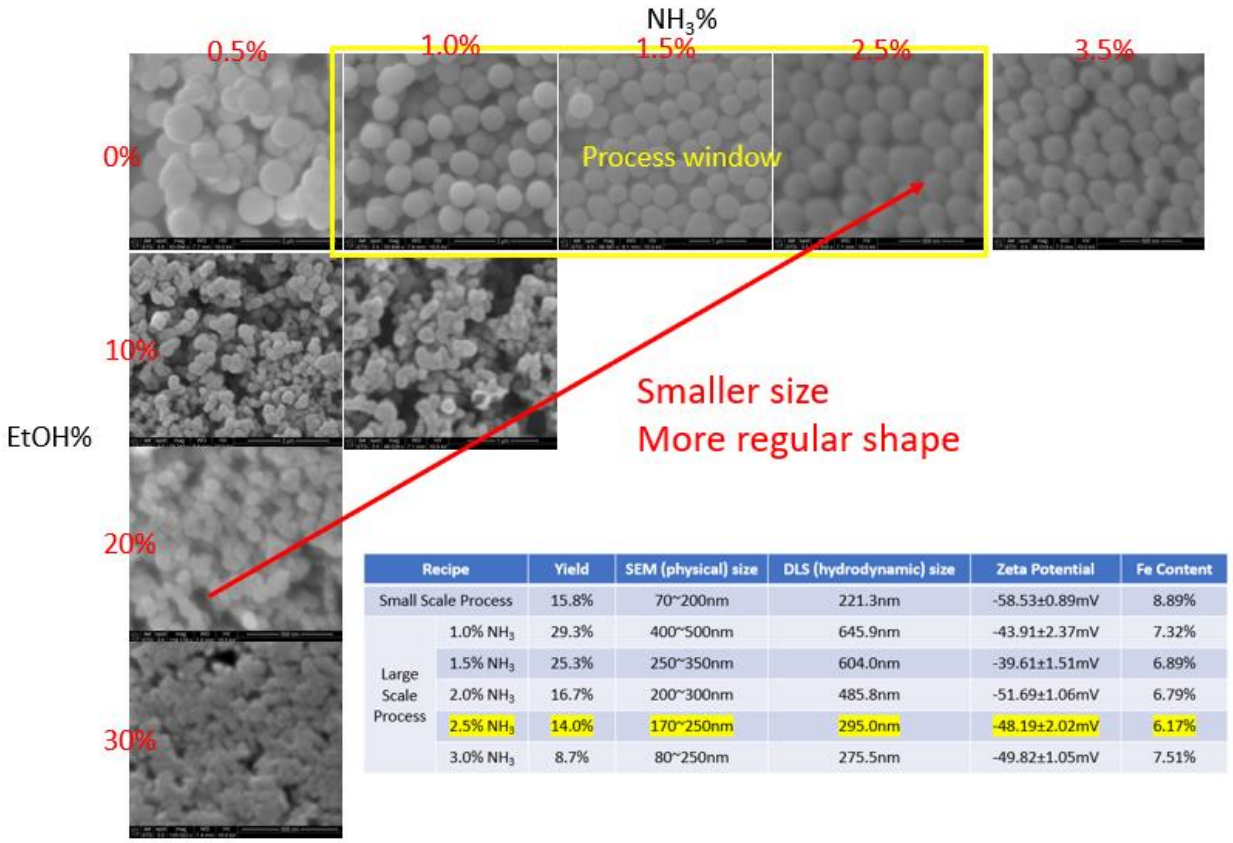

Recipe		Yield	SEM (physical) size	DLS (hydrodynamic) size	Zeta Potential	Fe Content
Small Scale Process		15.8%	70~200nm	221.3nm	-58.53±0.89mV	8.89%
Large Scale Process	1.0% NH_3	29.3%	400~500nm	645.9nm	-43.91±2.37mV	7.32%
	1.5% NH_3	25.3%	250~350nm	604.0nm	-39.61±1.51mV	6.89%
	2.0% NH_3	16.7%	200~300nm	485.8nm	-51.69±1.06mV	6.79%
	2.5% NH_3	14.0%	170~250nm	295.0nm	-48.19±2.02mV	6.17%
	3.0% NH_3	8.7%	80~250nm	275.5nm	-49.82±1.05mV	7.51%

Figure 12. Optimization of experimental factors, pH and solvent composition. The highlighted recipe in the table was selected for further research.

Effective Particle Labeling with Europium

We have doped PDA-Fe with a rare-earth metal ion, Europium (Eu(III)), to enable sensitive detection and monitoring of PDA-Fe nanoparticles in tissues by Ion Coupled Plasma Optical Emission Spectroscopy (ICP-OES) detection of the locations and concentration of particles in the in vitro and in vivo experiments. The Eu(III) ion was doped into PDA-Fe nanoparticles and bonded through the strong metal-ion chelation by the abundant hydroxyl groups. We reported that our ion

incorporation protocol achieved Eu(III) loading at ~3% (w/w against PDA-Fe) without causing change in the Fe(III) content, properties, or morphology (**Table 3, Figure 13**).

As a follow-up, we further compared the drug loading capacity and in vitro treatment efficacy of PDA-Fe-Eu with undoped PDA-Fe. The detailed bio assay results on cytotoxicity and treatment efficacy are presented in the supplemental information (**Figures S1, S2**). The loading capacities of BDQ evaluated by UV-Vis absorption was compared with bio assay, and the results showed consistent performance after Eu(III)-doping and supports the viability of using Eu(III) as a sensitive zero background label.

Sample	Hydrodynamic Size (nm)	Zeta Potential (mV)	Fe Content (wt%)	Eu Content (wt%)
PDA-Fe	304.5	-55.95±1.77	5.70%	0.00%
PDA-Fe-Eu	302.6	-53.30±1.43	5.65%	2.43%

Table 3. Fundamental properties comparison of PDA-Fe before and after Europium doping

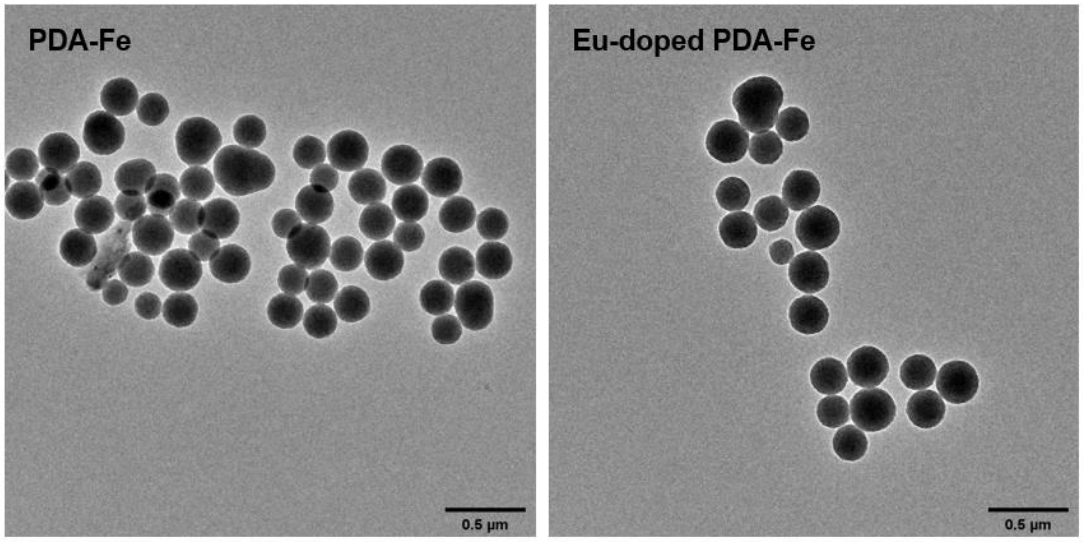

Figure 13. TEM images of PDA-Fe nanoparticles (left) and PDA-Fe-Eu nanoparticles (right). The images revealed that Europium doping does not affect PDA-Fe morphology.

In vivo Bioassays

Research published by Dr. Horwitz's group has shown that PRS Regimen V, comprised of bedaquiline (BDQ), delamanid (DLM), clofazimine (CFZ), and pyrazinamide (PZA), is highly efficacious in a murine model of tuberculosis. In comparison with the standard care of treatment, treatment with PRS Regimen V shortens the time to achieve a relapse-free cure by up to 75% [1]. In this research, we have conducted animal studies to determine whether we could further improve treatment efficacy, as assessed by lung burden of Mycobacterium tuberculosis, by combining pulmonary delivery of drug loaded nanoparticles with oral PRS Regiment V treatment.

Inhalational delivery of PDA-Fe nanoparticles loaded with BDQ (PDA-Fe-BDQ) was carried out using the In-Tox Inhalation delivery system equipped with a Lovelace aerosol nebulizer (**Figure 14**) and tracked with a DustTrak aerosol monitor in each of a 4 hour treatment session. We analyzed the aerodynamic size distribution of PDA-Fe-BDQ particles by quantifying the amounts of particles deposited on each of the stages of a seven-stage cascade impactor. We observed a very consistent particle distribution profiles from the six inhalation treatments over a period of two weeks (**Figure 15**). The majority of the particles are in the 0.1~1 micron range with a mean aerodynamic diameter (MMAD) between 0.26 to 0.38 microns, which is within the ideal particle size range for reaching lung periphery. We recovered the particles collected on filter samplers and determined the averaged inhaled dose for BDQ to be 80.6 μg per treatment, based on air flow rate, aerosol concentration, mouse minute volume, and duration of exposure. For intranasal administration, each mouse received 20 μl of PDA-Fe-BDQ per treatment at a concentration of 10 mg/ml. Per 100% BDQ loading (w/w) onto the PDA, this amounts to 200 μg of BDQ. While much of the intranasally administered PDA-Fe-BDQ is expected to deposit in the upper respiratory tract, 30~50% may reach the lower respiratory tract. As for inhalational delivery,

the inhaled PDA-Fe-BDQ particles are within the ideal aerodynamic diameter range for deposition deeper in the lungs including bronchi and alveoli.

To evaluate the stability and consistency of PDA-Fe-BDQ nanoparticles before and after use in the In-Tox inhalational therapy system, we recycled and examined the PDA-Fe-BDQ particle samples after inhalation experiments and compared with the sample properties acquired before inhalation experiments. The iron content of each sample was measured by ICP-OES. We also analyzed the physical particle size by TEM, hydrodynamic size by DLS (**Figure 16, Table 4)**, which were consistent with the aerodynamic size quantified by amounts of particles deposited on cascade impactor stages (**Figures 15**). In **Figure 16** and **Table 4**, sample #1 is the freshly-prepared sample before inhalation study, sample #2 is the sample of particles that passed through the 4μm filter within the In-Tox inhalational system, and sample #3 is the unused residue recollected from the nebulizer reservoir. Sample #2 has slightly smaller average size to the fresh sample, whereas sample #3 has dual-peak distribution with small particles having diameters of about 230 nm and large-sized aggregates at 450 nm. The different size distribution can be explained by the less volatile nature of larger aggregates in residue. On the other hand, the Fe(III) content and zeta potential of PDA-Fe-BDQ after the in vivo experiment were the same as those of the sample before the in vivo study. In summary, we have proven that the BDQ-loaded PDA-Fe particles are very stable and remain uniformly distributed along the whole inhalation study and will be the basic set-up for multi-drug delivery system.

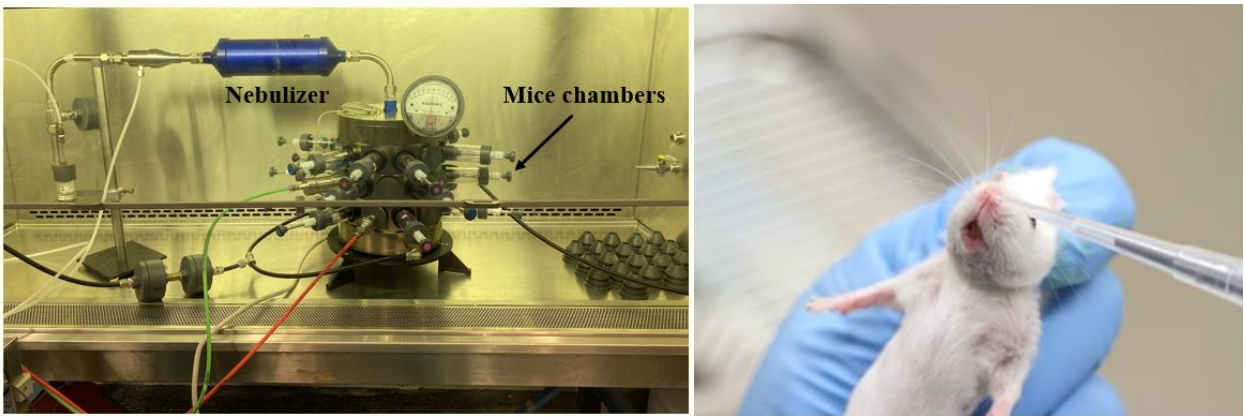

Figure 14. The two administration methods used for in vivo bioassay: The In-Tox inhalational system (left) and intra-nasal administration (right).

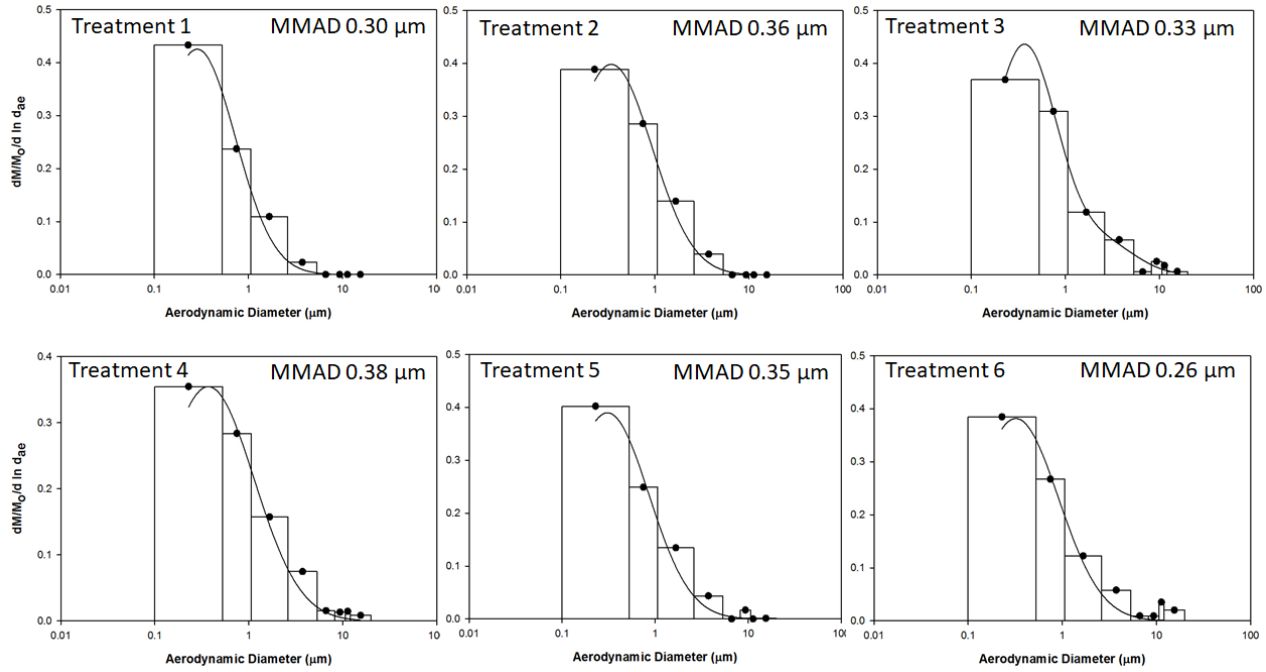

Figure 15. Size distribution of PDA-Fe-BDQ particles delivered by inhalation using In-Tox inhalational system.

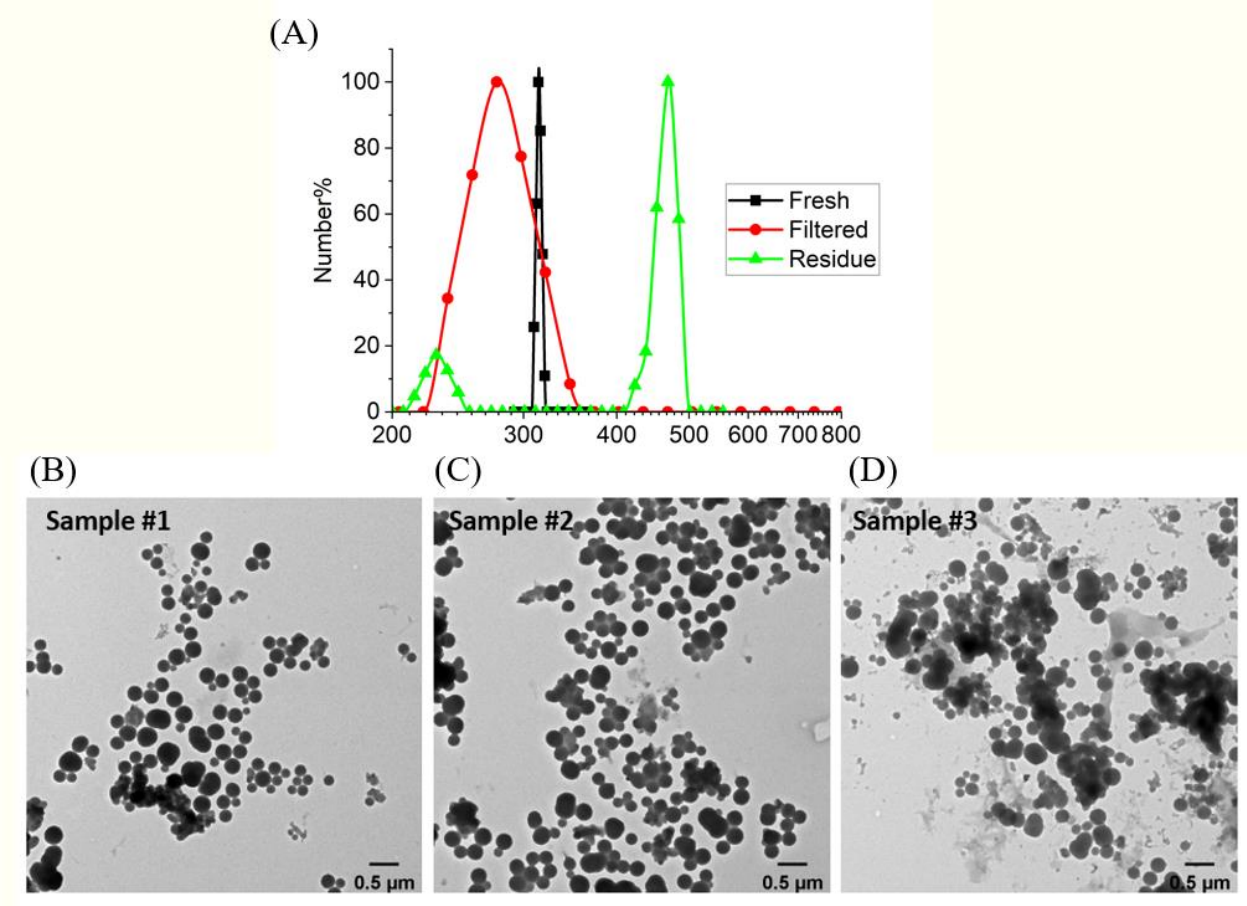

Figure 16. Comparison of (A) size distribution and particle morphology under TEM between (B) freshly-prepared PDA-Fe-BDQ, (C) filtered PDA-Fe-BDQ, and (D) recollected residue PDA-Fe-BDQ after inhalation therapy experiment.

Sample	Hydrodynamic Size (nm)	Zeta Potential (mV)	Fe Content (w%)
Sample #1 (Fresh)	314.6	-33.63±1.01	6.27%
Sample #2 (Filtered)	291.6	-41.89±2.06	5.18%
Sample #3 (Residue)	423.5	-32.05±2.62	5.27%

Table 4. Comparison of hydrodynamic size, zeta potential, and iron content between fresh PDA-Fe-BDQ (sample #1), filtered PDA-Fe-BDQ (sample #2), and PDA-Fe-BDQ residue (sample #3) after inhalation therapy experiment.

To evaluate the efficacy of PDA-Fe-BDQ, we first conducted animal studies comparing lung burden reduction of M. tuberculosis in mice treated with PRS Regimen V alone via oral route five days a week (Monday – Friday) to the reduction in mice treated with both oral PRS Regimen V and PDA-Fe-BDQ particles delivered by inhalation or intranasal administration three days a week (Monday, Wednesday, Friday) for one or two weeks.

We infected BALB/c mice with M. tuberculosis virulent strain Erdman by aerosol and initiated treatment two weeks post infection when the number of the organisms reached to 5×10^5 colony forming units (CFU) in the lungs. For treatment with PRS Regimen V, we administered 0.8mg of BDQ, 0.0166mg of DLM, and 3.7mg of PZA suspended in 0.15% agarose and one hour later 0.5mg of CFZ in 0.15% agarose separately to each mouse (~20g) by oral gavage.

Upon completion of inhalation therapy treatment, mice were euthanized and their lungs were aseptically removed. Lung homogenates were either serially diluted before plating (Sham-treated, PDA-BDQ alone) or without dilution for plating the entire lungs (all treatments with PRS Regimen V) on 7H11 charcoal agar. After incubation for 5 weeks, CFU on the plates was enumerated. Treatment with PRS Regimen V by oral gavage five days a week for one or two weeks reduced lung burden of M. tuberculosis CFU by 2.0 and 4.8 logs, respectively (**Figure 17**). In comparison, addition of inhalational or intranasal treatment with PDA-BDQ three times a week did not significantly decrease CFU. Treatment with PDA-Fe-BDQ alone by inhalation or intranasal route three days for two weeks reduced lung burden of M. tuberculosis by 0.0 and 0.2 logs, respectively.

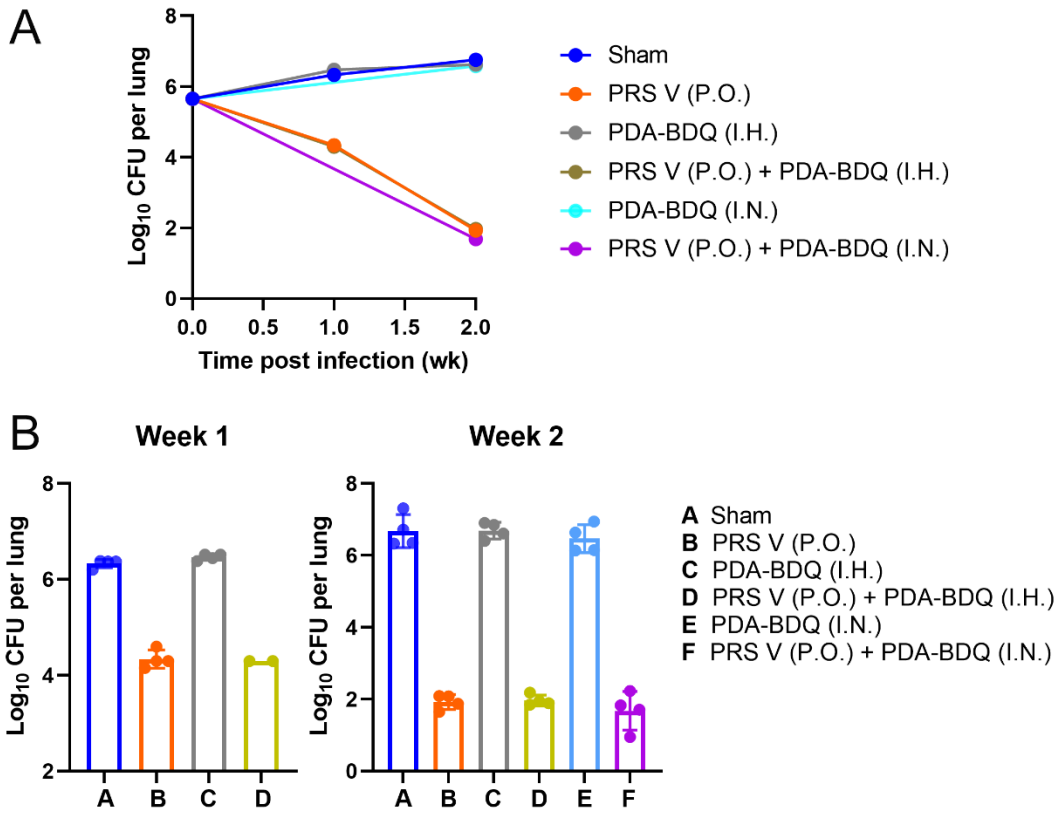

Figure 17. Treatment efficacy of PDA-BDQ administered via inhalation (I.H.) or intranasal (I.N.) route three days a week (Monday, Wednesday, Friday) with or without in combination with PRS Regimen V administered by oral gavage (P.O.) five days a week (Monday – Friday). (A) Lung burden of M. tuberculosis over the course of treatment. (B) M. tuberculosis CFU in the lungs after completion of one or two weeks of treatment. Data shown are mean ± SD.

Subsequently, we tested a mixture of PDA-Fe and LPMSN loaded with both BDQ and DLM (PDA-MSN-BDQ-DLM) through intranasal administration. We started with this setup because 1) lung burdens of M. tuberculosis in mice treated with PDA-Fe-BDQ averaged the lowest among all treatment groups, and 2) because it is more time efficient to deliver drugs with intranasal administration than inhalation administration. In detail, we compared the efficacy of lung burden

reduction of M. tuberculosis in mice treated with PRS Regimen V alone and addition of PDA-MSN-BDQ-DLM via intranasal administration five days a week (Monday – Friday) for two weeks. Loading of BDQ and DLM on the PDA-MSN mixture, which we refer to as PDA-MSN-BDQ-DLM^{Hi}, were 17.3% and 9.7% (w/w), respectively. Additional groups of mice received either sham treatment or treatment with PDA-BDQ (12% drug loading) or MSN-DLM (2.6% drug loading) alone. As our previous studies have shown that not only the drugs but also the drug ratios are important to efficacy, here we also included a group of mice to assess the treatment efficacy of PDA-MSN-BDQ-DLM^{Lo}, made by mixing PDA-BDQ together with MSN-DLM to achieve a ratio of ~50:1, to match the ratio in the oral gavage PRS Regimen V. All intranasal groups were given 20μL of the particles at a concentration of 10mg/mL per treatment, except for the PDA-MSN-BDQ-DLM^{Lo} group, which was given 29μL to match the amount of BDQ administered to the group treated with PDA-MSN-BDQ-DLM^{Hi}. **Table 5** shows the amount of BDQ and DLM administered to each group of mice.

		BDQ (μg/day)		DLM (μg/day)		BDQ/DLM Ratio	
Group	Treatment (Route)	PO	IN	PO	IN	PO	IN
A	Sham						
B	PRS V (PO)	800	0	17	0	47	
C	PRS V (PO) + PDA-BDQ (IN)	800	24	17	0	47	
D	PRS V (PO) + MSN-DLM (IN)	800	0	17	5.2	47	
E	PRS V (PO) + PDA-MSN-BDQ-DLM^{Hi} (IN)	800	34.6	17	19.4	47	1.8
F	PRS V (PO) + PDA-MSN-BDQ-DLM^{Lo} (IN)	800	34.6	17	0.69	47	50
G	PDA-MSN-BDQ-DLM^{Hi} (IN)	0	34.6	0	19.4		1.8

Table 5. The amount and ratio of BDQ and DLM administered by oral and intranasal routes.

Meanwhile, we monitored the weights of individual mice weekly upon arrival. Mice treated with PRS Regimen V had a net gain in weight suggesting that the treatment was well tolerated. Mice treated with PRS Regimen V and particles loaded with BDQ and DLM either individually or both, gained weight prior to infection and then lost 5% or less of their body weight at the end of the two-week treatment (**Figure 18**).

Treatment efficacy of PDA-SN-BDQ-DLM administered via intranasal route with or without in combination with PRS Regimen V administered by oral gavage was shown in **Figure 19**. Oral administration of PRS Regimen V reduced lung burden of M. tuberculosis by 5.5 logs. Addition of intranasal PDA-BDQ, MSN-DLM, or PDA-MSN-BDQ-DLM to the oral PRS Regimen V reduced lung CFU by 4.7 – 5 logs, which is a 0.5 – 0.8 log increase in lung burden compared with treatment with PRS Regimen V alone. This increase was statistically significant. Lung burden of M. tuberculosis in mice treated with intranasal PDA-MSN-BDQ-DLM^{Hi} was slightly lower than the sham-treated mice, but this difference is not statistically significant.

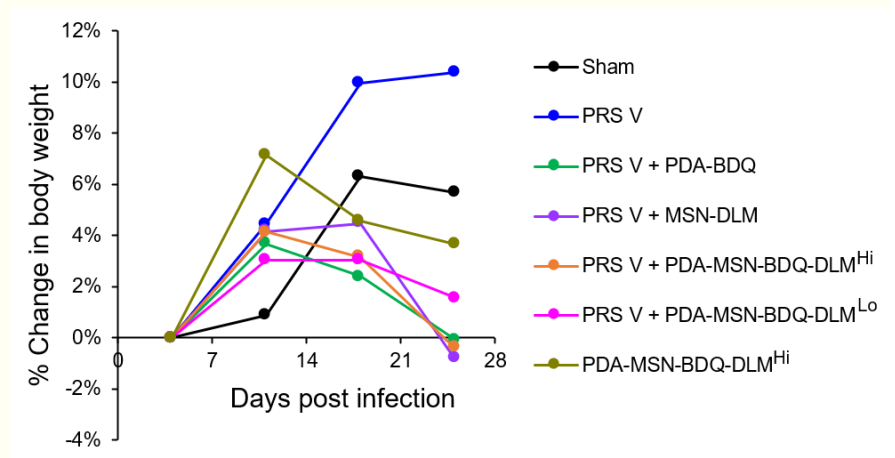

Figure 18. Mice were infected on Day 0, treated 5 days a week starting on Day 14, and euthanized on day 28 for determination of lung burden of M. tuberculosis. Weights of mice were monitored throughout the course of infection and treatment.

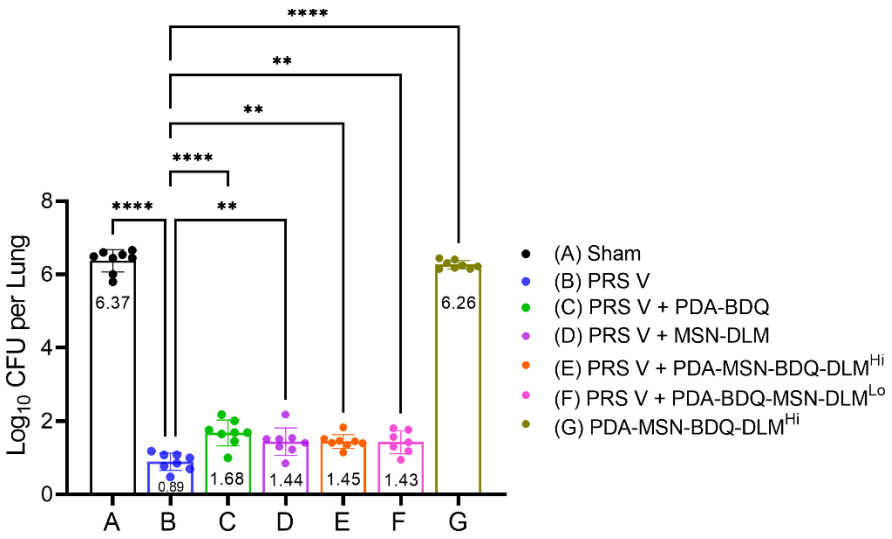

Figure 19. Treatment efficacy of PDA-SN-BDQ-DLM administered via intranasal route with or without in combination with PRS Regimen V administered by oral gavage. Mice were infected with virulent M. tuberculosis and treated for five days a week (Monday – Friday) for two weeks. Data shown are mean ± SD. Statistical analysis was performed using one-way ANOVA. **p<0.01, ****p<0.0001

4. Conclusion and Future Prospects

The goal of this project is to develop nanotherapeutics to deliver an ultra-short course tuberculosis treatment regimen, PRS Regimen V via inhalation. We had promising drug loading capability on two of the target drugs, BDQ and DLM, and we proved the concept of one-pot, multi-carrier, multi-drug delivery through benchtop characterizations and in vitro cell studies. However, to the current stage, the positive in vitro results were not reflected in both intranasal administration and inhalation administration study, due to that the macrophage uptake was not optimal in our in

vivo bioassay. Therefore, our next steps will be 1) modifying the nanoparticles to improve macrophage uptake, 2) designing protocols to incorporate the other drugs, specifically chemically bond PZA and physically encapsulate DLM in one particle, and 3) developing alternative carrier candidates, such as amphiphilic micelles.

First, to improve the macrophage uptake, we will study the multiple, complicated factors which affect inhalation therapy efficacy. Our next step is to develop strategies to fine-tune the carrier properties and applying surface modifications. For instance, it is found that the interactions between nano-carriers and pulmonary surfactant is crucial for the nanocarrier to transport through the pulmonary surfactant layer, where the particle size, surface charge, surface hydrophilicity are the key factors to the interactions [23-26]. We plan to synthesize smaller particles and apply positively-charged surface modification to improve the carrier transportation. Additionally, in the literature it is also reported that premixing silica nanoparticles with natural pulmonary surfactants or artificial surfactants helps the carrier transportation as well as internalization by the lung epithelial cells [27,28]. Therefore, in the near future, we plan to modify our LPMSN and PDA-Fe nanoparticles with surfactants mimicking natural pulmonary surfactant, or commercially available surfactants for respiratory distress syndrome treatment, such as Curosurf, in aim of improving macrophage uptake.

Secondly, for PZA delivery, an alternative carrier is required because unlike the hydrophobic BDQ, DLM, and CFZ, PZA is a hydrophilic drug and is highly soluble in water, ethanol and DMSO. In our preliminary experiments, PZA escaped easily from both PDA-Fe and LPMSN when the drug-loaded carriers were suspended in water. We proposed that modification of LPMSN surface with functional groups, followed by ester coupling can help anchor PZA molecules on LPMSNs. When PZA-loaded LPMSNs enter the target cell, the ester bonds will be

hydrolyzed by enzymes and the PZA will be released. We will then conduct detailed chemical characterization as well as cell studies to examine the PZA loading capacity and release efficiency.

Finally, we have proved the concept that multiple carriers can be beneficial to the total drug delivery amount in this research, so we will continue searching for alternative carriers for our multi-drug delivery system. We have identified several potential candidates inspired from state-of-the-art inhalation therapy and respiratory distress syndrome treatments, and we will conduct preliminary evaluations on the viability of a) amphiphilic micelles, b) micelle-encapsulated silica nanoparticles, and c) drug emulsions in perfluorocarbon media.

5. Experimental Section

Chemicals

Chemical reagents were purchased from Sigma-Aldrich, Fisher Scientifics, MedChemExpress LLC, Otsuka Pharmaceutical Co., and used as received unless noted otherwise. Triethanolamine (TEA; 98%, Aldrich), cetyltrimethylammonium chloride (CTAC; 25% aqueous solution, Aldrich), tetraethyl orthosilicate (TEOS; 99%, Aldrich), cyclohexane (99%, Aldrich), ammonium nitrate (NH_4NO_3; 99%, Aldrich), ethanol (200proof, Aldrich), toluene (certified ACS; Fisher), nitric acid (ACS reagent, 70%, Aldrich), nitric acid (trace metal basis, Aldrich), hydrochloric acid (HCl; 12N, certified ACS Plus, Fisher), hydrochloric acid (trace metal basis, Aldrich), (3-aminopropyl)triethoxysilane (APTES; 99%, Aldrich), 3-(triethoxysilyl)propionitrile (97%, Aldrich), 3-(trihydroxysilyl)propyl methylphosphonate (monosodium salt solution, 50wt% in water, Aldrich), dopamine hydrochloride (Aldrich), ferric chloride hexahydrate (97%, Aldrich), ammonium hydroxide solution (15N aqueous solution, Aldrich), europium(III) chloride hexahydrate (99.9%, Aldrich), Bedaquiline (BDQ; MedChemExpress, LLC), Delamanid (DLM; Otsuka Pharmaceutical Co.). Anhydrous toluene was obtained by distilling toluene with calcium hydride under dry nitrogen flow.

Fabrication of large pore mesoporous silica nanoparticles (LPMSN)

In a 100mL round-bottom flask, 0.18g of triethanolamine (TEA) was added to a mixture of 36mL water and 24mL CTAC solution. The solution was stirred at 60˚C for two hours to allow micelle self-assembly. Then, a mixture of 1mL TEOS and 19mL cyclohexane was added to the flask drop wisely to form a milky-white emulsion. The reaction was carried out in ambient air at 60˚C with reflux for another 24 hours. After the reaction, the cyclohexane layer was carefully

removed with a dropper, and the nanoparticles were centrifuged at 7830rpm for 25min followed by washed with ethanol three times. The CTAC template was removed by stirring the LPMSN in 100mL of 2% (w/w) NH_4NO_3 solution at 60˚C for 6 hours twice. Finally, the LPMSN fabricated were stored in ethanol under 4˚C for further use.

Fabrication of LPMSN-NH_2

50mg of LPMSN was transferred from stock solution to 15mL of dry toluene in a 100mL round-bottom flask. Afterwards, 70μL of (3-aminopropyl)triethoxysilane (APTES) was added into the mixture, and the reaction was carried out at 110˚C for 8 hours under continuous stir and nitrogen flow. Finally, the particle obtained was separated by centrifugation at 7830rpm for 20min and washed with 20mL of ethanol three times.

Fabrication of LPMSN-COOH

We modified the LPMSN with carboxylate groups by modifying LPMSN with nitrile groups followed by nitrile hydrolysis in water. First, 100mg of LPMSN was transferred from stock solution to 20mL of dry toluene in a 100mL round-bottom flask. Afterwards, 4.0mL of 3-(triethoxysilyl)propionitrile was added into the mixture, and the reaction was carried out at room temperature for 24 hours under continuous stir and nitrogen flow. The particle obtained was separated by centrifugation at 7830rpm for 20min and washed with 20mL of toluene twice and 20mL of ethanol once. The particles were then transferred to pure water for nitrile hydrolysis. To carry out the hydrolysis, the particles were re-dispersed in 60mL of 9N HCl aqueous solution and stirred at 105˚C for two hours, and the obtained LPMSN-COOH was washed with 30mL of water three times.

Fabrication of LPMSN-phosphonate

In a 100mL round-bottom flask, 0.18g of triethanolamine (TEA) was added to a mixture of 36mL water and 24mL CTAC solution. The solution was stirred at 60˚C for two hours to allow micelle self-assembly. Then, a mixture of 1mL TEOS and 19mL cyclohexane was added to the flask drop wisely to form a milky-white emulsion. The reaction was carried out in ambient air at 60˚C with reflux for another 24 hours. After the reaction, the cyclohexane layer was carefully removed with a dropper, and the nanoparticles were centrifuged at 7830rpm for 25min followed by washed with ethanol three times. To further modify the LPMSN surface with phosphonate groups, the LPMSN synthesized was then transferred to 100mL of pure water, and 0.30mL of 3-(Trihydroxysilyl)propyl methylphosphonate was added. The reaction was carried out at 78˚C for two hours. Finally, the CTAC template was removed by stirring the LPMSN-phosphonate in 100mL of 2% (w/w) NH_4NO_3 solution at 60˚C for 6 hours twice.

Fabrication of PDA-Fe nanoparticles

In a 500mL conical flask, 600mg of dopamine hydrochloride was dissolved in 160mL of pure water. Then, 120mg of ferric chloride hexahydrate was dissolved in 40mL of pure water, and the solution was added to the conical flask. The mixture was then stirred at 1100rpm for 10 minutes to form dark-green dopamine-iron complex. Afterwards, 40mL of 2.25M NH_3 aqueous solution was added into the flask, and the reaction was carried out under room temperature and 1100rpm magnetic stir for 24 hours. Finally, the synthesized PDA-Fe nanoparticles were separated by centrifugating at 7830rpm for 30min and washed by water for three times.

Fabrication of PDA-Fe-Eu

Europium-labeled PDA-Fe (PDA-Fe-Eu) was prepared by immersing PDA-Fe nanoparticles in aqueous europium(III) chloride hexahydrate solution. Specifically, 10mg of PDA-

Fe was dispersed in 5mL of pure water and then mixed with 5mL of 10mg/mL Europium(III) chloride hexahydrate aqueous solution. The mixture was stirred at room temperature for 8 hours, and the resulting PDA-Fe-Eu was washed with water for three times.

Fundamental Characterization of Nanoparticles

Dynamic Light Scattering (DLS) and Zeta Potential Analysis

DLS and Zeta-potential analysis were measured by a laser particle analyzer LPA-3100 at room temperature to characterize the hydrodynamic sizes and surface charge properties of nanoparticles. The LPMSN suspensions were diluted to 0.05mg/mL with pure water, and PDA-Fe suspensions were diluted to 0.01mg/mL with pure water in 1cm diameter cuvettes prior to measurements.

Inductively-Coupled Plasma Atomic Emission Spectroscopy (ICP-OES)

ICP-OES measurements were conducted on ICPE-9000 Shimadzu to quantify the Iron and Europium contents within PDA-Fe nanoparticles. The sample solutions were prepared by completely digesting the particles in Aqua Regia for two hours at 95˚C, followed by evaporation of liquid phase overnight. Afterwards, the residue was redissolved in 2.5% (v/v) nitric acid and kept at 95˚C for two hours. The cooled-down sample solutions were then taken to ICP-OES for further examination.

Transmission Electron Microscopy (TEM)

TEM images were recorded on Tecnai T12 cryo-electron microscope at 120kV accelerating voltage. The nanoparticle suspensions were dropped on 200-mesh carbon coated copper grid and dried under room temperature.

Scanning Electron Microscopy (SEM)

SEM images were recorded on Nova Nano 230 electron microscope. The PDA-Fe nanoparticle suspension was dropped on carbon tape, dried under room temperature, and attached to a pin stub specimen holder. 5~10nm of gold was sputtered on the nanoparticles for electron conductivity.

Characterization of pore properties

The surface area, total pore volume, and pore size distribution of nanoparticles were characterized by nitrogen adsorption method and analyzed by Brunauer-Emmett-Teller (BET) and Barrett-Joyner-Halenda (BJH) models.

Preparation of Drug-Loaded Carriers and Drug Loading Capacity Measurements

To load DLM in LPMSN, LPMSN particles were dispersed in EtOH:DMSO=10:1 (v/v) solvent at 1mg/mL concentration. Then, DLM was added into the dispersion at 5mg/mL concentration, followed by 24 hours of rocking. Afterwards, the particles were centrifuged down and washed with water three times. To load BDQ, PDA-Fe particles were dispersed in EtOH:DMSO=10:1 (v/v) solvent at 1mg/mL concentration. Then, BDQ was added into the PDA-Fe dispersion at 5mg/mL concentration, followed by 24 hours of rocking. Afterwards, the particles were centrifuged down and washed with water three times.

UV-Vis absorbance profiles were obtained on Agilent Cary 60 and analyzed by Cary WinUV Software to estimate the drug loading capacities of each carriers. Spectra was taken in a 1mL quartz cuvette under room temperature. To measure the amount of drug loaded, we re-dispersed the drug-loaded particles in DMSO, which is a good solvent for both DLM and BDQ, to

extract the drugs from the particle. After 24 hours of rocking, the concentrations of free drugs in the extract solution were characterized by UV-Vis spectroscopy. Because BDQ has negligible absorption above 350nm, to minimize the absorption peak overlap between BDQ and DLM in our multi-carrier, multi-drug delivery system, absorptions at 300nm and 360nm were selected for BDQ and DLM quantification, respectively (**Figure 20**).

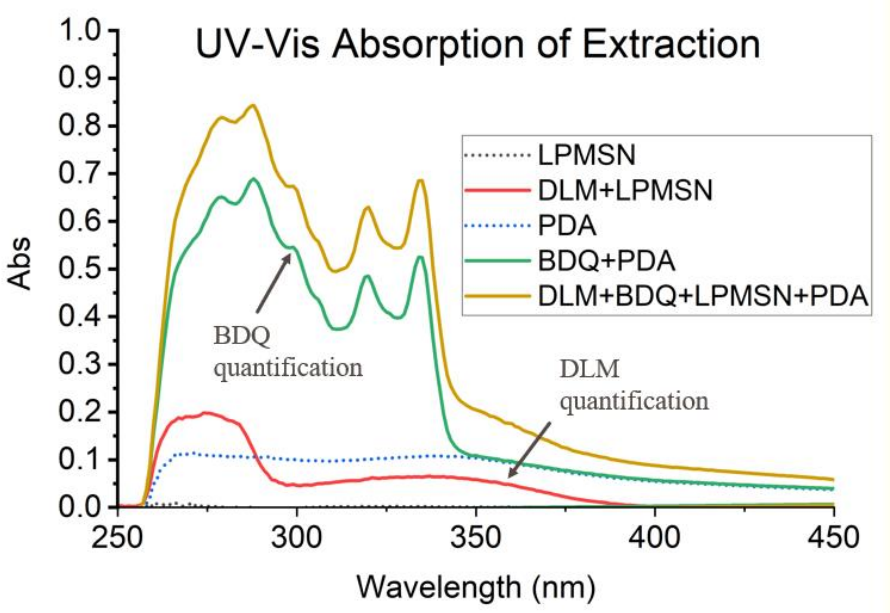

Figure 20. UV-Vis absorption spectra of extractions containing PDA-Fe, LPMSN, BDQ+PDA-Fe, DLM+LPMSN, and BDQ+DLM+PDA-Fe+LPMSN. 300nm and 360nm were selected for BDQ and DLM quantification, respectively.

6. Supplemental Information

Assessment of Eu(III) Doped PDA-Fe on Cytotoxicity and Efficacy

Our preliminary in vitro studies have indicated that PDA-Fe nanoparticles (PDA-Fe NPs) are well dispersed, without cytotoxicity, and are efficacious in antimicrobial treatment, thus making it an attractive platform for inhalational drug delivery. In anticipation of a need to quantify the amount of drug-loaded PDA-Fe NPs delivered to the lung in animal studies, PDA-Fe NPs with and without Eu(III) doping were prepared. We then assessed the safety and tolerability of these NPs in macrophages. We evaluated NPs loaded with BDQ in macrophages by measuring lactate dehydrogenase (LDH) release and the integrity of the macrophage monolayer, as reflected by nuclear counts (**Figure S1**). We observed that the level of LDH release and the nuclear counts in the macrophage monolayers treated with NPs with Eu doping vs. NPs without Eu doping for all three drugs were comparable to each other and to the untreated control. Although not a measure of the cytotoxicity of NPs, in addition to treating macrophages with NPs, we also treated the macrophages with extract from the BDQ-loaded PDA-Fe and PDA-Fe-Eu. These results confirmed that PDA-Fe NPs are not toxic to macrophages as assessed by the low LDH release and high nucleus counts of the macrophage monolayer, and Eu doping has no impact on cytotoxicity.

To assess whether Eu(III) doping affects drug efficacy against intracellular M. tuberculosis, we infected THP-1 macrophages with M. tuberculosis expressing IPTG-inducible green fluorescent protein and then either did not treat or treated with free drug, drug loaded PDA-Fe with and without Eu doping, or their DMSO extracts. After a 4-day incubation period, we fixed the macrophages with paraformaldehyde, stained the nuclei with DAPI and imaged by fluorescence microscopy. The acquired images were analyzed using Cell Profiler to quantitate integrated green fluorescence per nucleus per 10X microscopic field. Results from this study showed that Eu doping does not affect the inhibitory effect of BDQ-loaded PDA-Fe NPs on M. tuberculosis in macrophages (**Figure S2**).

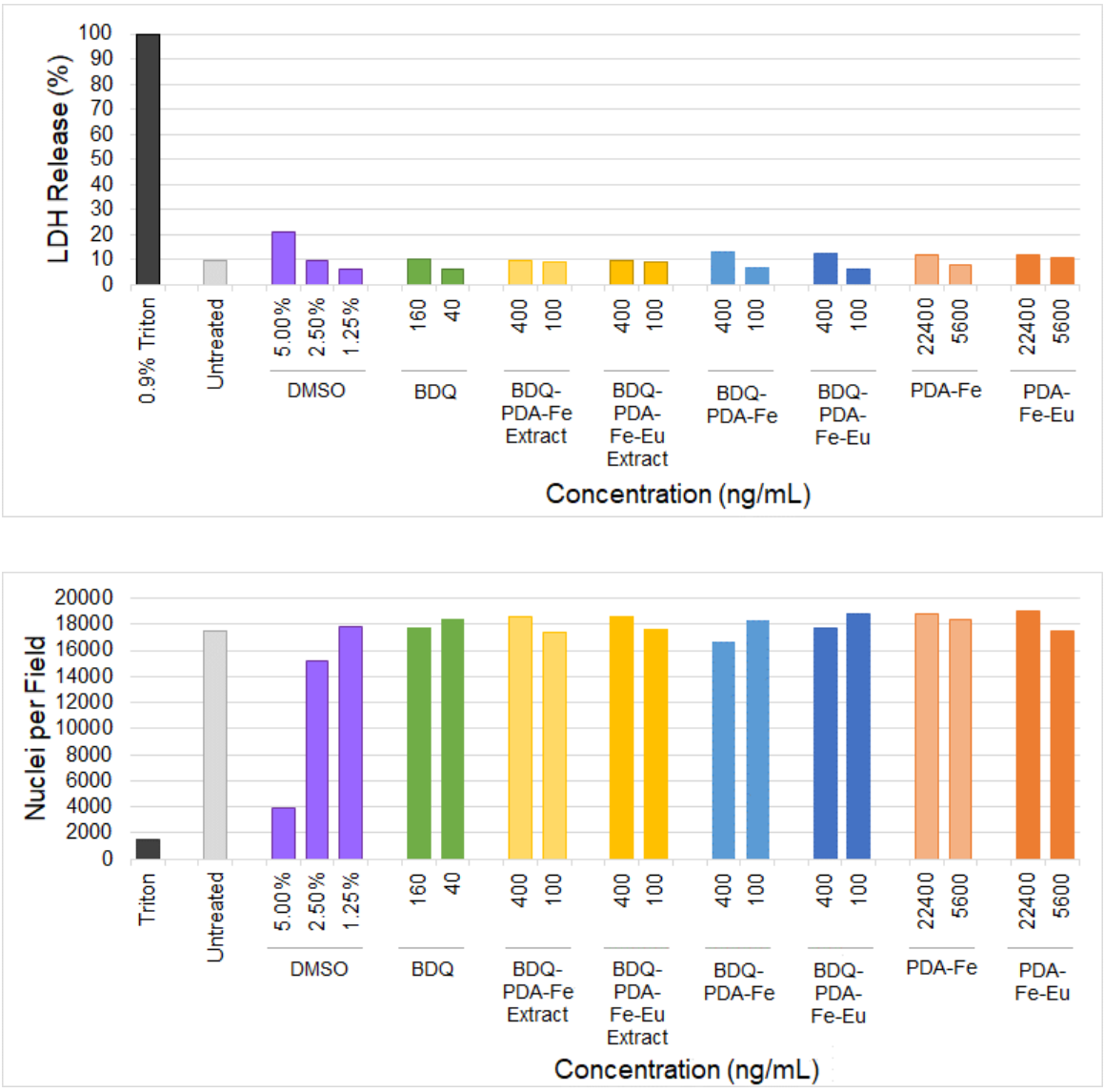

Figure S1. Cytotoxicity of BDQ-loaded PDA-Fe NPs with and without Eu doping as assessed by LDH release (A) and nuclear counts (B). Counts of macrophage nuclei per 10X microscopic field. DMSO was used to prepare drug extracts.

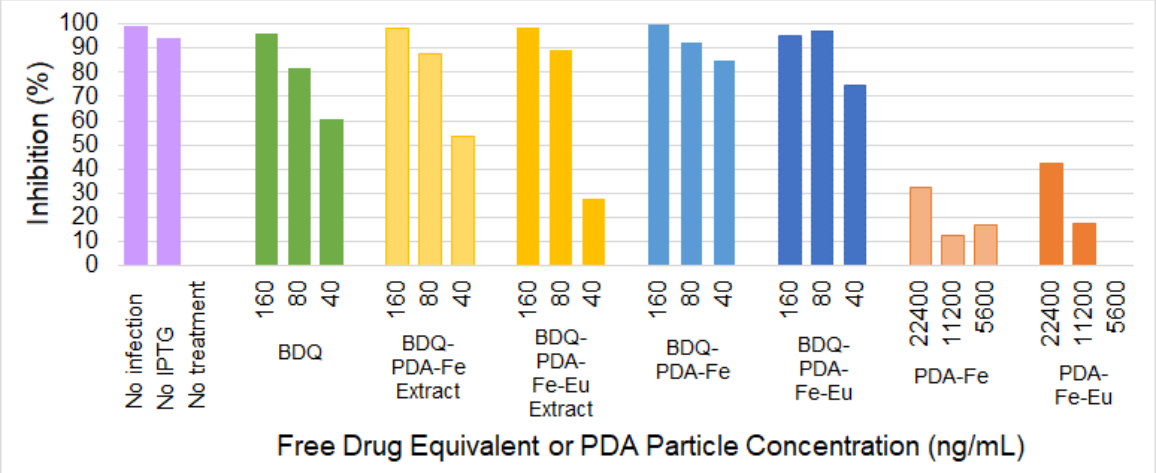

Figure S2. Treatment efficacy of BDQ loaded PDA-Fe NPs with and without Eu doping as assessed by quantifying integrated green fluorescence per nucleus.

7. References

1. B.Y. Lee, D.L. Clemens, A. Silva, B.J. Dillon, S. Maslesa-Galic, S. Nava, X.T. Ding, C.M. Ho, M.A. Horwitz, Drug regimens identified and optimized by output-driven platform markedly reduce tuberculosis treatment time, Nature Communications, **8**, 14183, (2017)
2. M.A. Horwitz, D.L. Clemens, B.Y. Lee, AI-Enabled Parabolic Response Surface Approach Identifies Ultra Short-Course Near-Universal TB Drug Regimens, Advanced Therapeutics, **3**(4), 1900086, (2020)
3. W. Chen, C.-A. Cheng, B.-Y. Lee, D.L. Clemens, W.-Y. Huang, M.A. Horwitz, J.I. Zink, Facile Strategy Enabling Both High Loading and High Release Amounts of the Water-Insoluble Drug Clofazimine Using Mesoporous Silica Nanoparticles, ACS Applied Materials & Interfaces, **10**(38), 31870-31881 (2018)
4. J. Wei, Z. Sun, W. Luo, Y. Li, A.A. Elzatahry, A.M. Al-Enizi, Y. Deng, D. Zhao, New Insight into the Synthesis of Large-Pore Ordered Mesoporous Materials, J. Am. Chem. Soc., **139**, 1706 (2017)
5. B. Rühle, P. Saint-Cricq, J.I. Zink, Externally Controlled Nanomachines on Mesoporous Silica Nanoparticles for Biomedical Applications, ChemPhysChem, **17**, 1769 (2016)
6. D. Tarn, C.E. Ashley, M. Xue, E.C. Carnes, J.I. Zink, C.J. Brinker, Mesoporous Silica Nanoparticle Nanocarriers: Biofunctionality and Biocompatibility, Acc. Chem. Res., **46**, 792 (2013)
7. C.C. Chou, W. Chen, Y. Hung, C.Y. Mou, Molecular Elucidation of Biological Response to Mesoporous Silica Nanoparticles in Vitro and in Vivo, ACS Appl. Mater. Interfaces, **9**, 22235 (2017)

8. B. Ruehle, D.L. Clemens, B.Y. Lee, M.A. Horwitz, J.I. Zink, A Pathogen-Specific Cargo Delivery Platform Based on Mesoporous Silica Nanoparticles, J. Am. Chem. Soc., **139**, 6663 (2017)

9. Z. Li, D.L. Clemens, B.Y. Lee, B.J. Dillon, M.A. Horwitz, J.I. Zink, Mesoporous Silica Nanoparticles with pH-Sensitive Nanovalves for Delivery of Moxifloxacin Provide Improved Treatment of Lethal Pneumonic Tularemia, ACS Nano, **9**, 10778 (2015)

10. R.R. Castillo, D. Lozano, M. Vallet-Regi, Mesoporous Silica Nanoparticles as Carriers for Therapeutic Biomolecules, Pharmaceutics, **12**(5), 432, (2020)

11. Y.X. Zhou, G.L. Quan, Q.L. Wu, X.X. Zhang, B.Y. Niu, B.Y. Wu, Y. Huang, X. Pan, C.B. Wu, Mesoporous silica nanoparticles for drug and gene delivery, Acta Pharmaceutica Sinica B, **8**(2), 165-177 (2018)

12. C. Xu, C. Lei, C.Z. Yu, Mesoporous Silica Nanoparticles for Protein Protection and Delivery, Frontiers in Chemistry, **7**, 290, (2019)

13. J. Ambati, A.M. Lopez, D. Cochran, P. Wattamwar, K. Bean, T.D. Dziubla, S.E. Rankin, Engineered silica nanocarriers as a high-payload delivery vehicle for antioxidant enzymes, Acta Biomaterialia, **8**(6), 2096-2103 (2012)

14. T.M. Guardado-Alvarez, W. Chen, A.E. Norton, M.M. Russell, W.B. Connick, J.I. Zink, Analyte-Responsive Gated Hollow Mesoporous Silica Nanoparticles Exhibiting Inverse Functionality and an AND Logic Response, Nanoscale, **8**, 18296 (2016)

15. D. Kwon, B.G. Cha, Y. Cho, J. Min, E.B. Park, S.J. Kang, J. Kim, Extra-Large Pore Mesoporous Silica Nanoparticles for Directing in Vivo M2 Macrophage Polarization by Delivering IL-4, Nano Lett., **17**, 2747 (2017)

16. C.A. Cheng, W. Chen, L. Zhang, H.H. Wu, J.I. Zink, A Responsive Mesoporous Silica Nanoparticle Platform for Magnetic Resonance Imaging-Guided High-Intensity Focused Ultrasound-Stimulated Cargo Delivery with Controllable Location, Time, and Dose, Journal of the American Chemical Society, **141**(44), 17670-17684 (2019)

17. K.M.L. Taylor, J.S. Kim, W.J. Rieter, H. An, W.L. Lin, W.B. Lin, Mesoporous silica nanospheres as highly efficient MRI contrast agents, Journal of the American Chemical Society, **130**(7), 2154-+ (2008)

18. D.K. Shen, J.P. Yang, X.M. Li, L. Zhou, R.Y. Zhang, W. Li, L. Chen, R. Wang, F. Zhang, D.Y. Zhao, Biphase Stratification Approach to Three-Dimensional Dendritic Biodegradable Mesoporous Silica Nanospheres, Nano Letters, **14**(2), 923-932 (2014)

19. F. Chen, Y.X. Xing, Z.Q. Wang, X.Y. Zheng, J.X. Zhang, K.Y. Cai, Nanoscale Polydopamine (PDA) Meets pi-pi Interactions: An Interface-Directed Coassembly Approach for Mesoporous Nanoparticles, Langmuir, **32**(46), 12119-12128 (2016)

20. M. Brownell, A.K. Nair, Adhesion and Interface Properties of Polydopamine and Polytetrafluoroethylene Thin Films, Journal of Applied Mechanics-Transactions of the Asme, **87**(12), 121002, (2020)

21. Q.H. Yu, C.M. Zhang, Z.W. Jiang, S.Y. Qin, A.Q. Zhang, Mussel-Inspired Adhesive Polydopamine-Functionalized Hyaluronic Acid Hydrogel with Potential Bacterial Inhibition, Global Challenges, **4**(2), 1900068, (2020)

22. L. Han, X. Lu, K.Z. Liu, K.F. Wang, L.M. Fang, L.T. Weng, H.P. Zhang, Y.H. Tang, F.Z. Ren, C.C. Zhao, G.X. Sun, R. Liang, Z.J. Li, Mussel-Inspired Adhesive and Tough Hydrogel Based on Nanoclay Confined Dopamine Polymerization, Acs Nano, **11**(3), 2561-2574 (2017)

23. M.A. Selo, J.A. Sake, K.J. Kim, C. Ehrhardt, In vitro and ex vivo models in inhalation biopharmaceutical research - advances, challenges and future perspectives, Advanced Drug Delivery Reviews, **177**, 113862, (2021)

24. D.Q. Arick, Y.H. Choi, H.C. Kim, Y.Y. Won, Effects of nanoparticles on the mechanical functioning of the lung, Advances in Colloid and Interface Science, **225**, 218-228 (2015)

25. R. Wustneck, J. Perez-Gil, N. Wustneck, A. Cruz, V.B. Fainerman, U. Pison, Interfacial properties of pulmonary surfactant layers, Advances in Colloid and Interface Science, **117**(1-3), 33-58 (2005)

26. A. Hidalgo, A. Cruz, J. Perez-Gil, Pulmonary surfactant and nanocarriers: Toxicity versus combined nanomedical applications, Biochimica Et Biophysica Acta-Biomembranes, **1859**(9), 1740-1748 (2017)

27. M. Radiom, M. Sarkis, O. Brookes, E.K. Oikonomou, A. Baeza-Squiban, J.F. Berret, Pulmonary surfactant inhibition of nanoparticle uptake by alveolar epithelial cells, Scientific Reports, **10**(1), 19436, (2020)

28. F. Mousseau, C. Puisney, S. Mornet, R. Le Borgne, A. Vacher, M. Airiau, A. Baeza-Squiban, J.F. Berret, Supported pulmonary surfactant bilayers on silica nanoparticles: formulation, stability and impact on lung epithelial cells, Nanoscale, **9**(39), 14967-14978 (2017)